TECHNISCHE UNIVERSITÄT
BERGAKADEMIE FREIBERG
The University of Resources. Since 1765.

Strain, charge carriers, and phonon polaritons in wurtzite GaN
-
a Raman spectroscopical view

By the Faculty of Chemistry and Physics
of the Technische Universität Bergakademie Freiberg

approved

Thesis

to attain the academic degree of

doctor rerum naturalium
(Dr. rer. nat.)

submitted by **Dipl. Nat. Christian Röder**

born on the 2nd July 1982 in Schlema

Assessor: Prof. Dr. Jens Kortus
Prof. Dr. Ion M. Tiginyanu

Date of the award:Freiberg, 30th September 2014

Kurzdarstellung

Die vorliegende Dissertation „Strain, charge carriers, and phonon polaritons in wurtzite GaN - a Raman spectroscopical view“ befasst sich der ramanspektroskopischen Charakterisierung von Galliumnitrid (GaN). Der Zusammenhang zwischen Waferkrümmung und mechanischer Restspannungen wird diskutiert. Mit Hilfe konfokaler Mikro-Ramanmessungen wurden Dotierprofile nachgewiesen sowie die Ladungsträgerkonzentration und -beweglichkeit ermittelt. Sämtliche Ramantensorelemente von wz-GaN wurden erstmals durch die Anwendung verschiedener Streugeometrien bestimmt. Eine neu entwickelte Vorwärtsstreuanordnung ermöglichte die Beobachtung von Phonon-Polaritonen. Es konnte gezeigt werden, dass von der theoretischen und experimentellen Betrachtung der Ramanstreuintensitäten dieser Elementaranregungen eindeutig das Vorzeichen der Faust-Henry-Koeffizienten von wz-GaN abgeleitet werden kann. Im Rahmen dieser Arbeit wurden alle Faust-Henry-Koeffizienten für GaN experimentell bestimmt.

Abstract

This thesis "Strain, charge carriers, and phonon polaritons in wurtzite GaN - a Raman spectroscopical view" focuses on special aspects of the Raman spectroscopical characterization of wurtzite gallium nitride (wz-GaN). The correlation between wafer curvature and residual stress is discussed. By means of confocal micro-Raman measurements doping profiles were detected as well as the density and mobility of free charge carriers were deduced. All Raman scattering cross sections of wz-GaN were determined the first time using different scattering configurations. A novel method for near-forward scattering was developed in order to observe phonon polaritons with pure symmetry. It is shown that the theoretical and experimental consideration of the Raman scattering efficiency of these elementary excitations allow for determining the sign of the Faust-Henry coefficients of wz-GaN unambiguously. The Faust-Henry coefficients of GaN were deduced from Raman scattering efficiencies of corresponding TO and LO phonons.

Thesen zur Dissertation

1. Die Nitride der dritten Hauptgruppe (AlN, GaN, InN) bilden ein herausragendes Materialsystem im Hinblick auf opto- und mikroelektronische Anwendungen im Hochfrequenz-, Hochleistungs- und Hochtemperatur-Bereich. Besonders der Einsatz dieser Materialien zur Realisierung von weißen Leuchtdioden scheint sehr vielversprechend zu sein.

2. Im Rahmen dieser Arbeit wurde die Ramanspektroskopie als vielseitige und empfindliche Methode zur Charakterisierung von hexagonalem GaN mit Wurtzitstruktur eingesetzt. Die Ergebnisse ergänzen Resultate, die zum Beispiel mittels Röntgenbeugung oder Photolumineszenzmessungen erzielt wurden. Die Anwendung der Mikro-Ramanspektroskopie ist weit verbreitet. Im speziellen haben die Messungen den Vorteil, dass sie sowohl zerstörungsfrei als auch berührungslos sind und eine exzellente laterale Auflösung bieten. Bei Materialien, die für die verwendete Anregungswellenlänge transparent sind, kann durch den Einsatz der konfokalen Technik eine hohe Tiefenauflösung erreicht werden.

3. Der Einfluss mechanischer Spannungen auf Ramanmoden wurde diskutiert und an einem ausgewählten Beispiel demonstriert. Mit Hilfe konfokaler Ramanmessungen wurde die Änderung von mechanischen Restspannungen in epitaktisch abgeschiedenen GaN-Schichten untersucht. Die Ergebnisse bestätigen die Krümmung der Schichtsysteme als einen wirkungsvollen Relaxationsmechanismus thermisch induzierter Verspannung. Die thermische Verspannung wird durch den Unterschied der thermischen Ausdehnungskoeffizienten von GaN und dem verwendeten Saphir-Substrat hervorgerufen. Die experimentell ermittelte Krümmung der untersuchten Proben wurde mit theoretischen Werten verglichen. Dazu wurden die Krümmungsradien mit Hilfe eines von Etzkorn und Clarke etablierten mechanischen Krümmungsmodells und eines FEM-Modells simuliert. Die Limitierung der Anwendbarkeit des Etzkorn/Clarke-Modells hinsichtlich der Probenkenngrößen (a) GaN-Schichtdicke und (b) Radius der Substratscheibe wurden aufgezeigt und diskutiert. FEM-Rechnungen rechtfertigen, auf das Etzkorn/Clarke-Modell zurückzugreifen, um die spektrale Position der $E_{2,high}$ Ramanmode in Abhängigkeit der GaN-Schichtdicke zu simulieren.

4. Ferner wurden gekoppelte LO-Phonon-Plasmon-Moden untersucht, um die Konzentration und Beweglichkeit freier Ladungsträger aus gemessenen Frequenzen, Halbwertsbreiten und Intensitäten zu ermitteln. Das Dotierprofil eines (0001) orientierten GaN Einkristalls wurde ermittelt und direkt mit dem Wachstumsprozess korreliert. Die Ergebnisse liefern eine wertvolle Rückkopplung an die Kristallzüchter. Insbesondere sind die konfokalen Ramanmessungen in Rückstreuan-

ordnung bedeutungsvoll, da sie (a) zerstörungsfrei ausgeführt werden und (b) E_1(LO) Phononen und damit gekoppelte LO-Phonon-Plasmonmoden in Rückstreugeometrie von Oberflächen senkrecht zur c-Richtung nicht zugänglich sind. Aus der Anpassung der Linienform der beobachteten L_+-Mode mit Hilfe eines dielektrischen Modells konnte die Ladungsträgerkonzentration und -beweglichkeit ermittelt werden. Die erhaltenen Ergebnisse stimmen gut mit denen von Hall-Messungen überein.

5. Die Anwendung des dielektrischen Modells zur Ermittlung der Ladungsträgerkonzentration und -beweglichkeit setzt die Kenntnis der Faust-Henry-Koeffizienten voraus. Während in kubischen Einkristallen ein Koeffizient ausreicht, gibt es für Einkristalle mit Wurtzitstruktur aufgrund der Symmetrie drei solche Koeffizienten. Bisher ist in der Literatur nur der Faust-Henry-Koeffizient C_a^{FH} mit voneinander abweichenden Werten und Vorzeichen bekannt. In Abhängigkeit vom Vorzeichen des Koeffizienten überlagern sich Beiträge der Gitterverformung und des begleitenden makroskopischen elektrischen Feldes zur Ramanstreuintensität konstruktiv oder destruktiv.

6. Die Faust-Henry-Koeffizienten können aus dem Verhältnis der Ramanstreuintensitäten der entsprechenden LO- und TO-Phononen ermittelt werden. Zur Bestimmung aller Streuintensitäten wurden systematische Ramanmessungen an undotierten GaN-Einkristallen mit unterschiedlichen Streuanordnungen ausgeführt. Erstmals werden die relativen Ramanstreuquerschnitte aller Ramanmoden von GaN zusammenhängend ermittelt.

7. In der vorliegenden Arbeit wird auf die Bestimmung der Faust-Henry-Koeffizienten in besonderer Weise eingegangen. Dies schließt die Untersuchung der Temperaturabhängigkeit mit ein. Ausgehend von den experimentell ermittelten Ramanstreuquerschnitten wurden die Faust-Henry-Koeffizienten berechnet. Allerdings gibt es für jeden der drei Koeffizienten zwei mögliche Lösungen. Die Betrachtung der Ramanstreuintensitäten von Phonon-Polaritonen ermöglicht, das Vorzeichen der Faust-Henry-Koeffizienten eindeutig zu bestimmen. Phonon-Polaritonen sind in einer Vorwärtsstreuanordnung zugänglich.

   a) Die theoretischen Ausdrücke für die Ramanstreuintensitäten für Phonon-Polaritonen in uniaxialen Kristallen wurden hergeleitet. Im Grenzfall für große Beträge übertragener Wellenvektoren beschreiben diese Gleichungen das Verhalten der polaren Phononmoden.

   b) Ein neuartige Experimentieranordnung für die Vorwärtsstreuung wurde entwickelt. Dazu wurde vor die Eingangsoptik des Spektrometers ein Schirm mit einem rechteckig zu öffnenden Fenster gesetzt. Dies ermöglicht die De-

tektion von Phonon-Polaritonen mit reiner E_1 oder A_1 Symmetrie in Abhängigkeit des übertragenen Wellenvektors. Die experimentellen Resultate zeigen eine exzellente Übereinstimmung mit den theoretisch berechneten Dispersionkurven als Funktion des übertragenen Wellenvektors für ordentliche und außerordentliche Polaritonen.

c) Die experimentell ermittelten Ramanstreuintensitäten der Phonon-Polaritonen wurden mit berechneten Intensitäten verglichen. Zur Berechnung wurden die vorher abgeleiteten theoretischen Ausdrücke herangezogen. Der Vergleich schließt die Lösung der Faust-Henry-Koeffizienten mit positivem Vorzeichen aus. Für wz-GaN ergeben sich die drei Koeffizienten daher zu C_a^{FH} = -3.46, C_b^{FH} = -3.81 und C_c^{FH} = -2.31.

8. Die ermittelten Ramanstreuquerschnitte und die bestimmten Faust-Henry-Koeffizienten wurden genutzt, um alle Ramantensorelemente für GaN relativ zum dem Tensorelement des nicht-polaren $E_{2,\mathrm{high}}$ Phonons zu berechnen. Dabei fand die Abhängigkeit der Streuquerschnitte von den Phononfrequenzen Berücksichtigung.

Contents

1 Introduction

Gallium nitride (GaN) and its ternary alloys with aluminum (Al) and indium (In) are remarkable and important material systems for several electronic and short-wavelength optoelectronic applications. GaN-based microelectronic devices, for instance, take advantage of the superior electronic properties for high-power, high-frequency, and high-temperature applications. Furthermore, the group III nitride semiconductors with direct band gaps ranging from 0.7 eV (InN) through 3.4 eV (GaN) to 6.0 eV (AlN) have inspired the field of solid-state lighting. In particular, applications of these materials realizing bright, white light-emitting diodes (LEDs) appear very promising [1–5]. However, due to the high melting temperature of GaN standard crystallization techniques are not applicable. Typically, GaN is grown heteroepitaxially on foreign substrates such as sapphire or silicon carbide, for instance. Sapphire is the most frequently used material for the growth of GaN. Due to the lattice mismatch and the difference in the thermal expansion coefficients between GaN and these substrates, there are serious problems, such as large density of structural imperfections, e.g. dislocations or grain boundaries, as well as the formation of strain.

The present work was performed within the framework of the joint project *Atomic Design and Defect Engineering*. The aim of this project focuses on the intentional alteration and design of material properties by modifications of the crystal structure on the atomic scale. One of the subprojects addresses novel approaches for the epitaxial growth of wz-GaN and subsequently the extensive characterization of the grown GaN layers.

Recently, there has been increasing interest to clarify the correlation between growth conditions and inherent properties of GaN using x-ray diffraction (XRD) [6–8], wafer curvature [9–13], high resolution transmission electron microscopy [14, 15], and photoluminescence [10, 13, 16].

In this field, Raman spectroscopy has also evolved as a powerful and versatile technique (see chapter 3). This method provides information on the vibrational states of GaN which are sensitive to the crystalline quality and free charge carriers as well as to external impacts such as temperature, pressure or strain (see chapter 4). Therefore, the results obtained by Raman measurements can supply beneficial feedback information on the growth process. Micro-Raman measurements are meaningful since they take advantage of being non-destructive, contactless, and providing an excellent resolution - both laterally and in the depth. Numerous Raman scattering studies have

been performed characterizing the residual stress [7–9, 17–19] or the density and mobility of free charge carriers [20–23] in GaN, for instance. For reviews see articles published by Kuball [24] or Harima [25].
In order to access the charge carrier concentration as well as their mobility by Raman scattering from measured frequencies, bandwidths, and intensities of coupled phonon plasmon modes [26–28] (see chapter 5), the knowledge of the Faust-Henry coefficients is required. These coefficients are ratios describing the relative influence of lattice displacements and electric field onto the dielectric susceptibility [26, 29, 30]. In the case of wz-GaN merely the Faust-Henry coefficient connected with the polar phonon mode of A_1 symmetry and its assigned Raman tensor elements a_{TO} and a_{LO} has been reported with differing values and questionable sign [31–35]. However, according to its wurtzite structure, in hexagonal GaN three Faust-Henry coefficients associated with phonon modes of different symmetry exist.
The present study reports on an accurate determination of the Faust-Henry coefficients in wz-GaN. These coefficients can be obtained by measuring the Raman scattering efficiencies of the corresponding LO and TO phonons. The Raman measurements require the application of different scattering geometries, i.e. backscattering as well as right-angle and near-forward scattering configurations. However, reports on measurements of relative or absolute Raman cross sections of phonons in wz-GaN are scarce in the literature [36]. Besides a detailed derivation of the theoretical Raman scattering efficiency in wurtzite crystals (see chapter 3), results of systematic Raman measurements on bulk wz-GaN single crystals in order to access the Raman scattering efficiencies will be presented (see chapter 6). From the obtained Raman scattering intensities of wz-GaN, the respective Faust-Henry coefficients as well as the absolute value of each Raman tensor element will be deduced.
Furthermore, it is shown that the Raman scattering efficiency of TO phonon polaritons allows to overcome the dilemma of the sign of Faust-Henry coefficients. Elementary excitations called phonon polaritons are derived when infrared photons strongly interact with the transverse modes of infrared active phonons. The frequencies of phonon polaritons occur in the terahertz (THz) spectral range. This range corresponds to the gap between high-frequency electronics and low-frequency optics. Phonon polariton studies have recently gained interest stimulated by the generation of THz pulses by femtosecond lasers and ultrasound acoustic waves [37], THz spectroscopy and imaging [38, 39].
Reports on Raman studies of phonon polaritons in uniaxial semiconductors are scare [40]. In this work, Raman spectra of systematic measurements of ordinary and extraordinary phonon polaritons in wz-GaN are presented (see chapter 7). A novel experimental near-forward scattering setup will be introduced with a screen positioned in a plane before the first image lens which enables to open a small adjustable rectangular window in this plane. Thus, measurements of phonon polaritons with well

defined wavevector transfer can be realized. The Raman scattering efficiency of the phonon polaritons in dependence on the frequency has been studied. A detailed theoretical treatment of the Raman scattering efficiency for arbitrary directions of phonon polaritons in uniaxial crystals with wurtzite structure is given. The comparison of polariton scattering efficiency results with theoretical ones enables to assign one solution of each Faust-Henry coefficient unambiguously.

2 Properties of gallium nitride

There are three crystal structures shared by the binary group III nitride species, aluminum nitride (AlN), gallium nitride (GaN), and indium nitride (InN): (i) the wurtzite, (ii) zinc blende, and (iii) rocksalt structures. The wurtzite structure (α polytype) is the thermodynamically stable one for bulk material of these compounds at ambient conditions. At high pressures a phase transition to the rocksalt structure occurs. In contrast, the zinc blende structure (β polytype) is metastable and may be stabilized only by heteroepitaxial growth on substrates with a cubic crystal structure, such as silicon (Si), magnesium oxide (MgO) or gallium arsenide (GaAs).

As all GaN samples investigated in this work exhibit wurtzite structure, the following discussion will be confined to wurtzite-type GaN (wz-GaN) only. Owing to the uniaxial crystal structure the properties are anisotropic as shown in table 2.1 for selected properties.

Tab. 2.1: Selected properties of wurtzite-type GaN at 300 K.

	GaN	Reference
Lattice parameter[a]	a = 0.318926 nm	[41]
	c = 0.518523 nm	
Thermal expansion coefficients[a]	α_a = (6.2$\pm$0.4) $\times$ 10^{-6} K^{-1}	[42]
	α_c = (5.7$\pm$0.5) $\times$ 10^{-6} K^{-1}	
Elastic constants	C_{11} = 367 GPa	[43]
	C_{12} = 135 GPa	
	C_{13} = 103 GPa	
	C_{33} = 405 GPa	
	C_{44} = 95 GPa	
Band gap (E_g)	3.39 eV	[25]
Refractive index	2.44 (at 514.5 nm)	[44]

[a] For comparison, sapphire (Al_2O_3) has lattice parameters of a = 0.47577 nm and c = 1.29907 nm [45] and thermal expansion coefficients α_a = (7.9$\pm$0.7) $\times$ 10^{-6} K^{-1} and α_c = (9.5$\pm$0.6) $\times$ 10^{-6} K^{-1} [12].

2.1 Crystal structure

The primitive unit cell of wz-GaN contains four atoms and belongs to the space group $C_{6\nu}^4$ ($P6_3mc$). In figure 2.1(a) the wurtzite crystal structure as well as its corresponding lattice parameters a in lateral direction and c in vertical direction with a ratio $c/a = \sqrt{8/3}$ are depicted. Each Ga atom is tetrahedrally coordinated by four N atoms, and vice versa. The stacking order of (0001)[1] planes is ABAB... along $\langle 0001 \rangle$ direction (c axis) for the hexagonal structure. Here A and B denote the allowed sites of the GaN pair in the hexagonal close packed layer of spheres. Thus, for the wurtzite structure the basal or (0001) crystal plane is the primary polar plane being either Ga- or N-terminated. In consequence, a (0001) surface (Ga polar) is not equivalent to a $(000\bar{1})$ surface (N polar) resulting in different chemical as well as physical properties of the surfaces.

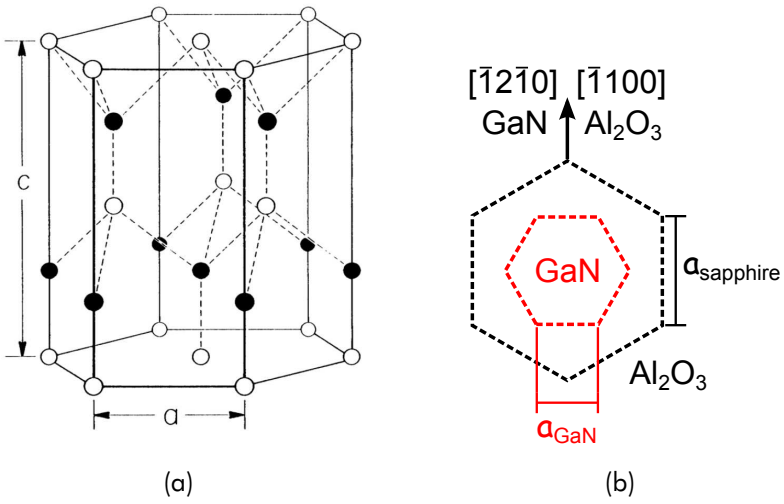

Fig. 2.1: (a) The wurtzite crystal structure (from [46]) with lattice parameter c in vertical direction and a in lateral direction. The Ga and N atoms in the wurtzite lattice are indicated by open and full circles, respectively. (b) Schematic illustration (top view) of the epitaxial relationship between c plane GaN grown on (0001) oriented sapphire (Al_2O_3) representing the 30° rotation of the GaN basal plane.

2.2 Epitaxial growth

Due to the high melting temperature of wurtzite-type GaN standard crystallization techniques are inapplicable. Therefore, one of the biggest challenges of GaN preparation is the lack of cost-efficient and high-quality substrates for homoepitaxy. Nowadays, GaN technology is based on heteroepitaxy [47–50]. The most widely used substrates are sapphire (0001), 6H-SiC (0001), and Si (111). Owing to the lattice mismatch and the difference in the thermal expansion coefficients between GaN and

[1] Note here the use of the four index notation $\{hkil\}$. The indices hki fulfil the relation $i = -(h + k)$.

these substrates, there are serious problems, such as large density of structural imperfections, e.g. dislocations or grain boundaries, as well as the formation of strain that eventually leads to cracking of the layer [11, 51–53].

For the heteroepitaxial growth of c plane GaN on (0001) oriented sapphire (Al_2O_3) with the mutual in-plane orientation $\langle\bar{1}2\bar{1}0\rangle_{\text{GaN}} \parallel \langle\bar{1}100\rangle_{\text{sapphire}}$, the lattice mismatch f with regard to the substrate reference lattice is

$$f = \frac{a_{\text{sapphire}} - \sqrt{3} \cdot a_{\text{GaN}}}{a_{\text{sapphire}}}, \tag{2.1}$$

where a_{GaN} and a_{sapphire} denote the in-plane lattice parameters of GaN and sapphire (see table 2.1), respectively.

The above mentioned orientation relationship leads to a significant reduction of the lattice misfit by 30° rotation of both lattices against each other and is shown schematically in figure 2.1(b). However, from the difference in the interatomic distances between the metallic atoms (Ga and Al) the calculated epitaxial lattice misfit f at room temperature is about -16%. As the interatomic distances are larger in GaN than in sapphire, compressive residual stress in GaN is expected.

Nevertheless, in dependence on the growth technique the reported lattice parameters of GaN (figure 2.2) show unusual large fluctuations. Due to the lack of a native substrate in the growth process it is difficult to prepare strain-free material and subsequently to determine the intrinsic unstrained lattice parameters.

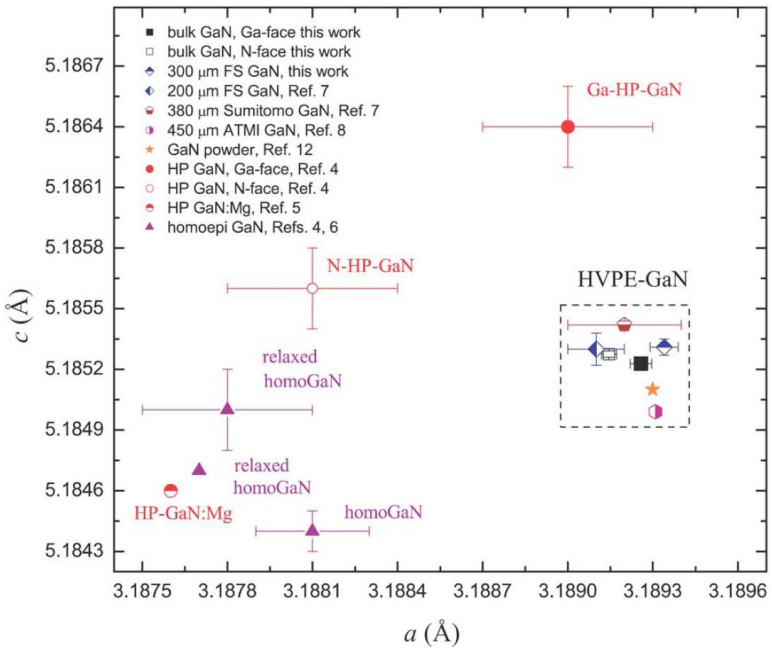

Fig. 2.2: Lattice parameters a and c for bulk and freestanding GaN fabricated by HVPE, HP bulk GaN, and homoepitaxial GaN layers (from [54] and references therein).

From a technological point of view, the Hydride Vapor Phase Epitaxy (HVPE) is ascribed a great potential for growing free-standing GaN substrates due to high

growth rates. Several routes to produce thick, high-quality HVPE layers starting from sapphire substrates are currently under investigation, such as (i) HVPE overgrowth of GaN templates manufactured by Metalorganic Vapor Phase Epitaxy (MOVPE) on sapphire [55], and (ii) the deposition of GaN layers directly on sapphire in a closed HVPE process [56]. Within the framework of the joint project *Atomic Design and Defect Engineering* a novel approach for the deposition of GaN directly on sapphire substrates was developed. The closed two-step HVPE process includes the growth of GaN nucleation layers at intermediate temperatures in the range of 750 - 900°C. In comparison to frequently used low-temperature (LT) nucleation layers, significant changes in the surface kinetics and consequently an improved crystallinity are expected due to nucelation temperatures at least 150 K above the LT nucleation range. Subsequently, a high-temperature overgrowth of the nucleation layers at about 1040°C was conducted resulting in 10 μm thick, crack-free GaN layers of high crystalline quality [49].

Moreover, the High Temperature Vapor Phase Epitaxy (HTVPE) as a promising chlorine-free technique for the growth of GaN films was modified within this joint project. The method employs ammonia (NH_3) and thermally evaporated metallic gallium (Ga) as precursors [50] which mainly contributes to the environmental impact of this growth technique. A novel growth reactor was developed in order to overcome the drawbacks of conventional HTVPE, such as non-stationary transport and growth conditions, strong thermal coupling between Ga source and substrate, and a high contamination level of the deposited films. According to the achieved growth rate of 50 μm/h the HTVPE technique is ascribed the potential for growth of thick GaN layers. For more details see the article recently published by Lukin *et al.*[50].

2.3 Mechanical and thermal properties

In the following section mechanical and thermal properties of wurtzite-type GaN are discussed as both contribute to a profound understanding of the stress-strain-correlation in terms of the growth of GaN. Generally, Hookes law describes the stress-strain relation in the limit of the linear elasticity theory:

$$\sigma_{ij} = C_{ijkl}\varepsilon_{kl} \qquad \text{with } i,j,k,l = 1\ldots 3, \tag{2.2}$$

where C_{ijkl} refers to the fourth-rank tensor of the elastic stiffness constants, σ_{ij} and ε_{kl} denote stress and strain tensor, respectively. As both of these tensors are symmetric[2], Hookes law can be written as

$$\sigma_i = C_{ij}\varepsilon_j \qquad \text{with } i,j = 1\ldots 6, \tag{2.3}$$

[2] i.e., $\sigma_{ij} = \sigma_{ji}$ and $\varepsilon_{kl} = \varepsilon_{lk}$. Thus, the relation $C_{ijkl} = C_{klij}$ is fulfilled.

introducing the so-called matrix notation[3]. Both, the stress and strain tensor components are denoted by a single index running from 1 to 6. Concerning the elastic stiffness tensor C_{ijkl} the first two indices i, j as well as the last two ones k, l are abbreviated into a single index each according to the scheme [57]:

tensor notation	11	22	33	23, 32	31, 13	12, 21
matrix notation	1	2	3	4	5	6

In case of wz-GaN, five elastic constants C_{ij} have to be considered and the stiffness tensor in matrix notation takes the following form:

$$C_{ij} = \begin{pmatrix} C_{11} & C_{12} & C_{13} & 0 & 0 & 0 \\ C_{12} & C_{11} & C_{13} & 0 & 0 & 0 \\ C_{13} & C_{13} & C_{33} & 0 & 0 & 0 \\ 0 & 0 & 0 & C_{44} & 0 & 0 \\ 0 & 0 & 0 & 0 & C_{44} & 0 \\ 0 & 0 & 0 & 0 & 0 & {}^1\!/_2(C_{11} - C_{12}) \end{pmatrix}, \tag{2.4}$$

where the X, Y, and Z axes of the laboratory coordinate system are chosen along the GaN $[11\bar{2}0]$, $[1\bar{1}00]$, and $[0001]$ directions, respectively. In this work elastic constants reported by Wright *et al.*[43] (see table 2.1) were adopted. It should be mentioned, that it is necessary to go back to the tensor notation in order to transform the elastic tensor to other axes. The fourth-rank tensor C_{ijkl} transforms to C'_{ijkl} on change of axes where a_{ij} refers to the corresponding transformation matrix:

$$C'_{ijkl} = a_{im} a_{jn} a_{ko} a_{lp} C_{mnop}. \tag{2.5}$$

As described in section 2.2 the growth of GaN by means of vapor phase epitaxy is performed at high temperatures of about 1000°C. Epitaxial layer systems consist of different materials, i.e. film and substrate, differing in their lattice parameters as well as their thermal expansion coefficients. Owing to the difference in the thermal expansion coefficients of film and substrate the layer system experiences a thermally induced strain on cooling down from growth temperature to room temperature. The thermal mismatch strain $\varepsilon_{\mathsf{th}}$ between film and substrate at room temperature is expressed as:

$$\varepsilon_{\mathsf{th}} = \int_{T_{\mathsf{G}}}^{T_{\mathsf{RT}}} \left(\alpha^{\mathsf{substrate}}(T) - \alpha^{\mathsf{film}}(T) \right) \mathrm{d}T, \tag{2.6}$$

where T_{G} refers to the growth temperature, T_{RT} is the room temperature, and $\alpha^{\mathsf{film}}(T)$ and $\alpha^{\mathsf{substrate}}(T)$ denote the respective temperature dependent thermal expansion coefficients of film and substrate. Due to the hexagonal structure of GaN the thermal expansion coefficients are anisotropic, i.e. different for a and c direction (see table 2.1).

[3]This notation was established by the physicist Woldemar Voigt in 1910.

2.4 Band structure of GaN

After the description of the mechanical and thermal properties of GaN the following discussion will focus on the electronic properties.

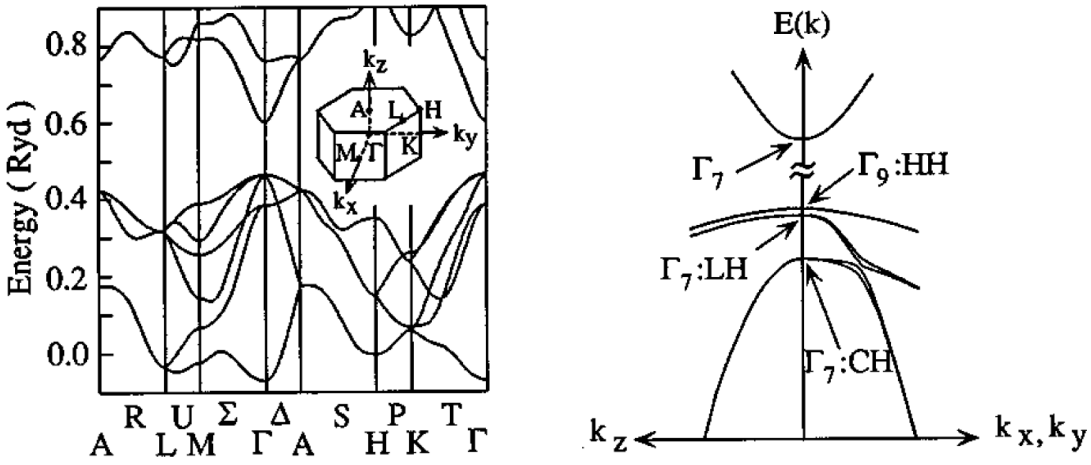

Fig. 2.3: Electronic band structure of wurtzite GaN without strain (from [58]). (a) Dispersion along the symmetry lines. The inset shows the first Brillouin zone. (b) Schematic band structure along the k_z direction and in the k_x-k_y plane near the Γ point. For details see text.

Figure 2.3 shows the electronic band structure of wurtzite GaN along the symmetry lines in the first Brillouin zone which is represented by the inset in figure 2.3(a). The wavevector in the first Brillouin zone is indicated by k. The calculations were performed by means of a full-potential linearized augmented plane wave (FLAPW) method [59], within the local density functional approximation (LDA) [60]. For more details concerning the calculations see Suzuki *et al.*[58]. The schematic band structure near the Γ point of wz-GaN without strain is depicted in figure (b). Neglecting spin-orbit interaction, the direct band gap of GaN is formed by an s-like Γ_{1c} conduction band state and p-like Γ_{6v} and Γ_{1v} valence band states due to crystal field splitting [61]. Taking the weak spin-orbit interaction into account, the Γ_{6v} state is split into two twofold degenerate states (Γ_9 and Γ_7). The Γ_1 state has also Γ_7 symmetry [58]. The upper three hole bands are labelled as HH (heavy), LH (light), and CH (crystal field split off). The corresponding effective masses of these three hole bands show an anisotropic behavior with respect to the k_z direction and the k_x-k_y plane as depicted in figure 2.3(b).

At room temperature the optical transition $\Gamma_{9v} \rightarrow \Gamma_{7c}$ referred to as the A exciton transition is observable with the energy gap influenced by strain [10, 62, 63]. The strain dependence of the A free exciton transition energy E_A is given by Shan *et al.*[63]:

$$E_A = E_A(0) + a_1\varepsilon_{zz} + a_2\left(\varepsilon_{xx} + \varepsilon_{yy}\right) + b_1\varepsilon_{zz} + b_2\left(\varepsilon_{xx} + \varepsilon_{yy}\right), \tag{2.7}$$

where $E_A(0)$ represents the strain-free A exciton transition energy, and a_i and b_i are electronic deformation potentials. In principle, knowing the deformation potentials and the elastic coefficients, the shift of the A free exciton energy position depends linearly on strain [62]. Under the assumption of biaxial stress, the strain tensor components ε_{xx}, ε_{yy}, and ε_{zz} are connected due to Poisson's ratio with the elastic stiffness coefficients C_{ij} of GaN (see section 4.1).

3 Raman spectroscopy

In this chapter the principle of inelastic scattering of monochromatic light - called Raman scattering - is described. At first, phonon modes of wz-GaN and fundamental equations of the phonon polariton in uniaxial crystals are introduced. After a brief description of the classical theory of light scattering a detailed derivation of the Raman scattering efficiency of uniaxial crystals as well as the selection rules in case of wurtzite single crystals are provided.

3.1 Phonon modes in GaN

Initially, Raman spectroscopy was applied in analytical chemistry as a complementary method to infrared (IR) spectroscopy. By measuring the energy of the scattered light relative to the energy of the incident monochromatic light information about the specimen can be deduced. The frequency shift of the inelastically scattered photons depends on the properties of the sample such as chemical bonding, temperature, and strain. In the last decades Raman spectroscopy has been developed as a powerful, non-destructive, and contactless tool for the characterization of condensed matter. In this case, the incident laser light interacts with optical phonons or other elementary excitations (e.g. plasmons or phonon polaritons) in the system. The phonon modes of wz-GaN will be discussed in this section.

As described in section 2.1 the primitive unit cell of hexagonal GaN with space group $C_{6\nu}^4$ contains four atoms. Thus, group theory predicts $3 \times 4 = 12$ phonon normal modes at the Γ point of the Brillouin zone according to the irreducible representation $2A_1 + 2B_1 + 2E_1 + 2E_2$. The modes of E_1 and E_2 symmetry are doubly degenerated. One set of the A_1 and E_1 modes are acoustic, while the remaining $A_1 + 2B_1 + E_1 + 2E_2$ modes are optical ones. The A_1 and E_1 modes are both Raman and infrared (IR) active, the two E_2 modes are only Raman active, and the two B_1 modes are silent ones (neither Raman nor IR active). The atomic displacements of the Raman active phonon modes in wz-GaN are schematically shown in figure 3.1.

The two lattice vibrations with E_2 symmetry are distinguished by subscripts 'low' and 'high'. Since their atomic displacements in the basal plane (perpendicular to the crystals c axis) do not influence the charge distribution within the unit cell these optical modes are nonpolar ones. In contrast, the polar A_1 and E_1 modes split into transverse

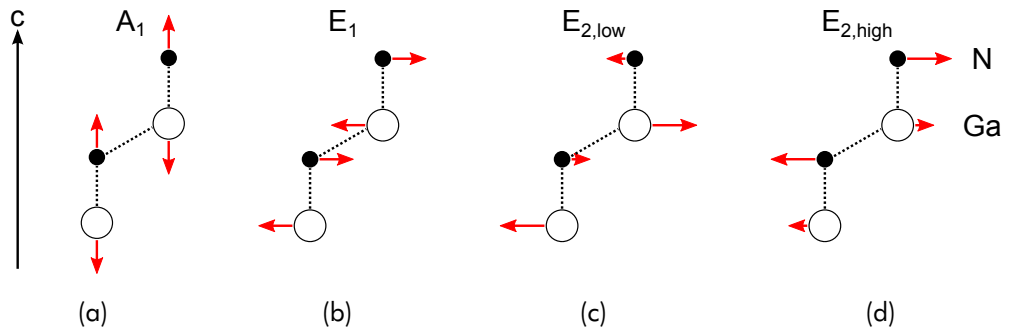

Fig. 3.1: Atomic displacements are schematically depicted for Raman active lattice vibrations in wz-GaN.

optical (TO) and longitudinal optical (LO) phonon modes with different frequencies due to the macroscopic electric field associated with the longitudinal modes. In case of GaN, the electrostatic forces predominate over the anisotropic short-range forces. Therefore, the TO-LO splitting is larger than the A_1-E_1 splitting [64]. For lattice vibrations with A_1 and E_1 symmetry the atomic displacement is parallel and perpendicular to the c axis, respectively, as shown in figure 3.1. Thus, phonons with wavevector angles between 0° and 90° to the c axis have mixed A_1-E_1 character. The directional dispersion will be discussed in section 3.2.3

Since there is an excellent agreement with our experimental data, the phonon frequencies at 300 K reported by Davydov *et al.*[65] were adopted in this work:

$$\begin{array}{lll} \omega_{\mathrm{TO,A1}} = 531.8\ \mathrm{cm}^{-1} & \omega_{\mathrm{TO,E1}} = 558.8\ \mathrm{cm}^{-1} & \omega_{\mathrm{E2,low}} = 144\ \mathrm{cm}^{-1} \\ \omega_{\mathrm{LO,A1}} = 734\ \mathrm{cm}^{-1} & \omega_{\mathrm{LO,E1}} = 741\ \mathrm{cm}^{-1} & \omega_{\mathrm{E2,high}} = 567.6\ \mathrm{cm}^{-1} \end{array}$$

3.2 Phonon polaritons in uniaxial crystals

In polar crystals (e.g. wz-GaN), infrared photons strongly interact with the transverse modes of infrared active phonons (see section 3.1) if their energies are nearly equal. The elementary excitations derived are called phonon polaritons. Their existence has been predicted by Huang [66, 67]. According to the mixed mechanical and electromagnetic nature of the phonon polaritons, one needs equations of both motion and electromagnetic field.
In a first step, Maxwell's equations of electrodynamics will be introduced:

$$\begin{aligned} \nabla \times \vec{E} &= -\dot{\vec{B}}, \\ \nabla \times \vec{H} &= \vec{j} + \dot{\vec{D}}, \\ \nabla \cdot \vec{D} &= \rho, \\ \nabla \cdot \vec{B} &= 0. \end{aligned} \tag{3.1}$$

The electric displacement field $\vec{D}$ is correlated with the electric field $\vec{E}$ and the polarization $\vec{P}$ according to

$$\vec{D} = \varepsilon_0 \tilde{\varepsilon} \cdot \vec{E} = \varepsilon_0 \vec{E} + \vec{P}. \tag{3.2}$$

Here, $\tilde{\varepsilon}(\vec{k}, \omega)$ refers to the dielectric tensor of the medium and ε_0 denotes the permittivity. For nonmagnetic materials the correlation between the magnetic induction $\vec{B}$ and the magnetic field $\vec{H}$ is $\vec{B} = \mu_0 \vec{H}$ with μ_0 being the permeability of the free space. Using the ansatz of plane waves for the electric field $\vec{E} = \vec{E}_0 e^{i(\vec{k} \cdot \vec{r} - \omega t)}$ and the magnetic induction $\vec{B} = \vec{B}_0 e^{i(\vec{k} \cdot \vec{r} - \omega t)}$, and assuming that the medium contains neither free electrical charges ρ nor electrical currents $\vec{j}$, one obtains from the first two rows in equation (3.1)

$$\vec{k} \times \left(\vec{k} \times \vec{E} \right) = \vec{k} \left(\vec{k} \cdot \vec{E} \right) - k^2 \vec{E} = -\omega^2 \varepsilon_0 \mu_0 \, \tilde{\varepsilon} \, \vec{E} = -\frac{\omega^2}{c^2} \tilde{\varepsilon} \, \vec{E}, \tag{3.3}$$

where c equals $(\varepsilon_0 \mu_0)^{-1/2}$ and refers to the velocity of light. Inserting equation (3.3) into equation (3.2) the relation between the electric field $\vec{E}$ and the polarization $\vec{P}$ can be derived:

$$\vec{P} = \varepsilon_0 \vec{E} \left(\frac{c^2 k^2}{\omega^2} - 1 \right) - \frac{\varepsilon_0 c^2}{\omega^2} \vec{k} \left(\vec{k} \cdot \vec{E} \right). \tag{3.4}$$

For purely transverse waves, $\vec{E} \perp \vec{k}$, one obtains

$$\vec{P}_{\mathsf{T}} = \varepsilon_0 \vec{E}_{\mathsf{T}} \left(\frac{c^2 k^2}{\omega^2} - 1 \right), \tag{3.5}$$

and for purely longitudinal waves, $\vec{E} \parallel \vec{k}$, one obtains

$$\vec{P}_{\mathsf{L}} = -\varepsilon_0 \vec{E}_{\mathsf{L}}. \tag{3.6}$$

The following discussion will focus on optically anisotropic media, in particular on the case of a uniaxial crystal (e.g. wz-GaN). The three principal directions are denoted by the three cartesian coordinates x, y, and z.

The uniaxial crystal is characterized by dielectric functions which are identical for two principal directions:

$$\varepsilon_{11}(\omega) = \varepsilon_{22}(\omega) = \varepsilon_{\perp}(\omega) \tag{3.7}$$

These directions describe the optically isotropic plane. The third principal direction perpendicular to this plane is referred to as the optical axis c with the dielectric function

$$\varepsilon_{33}(\omega) = \varepsilon_{\parallel}(\omega) \tag{3.8}$$

The equations of motion for phonon polaritons will be written in a form first claimed by Huang for the description of cubic diatomic crystals with one polar mode [66, 67]. In the case of a uniaxial crystal and arbitrary direction of the wavevector $\vec{k}$ the vectors $\vec{Q}$ (generalized coordinate displacement), $\vec{E}$ (electric field strength), and

$\vec{P}$ (polarization) of the Born-Huang equations can be split into linearly independent ordinary and extraordinary components lying either perpendicularly to or in the plane spanned by the wavevector and the optical axis, respectively (see figure 3.2). As the (x, y) plane is isotropic, it will be assumed without loss of generality that the wavevector lies in the (x, z) plane and that the displacement of the ordinary transverse mode is parallel to the y direction. The extraordinary parts of $\vec{Q}$, $\vec{E}$, and $\vec{P}$ are decomposed in components parallel and perpendicular to the z axis. This is shown in figure 3.2 for the displacement vector $\vec{Q}$ as an example.

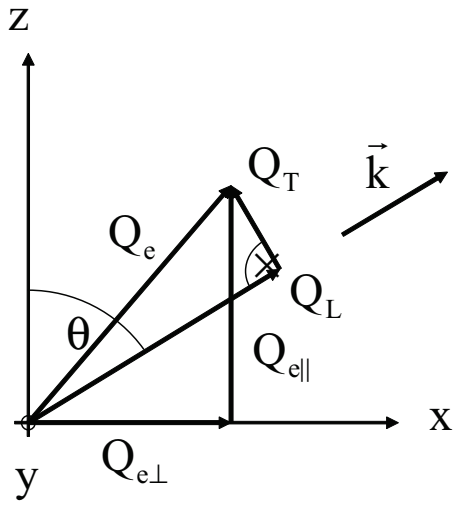

Fig. 3.2: Displacement components of the extraordinary phonon polariton Q_{e} which are decomposed into parts either parallel ($Q_{\mathsf{e}\parallel}$) and perpendicular ($Q_{\mathsf{e}\perp}$) to the optical axis or parallel (L*ongitudinal*) and perpendicular (T*ransverse*) to the wavevector $\vec{k}$. The same procedure can be adopted for $\vec{E}$ and $\vec{P}$. Reprinted figure with permission from [68]. Copyright 2013 American Physical Society.

With time dependence of the displacement vector in the form $\vec{Q} = \vec{Q}_0 e^{i\omega t}$ and without damping, one obtains for the ordinary phonon polaritons:

$$\begin{aligned} -\omega^2 Q_{\mathsf{o}\perp} &= B^{11}_{\mathsf{o}\perp} Q_{\mathsf{o}\perp} + B^{12}_{\mathsf{o}\perp} E_{\perp}, \\ P_{\mathsf{o}\perp} &= B^{21}_{\mathsf{o}\perp} Q_{\mathsf{o}\perp} + B^{22}_{\mathsf{o}\perp} E_{\perp}, \end{aligned} \tag{3.9}$$

and for the extraordinary phonon polaritons:

$$\begin{aligned} -\omega^2 Q_{\mathsf{e}\perp} &= B^{11}_{\mathsf{e}\perp} Q_{\mathsf{e}\perp} + B^{12}_{\mathsf{e}\perp} E_{\perp}, \\ P_{\mathsf{e}\perp} &= B^{21}_{\mathsf{e}\perp} Q_{\mathsf{e}\perp} + B^{22}_{\mathsf{e}\perp} E_{\perp}, \\ -\omega^2 Q_{\mathsf{e}\parallel} &= B^{11}_{\mathsf{e}\parallel} Q_{\mathsf{e}\parallel} + B^{12}_{\mathsf{e}\parallel} E_{\parallel}, \\ P_{\mathsf{e}\parallel} &= B^{21}_{\mathsf{e}\parallel} Q_{\mathsf{e}\parallel} + B^{22}_{\mathsf{e}\parallel} E_{\parallel}. \end{aligned} \tag{3.10}$$

In order to determine the nine variables in equations (3.9) and (3.10) three equations are additionally needed. The relationship between the electric field $\vec{E}$ and the polarization $\vec{P}$ was derived from Maxwell's equations (see equation (3.4)).

The coefficients B in equations (3.9) and (3.10) can be interpreted macroscopically. In the following sections they will be replaced by the coefficients $a_\perp$, $b_\perp$, $a_\parallel$, and $b_\parallel$ which can be expressed using measurable parameters (see, for instance, [69]): for transverse phonons in the principal directions with $c^2k^2/\omega^2 \gg 1$, it can be seen that

$$\begin{aligned} B^{11}_{\mathsf{o}\perp} = B^{11}_{\mathsf{e}\perp} &= -\omega^2_{\mathsf{T}\perp}, \\ B^{11}_{\mathsf{e}\parallel} &= -\omega^2_{\mathsf{T}\parallel}. \end{aligned} \tag{3.11}$$

For large frequencies ω the amplitudes of the normal coordinates $Q_{\mathsf{o}\perp}$, $Q_{\mathsf{e}\perp}$, and $Q_{\mathsf{e}\parallel}$ vanish, and following $P_{\mathsf{o}\perp} = B^{22}_{\mathsf{o}\perp}E_{\mathsf{o}\perp} = \varepsilon_0(\varepsilon_{\infty\perp} - 1)E_{\mathsf{o}\perp}$, $P_{\mathsf{e}\perp} = B^{22}_{\mathsf{e}\perp}E_{\mathsf{e}\perp} = \varepsilon_0(\varepsilon_{\infty\perp} - 1)E_{\mathsf{e}\perp}$, and $P_{\mathsf{e}\parallel} = B^{22}_{\mathsf{e}\parallel}E_{\mathsf{e}\parallel} = \varepsilon_0(\varepsilon_{\infty\parallel} - 1)E_{\mathsf{e}\parallel}$ one gets

$$\begin{aligned} B^{22}_{\mathsf{o}\perp} = B^{22}_{\mathsf{e}\perp} = b_\perp &= \varepsilon_0\left(\varepsilon_{\infty\perp} - 1\right), \\ B^{22}_{\mathsf{e}\parallel} = b_\parallel &= \varepsilon_0\left(\varepsilon_{\infty\parallel} - 1\right). \end{aligned} \tag{3.12}$$

In the static case ($\omega = 0$), one obtains for the ordinary modes from $Q_{\mathsf{o}\perp} = -\left(B^{12}_{\mathsf{o}\perp}/B^{11}_{\mathsf{o}\perp}\right)E_{\mathsf{o}\perp}$ and $P_{o\perp} = \left[-\left(B^{12}_{o\perp}B^{21}_{o\perp}/B^{11}_{\mathsf{o}\perp}\right) + B^{22}_{\mathsf{o}\perp}\right]E_{\mathsf{o}\perp}$, analog equations for the extraordinary modes, and with equations (3.11) and (3.12)

$$\begin{aligned} B^{12}_{\mathsf{o}\perp} = B^{21}_{\mathsf{o}\perp} = B^{12}_{\mathsf{e}\perp} = B^{21}_{\mathsf{e}\perp} &= a_\perp \\ &= \omega_{\mathsf{T}\perp}\sqrt{\varepsilon_0\left(\varepsilon_{\mathsf{s}\perp} - \varepsilon_{\infty\perp}\right)} = \sqrt{\varepsilon_0\varepsilon_{\infty\perp}\left(\omega^2_{\mathsf{L}\perp} - \omega^2_{\mathsf{T}\perp}\right)}, \\ B^{12}_{\mathsf{e}\parallel} = B^{21}_{\mathsf{e}\parallel} &= a_\parallel \\ &= \omega_{\mathsf{T}\parallel}\sqrt{\varepsilon_0\left(\varepsilon_{\mathsf{s}\parallel} - \varepsilon_{\infty\parallel}\right)} = \sqrt{\varepsilon_0\varepsilon_{\infty\parallel}\left(\omega^2_{\mathsf{L}\parallel} - \omega^2_{\mathsf{T}\parallel}\right)}. \end{aligned} \tag{3.13}$$

$\omega_{\mathsf{T}\perp}$ ($\omega_{\mathsf{T}\parallel}$) indicates the frequency of the transverse phonon propagating in the (x, y) plane (parallel to the z axis). $\omega_{\mathsf{L}\perp}$ ($\omega_{\mathsf{L}\parallel}$) refers to the frequency of the longitudinal phonon propagating in the (x, y) plane (parallel to the z axis). $\varepsilon_{\mathsf{s}\perp}$ ($\varepsilon_{\infty\perp}$) denotes the static (high-frequency) dielectric constant in the (x, y) plane, and $\varepsilon_{\mathsf{s}\parallel}$ ($\varepsilon_{\infty\parallel}$) the static (high-frequency) dielectric constant parallel to the z axis. In case of wz-GaN, the following set of static [70] and high-frequency [71] dielectric constants were adopted in this work:

$$\begin{aligned} \varepsilon_{\mathsf{s}\perp} &= 9.28 & \varepsilon_{\infty\perp} &= 5.14 \\ \varepsilon_{\mathsf{s}\parallel} &= 10.1 & \varepsilon_{\infty\parallel} &= 5.31 \end{aligned}$$

Moreover, in equation (3.13) Lyddane-Sachs-Teller relations were used:

$$\begin{aligned} \frac{\omega^2_{\mathsf{L}\perp}}{\omega^2_{\mathsf{T}\perp}} &= \frac{\varepsilon_{\mathsf{s}\perp}}{\varepsilon_{\infty\perp}}, \\ \frac{\omega^2_{\mathsf{L}\parallel}}{\omega^2_{\mathsf{T}\parallel}} &= \frac{\varepsilon_{\mathsf{s}\parallel}}{\varepsilon_{\infty\parallel}}. \end{aligned} \tag{3.14}$$

3.2.1 Ordinary phonon polaritons

In order to solve the three equations (3.9) and (3.5), one combines $Q_{\mathsf{o}\perp}$, $E_{\mathsf{o}\perp}$, and $P_{\mathsf{o}\perp}$ to a vector $\vec{X}_{\mathsf{o}}$. The set of equations can then be written as

$$\tilde{M}_{\mathsf{o}} \cdot \vec{X}_{\mathsf{o}} = 0 \tag{3.15}$$

with the matrix

$$\tilde{M}_{\mathsf{o}} = \begin{pmatrix} \omega^2 - \omega_{\mathsf{T}\perp}^2 & a_\perp & 0 \\ a_\perp & b_\perp & -1 \\ 0 & \varepsilon_0 \left(\frac{c^2 k^2}{\omega^2} - 1 \right) & -1 \end{pmatrix}.$$

Nontrivial solutions of the equations are obtained with $\det(\tilde{M}_{\mathsf{o}}) = 0$. This leads to the equation

$$\varepsilon_{\infty\perp}\omega^4 - \omega^2 c^2 k^2 - \varepsilon_{\infty\perp}\omega^2\omega_{\mathsf{L}\perp}^2 + c^2 k^2 \omega_{\mathsf{T}\perp}^2 = 0. \tag{3.16}$$

This equation can also be written as

$$\frac{c^2 k^2}{\omega^2} = \varepsilon_\perp(\omega) = \varepsilon_{\infty\perp} \left(1 + \frac{\omega_{\mathsf{L}\perp}^2 - \omega_{\mathsf{T}\perp}^2}{\omega_{\mathsf{T}\perp}^2 - \omega^2} \right), \tag{3.17}$$

where $\varepsilon_\perp(\omega)$ is the dielectric function for propagation in the optically isotropic plane. Equation (3.16) is a quadratic equation in ω^2. Its solution gives two polariton branches which do not depend on the angle θ (see section 7.1).

3.2.2 Extraordinary phonon polaritons

It is convenient to change the coordinate system and express the vectors $\vec{Q}$, $\vec{E}$, and $\vec{P}$ in components parallel (L*ongitudinal*) and perpendicular (T*ransverse*) to the wavevector $\vec{k}$ (figure 3.2). Thus, the polarization can be easily expressed by components parallel to the corresponding electric field components (see equations (3.5) and (3.6)). In order to solve the six equations (3.10), (3.5), and (3.6), one combines the transformed components $Q_{\mathsf{e}\perp}$, $E_{\mathsf{e}\perp}$, $P_{\mathsf{e}\perp}$, $Q_{\mathsf{e}\parallel}$, $E_{\mathsf{e}\parallel}$, and $P_{\mathsf{e}\parallel}$ to a vector $\vec{X}_{\mathsf{e}}$ and writes the set of equations in the form

$$\tilde{M}_{\mathsf{e}} \cdot \vec{X}_{\mathsf{e}} = 0 \tag{3.18}$$

with the matrix

$$\tilde{M}_{\mathsf{e}} = \begin{pmatrix} -\left(\omega^2 - \omega_{\mathsf{T}\perp}^2\right)\cos\theta & -a_\perp \cos\theta & 0 & \left(\omega^2 - \omega_{\mathsf{T}\perp}^2\right)\sin\theta & a_\perp \sin\theta & 0 \\ -a_\perp \cos\theta & -b_\perp \cos\theta & \cos\theta & a_\perp \sin\theta & b_\perp \sin\theta & -\sin\theta \\ 0 & \varepsilon_0 \left(1 - \frac{c^2 k^2}{\omega^2}\right) & 1 & 0 & 0 & 0 \\ \left(\omega^2 - \omega_{\mathsf{T}\parallel}^2\right)\sin\theta & a_\parallel \sin\theta & 0 & \left(\omega^2 - \omega_{\mathsf{T}\parallel}^2\right)\cos\theta & a_\parallel \cos\theta & 0 \\ a_\parallel \sin\theta & b_\parallel \sin\theta & -\sin\theta & a_\parallel \cos\theta & b_\parallel \cos\theta & -\cos\theta \\ 0 & 0 & 0 & 0 & \varepsilon_0 & 1 \end{pmatrix}.$$

Nontrivial solutions of this homogeneous equation system for the six variables Q_{T}, E_{T}, P_{T}, Q_{L}, E_{L}, and P_{L} are obtained for a vanishing determinant of $\tilde{M}_{\mathsf{e}}$. This leads to the equation

$$\left(\frac{c^2k^2}{\omega^2}\right) \cdot \left(\varepsilon_\perp(\omega) \cdot \sin^2\theta + \varepsilon_\parallel(\omega) \cdot \cos^2\theta\right) - \varepsilon_\perp(\omega) \cdot \varepsilon_\parallel(\omega) = 0, \tag{3.19}$$

where $\varepsilon_\perp(\omega)$ and $\varepsilon_\parallel(\omega)$ are the dielectric functions for propagation in the optically isotropic plane and parallel to the c axis of the uniaxial crystal, respectively. $\varepsilon_\perp(\omega)$ is given by equation (3.17) and $\varepsilon_\parallel(\omega)$ is defined by

$$\varepsilon_\parallel(\omega) = \varepsilon_{\infty\parallel}\left(1 + \frac{\omega_{\mathsf{L}\parallel}^2 - \omega_{\mathsf{T}\parallel}^2}{\omega_{\mathsf{T}\parallel}^2 - \omega^2}\right). \tag{3.20}$$

Equation (3.19) describes the directional dispersion as well as the dispersion as a function of the wavevector. It is cubic in ω^2 and can be solved analytically using Cardano's formula [72]. The three real solutions describe the three branches of the extraordinary polaritons (see section 7.1).

3.2.3 Directional dispersion

For large wavevectors (10^4 cm$^{-1} < k < 10^6$ cm^{-1}) the polaritons are phononlike. Assuming $k \to \infty$, one obtains from equation (3.19):

$$\varepsilon_\perp(\omega) \cdot \sin^2\theta + \varepsilon_\parallel(\omega) \cdot \cos^2\theta = 0. \tag{3.21}$$

The solution of this quadratic equation in ω^2 yields two extraordinary polariton (phonon) branches depending on the angle θ including the wavevector and the c axis of the crystal. Figure 3.3 illustrates the directional dispersion of the two extraordinary modes. The ordinary phonon of E_1 symmetry and TO character as well as the nonpolar mode $\mathsf{E}_{2,\mathsf{high}}$ do not exhibit a directional dispersion. The $\mathsf{E}_{2,\mathsf{low}}$ phonon mode at 144 cm^{-1} which is also independent on the angle θ is not shown in this figure.

In order to describe the directional dependence, the Poulet-Loudon approximation [73, 74] is a simple expression used in the literature:

$$\begin{aligned} \omega_{\mathsf{TO}}^2(\theta) &= \omega_{\mathsf{TO,E1}}^2 \cdot \cos^2\theta + \omega_{\mathsf{TO,A1}}^2 \cdot \sin^2\theta, \\ \omega_{\mathsf{LO}}^2(\theta) &= \omega_{\mathsf{LO,A1}}^2 \cdot \cos^2\theta + \omega_{\mathsf{LO,E1}}^2 \cdot \sin^2\theta. \end{aligned} \tag{3.22}$$

In the case of wz-GaN, these approximations work very well and practically coincide with the exact solutions shown in figure 3.3.

3.3 Classical theory of light scattering in solids

The Raman effect describes the inelastic scattering of light and was theoretically predicted by A. Smekal in 1923 [75]. Investigating optical scattering of liquids the Raman effect was experimentally revealed by the Indian physicists C. V. Raman and

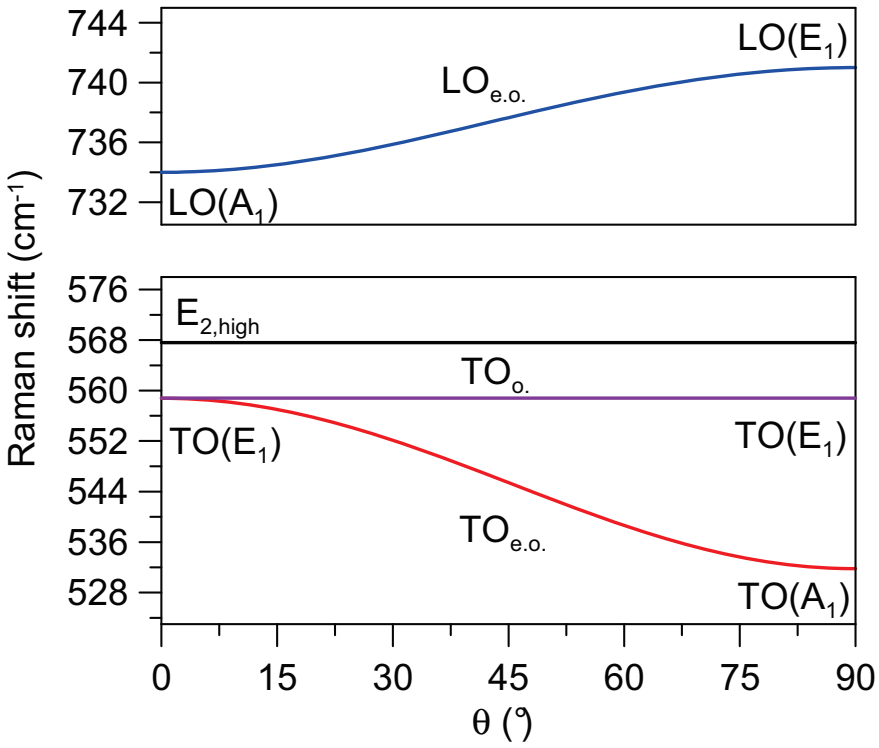

Fig. 3.3: Optical phonon modes of wz-GaN. The directional dispersion of the extraordinary (e.o.) polar modes as function of the angle θ between the phonon wavevector and the c axis of the crystal is shown. The ordinary (o.) transverse phonon of E_1 symmetry exhibits no directional dispersion.

K. S. Krishnan [76] in 1928. Independently, the Russian academics G. Landsberg and L. Mandelstam [77] observed this effect in condensed matter nearly at the same time. C. V. Raman was awarded the Nobel prize for physics in 1930 for this discovery.

The origin of Raman scattering in crystals can be understood within the classical theory of light scattering. For further reading and details see standard textbooks [30, 78–80].

The atomic vibrations relative to an equilibrium position are correlated and can be classified as normal modes. The energy of the normal modes is restricted to integer multiples of a quantum of energy. The elementary excitation derived is called phonon. Mathematically, the displacement of the atoms can be expressed using the vector of the generalized coordinate $\vec{Q}_\mathrm{N}$ for the N$^{\mathrm{th}}$ phonon mode at a position $\vec{r}$ and time t:

$$\vec{Q}_\mathrm{N}(\vec{r},t) = \vec{Q}_0 e^{\pm i(\vec{k}_\mathrm{N}\cdot\vec{r}-\omega_\mathrm{N}t)}. \tag{3.23}$$

Here, $\vec{Q}_0$ is the amplitude, $\vec{k}_\mathrm{N}$ denotes the wavevector and ω_N refers to the eigenfrequency of the N$^{\mathrm{th}}$ normal mode. As a result of the collective oscillation, the dielectric susceptibility tensor $\tilde{\chi}$ of the crystal will also change periodically. Since the atomic dis-

placements are assumed to be small compared to the lattice constants, the dielectric susceptibility can be expanded as a Taylor series with respect to Q_N:

$$\chi = \chi_0 + \sum_\mathsf{N} \left\{ \left(\frac{\partial \chi}{\partial Q_\mathsf{N}} \right)_0 Q_\mathsf{N} + \text{higher-order terms} \right\}, \tag{3.24}$$

where the sum runs over all normal coordinates. $\partial\chi/\partial Q_\mathsf{N}$ denotes the coefficients of the atomic displacement tensor describing the contribution of the normal coordinates to the changes $\delta\chi$ of the susceptibility tensor. This approach is valid for nonpolar phonon modes and transverse optical modes with wavevector values in the range 10^5 cm$^{-1} < k < 10^8$ cm^{-1}. In case of longitudinal phonon modes the contribution of the electric field components related to the coefficients of the electro-optic tensor $\partial\chi/\partial E_\mathsf{N}$ has to be taken into account additionally (see section 3.4).

The dielectric susceptibility tensor $\tilde{\chi}$ describes the polarization of a material in an electromagnetic field. The induced polarization $\vec{P}$ is given by:

$$\vec{P} = \varepsilon_0 \tilde{\chi} \vec{E}. \tag{3.25}$$

Using the ansatz of plane waves for the electric field $\vec{E} = \vec{E}_0 e^{i\left(\vec{k}\cdot\vec{r}-\omega t\right)}$ and inserting the zero and first order terms of equation (3.24) in equation (3.25), the relation between the polarization $\vec{P}$ and the electric field $\vec{E}$ can be rewritten as:

$$\vec{P} = \varepsilon_0 \chi_0 \cdot \vec{E}_0 e^{i\left(\vec{k}_\mathsf{L}\cdot\vec{r}-\omega_\mathsf{L} t\right)} + \varepsilon_0 \vec{E}_0 \cdot \sum_\mathsf{N} \left\{ \left(\frac{\partial \chi}{\partial Q_\mathsf{N}} \right)_0 \vec{Q}_0 e^{i\left[\left(\vec{k}_\mathsf{L} \pm \vec{k}_\mathsf{N}\right)\cdot\vec{r}-(\omega_\mathsf{L}\pm\omega_\mathsf{N})t\right]} \right\}. \tag{3.26}$$

The first term of this equation refers to the elastic scattering of light (Rayleigh scattering[1]) where frequency and wavevector of the scattered light equal the frequency ω_L and wavevector $\vec{k}_\mathsf{L}$ of the incident (laser) light, respectively. The second term represents the inelastic scattering components indicating the Stokes and anti-Stokes processes.

Figure 3.4 illustrates the interaction of any scattering system and the incident radiation as vibrational transition between quantized energy levels. Possible inelastic scattering processes are depicted by energy level schemes, where $\mathsf{E_i}$ and $\mathsf{E_f}$ refer to the energy of the initial and final eigenstate, respectively. Generally, the Stokes process describes a generation of a vibrational eigenstate. The frequency ω_S and wavevector $\vec{k}_\mathsf{S}$ of the scattered light are slightly reduced with respect to the incident (laser) light by the amount of the characteristic eigenfrequency ω_N and wavevector $\vec{k}_\mathsf{N}$ of the N$^{\text{th}}$ normal phonon mode, respectively. The anti-Stokes scattering refers to the annihilation of such an elementary excitation. Thus, frequency and wavevector of the scattered light are increased compared to the incident light.

[1] named after the British physicist Lord Rayleigh (1842-1919)

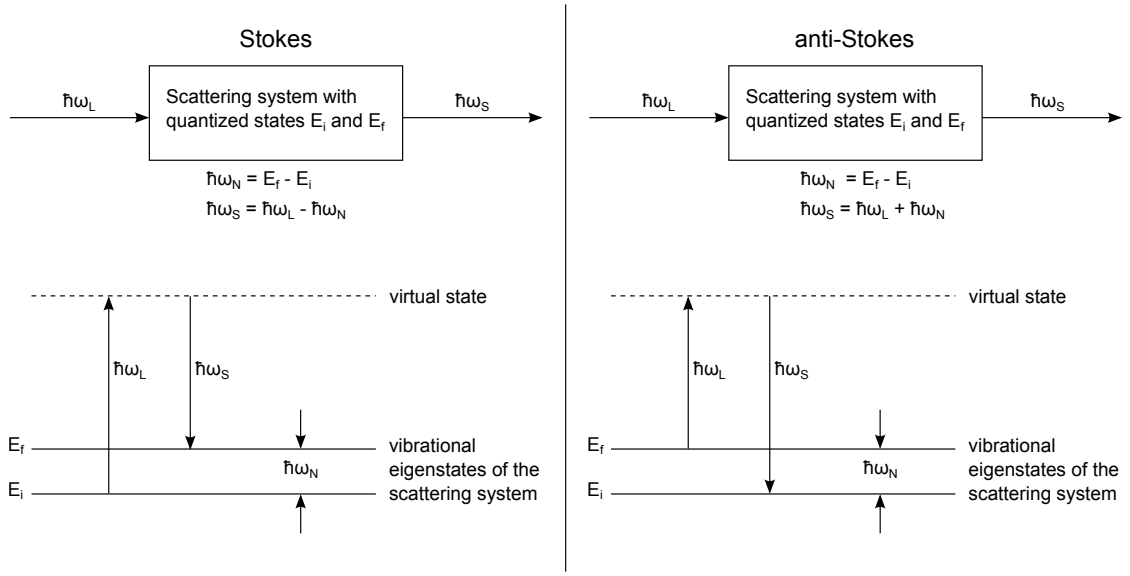

Fig. 3.4: Inelastic scattering processes. The observed energy of the scattered light $\hbar\omega_S$ relative to the energy of the incident light $\hbar\omega_L$ depends on the detected transition between vibrational eigenstates E_i and E_f of the scattering system. The characteristic eigenenergy of the generated (Stokes) or annihilated (anti-Stokes) elementary excitation is indicated by $\hbar\omega_N$.

For both, the anti-Stokes and Stokes scattering processes inside the crystal (introducing an additional index 'i') wavevector conservation requires

$$\vec{k}_{iS} = \vec{k}_{iL} \pm \vec{k}_N, \tag{3.27}$$

and energy conservation requires

$$\hbar\omega_S = \hbar\omega_L \pm \hbar\omega_N \qquad \text{or} \qquad \frac{1}{\lambda_S} = \frac{1}{\lambda_L} \pm \bar{\omega_R}, \tag{3.28}$$

where λ_L and λ_S denote the wavelength of incident and scattered light outside the crystal, respectively, and $\bar{\omega_R}$ refers to the Raman shift expressed in cm^{-1}. For practical reasons, ω indicates the Raman shift in the following.

3.4 Raman scattering efficiency

Due to polarization selection rules, not all available normal modes (phonons) of the crystal simultaneously contribute to the observable Raman scattered light for an applied incident electromagnetic field. The Raman scattering efficiency per unit angle $dS/d\Omega$ of the phonons travelling the distance L in the crystal through the volume V can be written as [81]

$$\frac{dS}{d\Omega} = \left(\frac{\omega_S}{c}\right)^4 VL \left| \langle 1 + n_\omega | \sum_{\mu,\nu=1}^{3} e_\mu^S \delta\chi_{\mu\nu} e_\nu^L | n_\omega \rangle \right|^2, \tag{3.29}$$

where e_ν^{L} (e_μ^{S}) are the unit vectors in direction of polarization of the incident (scattered) light, respectively. The term inside the absolute value signs is the matrix element of an operator between the state with n_ω phonons of frequency ω present and the state with $n_\omega + 1$ phonons describing a Stokes scattering process. Thus, the scattered photon emerges with the frequency ω_{S}, less than that of the incident photon by the small amount ω ($\bar{\omega}_{\mathsf{R}}$ in equation (3.28)). $n_\omega = 1/\left[\exp(\hbar\omega/kT) - 1\right]$ refers to the Bose-Einstein factor.

First, the three polar phonon modes of hexagonal crystals with point group C_{6v} which are Raman as well as infrared active are considered (see section 3.1). Their Raman scattering intensity depends on the changes $\delta\chi$ of the polarizability tensor elements with contributions of the normal coordinates and the electric field components

$$\begin{aligned}
\delta\chi_{ij}^N &= \frac{\partial\chi_{ij}}{\partial Q_N} Q_N + \frac{\partial\chi_{ij}}{\partial E_N} E_N \\
&= \left[\frac{\partial\chi_{ij}}{\partial Q_N} + \frac{(\omega_{\mathsf{T}N}^2 - \omega^2)}{\omega_{\mathsf{T}N}\sqrt{\varepsilon_0(\varepsilon_{\mathsf{s}N} - \varepsilon_{\infty N})}} \frac{\partial\chi_{ij}}{\partial E_N}\right] Q_N \\
&= \left\{\sum_{\alpha=1}^{3}\left[\frac{\partial\chi_{ij}}{\partial Q_\alpha}\frac{\partial Q_\alpha}{\partial Q_N} + \frac{(\omega_{\mathsf{T}N}^2 - \omega^2)}{\omega_{\mathsf{T}N}\sqrt{\varepsilon_0(\varepsilon_{\mathsf{s}N} - \varepsilon_{\infty N})}} \frac{\partial\chi_{ij}}{\partial E_\alpha}\frac{\partial E_\alpha}{\partial E_N}\right]\right\} Q_N \\
&= \sum_{\alpha=1}^{3}\left[\frac{\partial\chi_{ij}}{\partial Q_\alpha}\cdot\frac{\partial Q_\alpha}{\partial Q_N}\cdot\left(1 + \frac{\omega_{\mathsf{TO},\alpha}^2 - \omega^2}{C_{\alpha,ij}^{\mathsf{FH}}\cdot\omega_{\mathsf{TO},\alpha}^2}\right)\right] Q_N.
\end{aligned} \tag{3.30}$$

The letter N denotes the ordinary transverse, extraordinary transverse and the extraordinary longitudinal phonon with the normal coordinates Q_{To}, Q_{Te}, Q_{Le} and the electric fields E_{To}, E_{Te}, E_{Le}, respectively. The relation between E_N and Q_N follows from the Born-Huang equations (3.9) and (3.10) given in section 3.2.

$$\begin{aligned}
Q_{\mathsf{To}} &= \frac{\omega_{\mathsf{T}\perp}\sqrt{\varepsilon_0\left(\varepsilon_{\mathsf{s}\perp} - \varepsilon_{\infty\perp}\right)}}{\omega_{\mathsf{T}\perp}^2 - \omega^2}\, E_{\mathsf{To}}, \\
Q_{\mathsf{Te}} &= \frac{\omega_{\mathsf{T}\perp}\sqrt{\varepsilon_0\left(\varepsilon_{\mathsf{s}\perp} - \varepsilon_{\infty\perp}\right)}}{\omega_{\mathsf{T}\perp}^2 - \omega^2}\, E_{\mathsf{Te}}, \\
Q_{\mathsf{Le}} &= \frac{\omega_{\mathsf{T}\parallel}\sqrt{\varepsilon_0\left(\varepsilon_{\mathsf{s}\parallel} - \varepsilon_{\infty\parallel}\right)}}{\omega_{\mathsf{T}\parallel}^2 - \omega^2}\, E_{\mathsf{Le}}.
\end{aligned} \tag{3.31}$$

The normal coordinates are decomposed introducing the angles φ and θ which define the direction of the wavevector $\vec{k} = k\ (\sin\theta\cdot\cos\varphi,\ \sin\theta\cdot\sin\varphi,\ \cos\theta)$. The direction of the three normal coordinates $\vec{Q}_{\mathsf{To}}\perp\vec{Q}_{\mathsf{Te}}\perp\vec{Q}_{\mathsf{Le}}$ is given by $\vec{Q}_{\mathsf{To}}\perp(z$ axis, $\vec{k})$, $\vec{Q}_{\mathsf{Te}}\perp(\vec{k},\ \vec{Q}_{\mathsf{To}})$, and $\vec{Q}_{\mathsf{Le}} \parallel \vec{k}$:

$$\begin{aligned}
\vec{Q}_{\mathsf{To}} &= -\sin\varphi\ Q_x\,\vec{e}_x + \cos\varphi\ Q_y\,\vec{e}_y, \\
\vec{Q}_{\mathsf{Te}} &= -\cos\varphi\cos\theta\ Q_x\,\vec{e}_x - \sin\varphi\cos\theta\ Q_y\,\vec{e}_y + \sin\theta\ Q_z\,\vec{e}_z, \\
\vec{Q}_{\mathsf{Le}} &= \cos\varphi\sin\theta\ Q_x\,\vec{e}_x + \sin\varphi\sin\theta\ Q_y\,\vec{e}_y + \cos\theta\ Q_z\,\vec{e}_z.
\end{aligned} \tag{3.32}$$

In equation (3.30) the cartesian coordinates x, y, and z are numbered in sequence by α. The frequencies of the transverse phonon polarized in the (x, y) plane (parallel to the z axis) are indicated by $\omega_{\mathsf{TO},1} = \omega_{\mathsf{TO},2} = \omega_{\mathsf{TO,E1}}$ ($\omega_{\mathsf{TO},3} = \omega_{\mathsf{TO,A1}}$).

Using equation (3.32) the components of the atomic displacement tensor can be expressed as:

$$\begin{aligned}
\frac{\partial \chi_{ij}}{\partial Q_{\mathsf{To}}} &= \frac{\partial \chi_{ij}}{\partial Q_x}\frac{\partial Q_x}{\partial Q_{\mathsf{To}}} + \frac{\partial \chi_{ij}}{\partial Q_y}\frac{\partial Q_y}{\partial Q_{\mathsf{To}}} + \frac{\partial \chi_{ij}}{\partial Q_z}\frac{\partial Q_z}{\partial Q_{\mathsf{To}}} \\
&= -\frac{\partial \chi_{ij}}{\partial Q_x}\sin\varphi + \frac{\partial \chi_{ij}}{\partial Q_y}\cos\varphi, \\
\frac{\partial \chi_{ij}}{\partial Q_{\mathsf{Te}}} &= \frac{\partial \chi_{ij}}{\partial Q_x}\frac{\partial Q_x}{\partial Q_{\mathsf{Te}}} + \frac{\partial \chi_{ij}}{\partial Q_y}\frac{\partial Q_y}{\partial Q_{\mathsf{Te}}} + \frac{\partial \chi_{ij}}{\partial Q_z}\frac{\partial Q_z}{\partial Q_{\mathsf{Te}}} \\
&= -\frac{\partial \chi_{ij}}{\partial Q_x}\cos\theta\cdot\cos\varphi - \frac{\partial \chi_{ij}}{\partial Q_y}\cos\theta\cdot\sin\varphi + \frac{\partial \chi_{ij}}{\partial Q_z}\sin\theta, \\
\frac{\partial \chi_{ij}}{\partial Q_{\mathsf{Le}}} &= \frac{\partial \chi_{ij}}{\partial Q_x}\frac{\partial Q_x}{\partial Q_{\mathsf{Le}}} + \frac{\partial \chi_{ij}}{\partial Q_y}\frac{\partial Q_y}{\partial Q_{\mathsf{Le}}} + \frac{\partial \chi_{ij}}{\partial Q_z}\frac{\partial Q_z}{\partial Q_{\mathsf{Le}}} \\
&= \frac{\partial \chi_{ij}}{\partial Q_x}\sin\theta\cdot\cos\varphi + \frac{\partial \chi_{ij}}{\partial Q_y}\sin\theta\cdot\sin\varphi + \frac{\partial \chi_{ij}}{\partial Q_z}\cos\theta.
\end{aligned} \tag{3.33}$$

Similarly, the components of the electro-optic tensor are obtained. The coefficients of the electro-optic tensor are related to those of the second harmonic generation tensor $d_{\alpha,ij}$ [82]:

$$\frac{\partial \chi_{ij}}{\partial E_\alpha} = 4\, d_{\alpha,ij}. \tag{3.34}$$

According to Claus *et al.*[69][2], the Raman tensors for polar modes in hexagonal crystals with point group C_{6v} have the following form:

$$\begin{aligned}
\alpha = 1,\ E_1(x):\quad & \frac{\partial \chi_{ij}}{\partial Q_x} = \begin{pmatrix} 0 & 0 & c_{\mathsf{TO}} \\ 0 & 0 & 0 \\ c_{\mathsf{TO}} & 0 & 0 \end{pmatrix}, \qquad \frac{\partial \chi_{ij}}{\partial E_x} = \begin{pmatrix} 0 & 0 & c_{\mathsf{e}} \\ 0 & 0 & 0 \\ c_{\mathsf{e}} & 0 & 0 \end{pmatrix}, \\
\alpha = 2,\ E_1(y):\quad & \frac{\partial \chi_{ij}}{\partial Q_y} = \begin{pmatrix} 0 & 0 & 0 \\ 0 & 0 & c_{\mathsf{TO}} \\ 0 & c_{\mathsf{TO}} & 0 \end{pmatrix}, \qquad \frac{\partial \chi_{ij}}{\partial E_y} = \begin{pmatrix} 0 & 0 & 0 \\ 0 & 0 & c_{\mathsf{e}} \\ 0 & c_{\mathsf{e}} & 0 \end{pmatrix}, \\
\alpha = 3,\ A_1(z):\quad & \frac{\partial \chi_{ij}}{\partial Q_z} = \begin{pmatrix} a_{\mathsf{TO}} & 0 & 0 \\ 0 & a_{\mathsf{TO}} & 0 \\ 0 & 0 & b_{\mathsf{TO}} \end{pmatrix}, \qquad \frac{\partial \chi_{ij}}{\partial E_z} = \begin{pmatrix} a_{\mathsf{e}} & 0 & 0 \\ 0 & a_{\mathsf{e}} & 0 \\ 0 & 0 & b_{\mathsf{e}} \end{pmatrix}.
\end{aligned} \tag{3.35}$$

[2] The authors corrected some errors appearing in older tables.

The relation between the electro-optic tensor components $\left(\frac{\partial \chi_{ij}}{\partial E_\alpha}\right)$ and the atomic displacement tensor components $\left(\frac{\partial \chi_{ij}}{\partial Q_\alpha}\right)$ can be expressed using the Faust-Henry [29] coefficients which were introduced in equation (3.30):

$$C^{\mathsf{FH}}_{\alpha,ij} = \frac{\sqrt{\varepsilon_0(\varepsilon_{\mathsf{s}\alpha} - \varepsilon_{\infty\alpha})}}{\omega_{\mathsf{TO},\alpha}} \cdot \frac{\left(\frac{\partial \chi_{ij}}{\partial Q_\alpha}\right)}{\left(\frac{\partial \chi_{ij}}{\partial E_\alpha}\right)}, \tag{3.36}$$

where $\varepsilon_{\mathsf{s}1} = \varepsilon_{\mathsf{s}2} = \varepsilon_{\mathsf{s}\perp}$ ($\varepsilon_{\infty 1} = \varepsilon_{\infty 2} = \varepsilon_{\infty\perp}$) denotes the static (high-frequency) dielectric constant in the (x, y) plane, and $\varepsilon_{\mathsf{s}3} = \varepsilon_{\mathsf{s}\parallel}$ ($\varepsilon_{\infty 3} = \varepsilon_{\infty\parallel}$) the static (high-frequency) dielectric constant parallel to the z axis (see section 3.2). According to the symmetry of the tensors in equation (3.35), three different Faust-Henry coefficients will appear:

$$\begin{aligned} C^{\mathsf{FH}}_c &= C^{\mathsf{FH}}_{1,31} = C^{\mathsf{FH}}_{1,13} = C_{2,23} = C^{\mathsf{FH}}_{2,32}, \\ C^{\mathsf{FH}}_a &= C^{\mathsf{FH}}_{3,11} = C^{\mathsf{FH}}_{3,22}, \\ C^{\mathsf{FH}}_b &= C^{\mathsf{FH}}_{3,33}. \end{aligned} \tag{3.37}$$

The Raman scattering intensity can now be written as:

$$I_N(\omega) = \left(\frac{\omega_{\mathsf{s}}}{c}\right)^4 VL \left|\vec{e}^{\,\mathsf{S}} \cdot \tilde{R}_N \cdot \vec{e}^{\,\mathsf{L}}\right|^2 \left|\langle 1 + n_\omega| \, Q_N \, |n_\omega\rangle\right|^2. \tag{3.38}$$

The index N refers to the ordinary transverse phonon ($N = \mathsf{To}$), extraordinary transverse phonon ($N = \mathsf{Te}$), and extraordinary longitudinal phonon ($N = \mathsf{Le}$), respectively. The three matrices $\tilde{R_N}$ are:

$$\tilde{R}_{\mathsf{To}} = C \cdot \begin{pmatrix} 0 & 0 & -\sin\varphi \\ 0 & 0 & \cos\varphi \\ -\sin\varphi & \cos\varphi & 0 \end{pmatrix}, \tag{3.39}$$

with

$$C(\omega) = c_{\mathsf{TO}} \cdot \left(1 + \frac{\omega^2_{\mathsf{TO,E1}} - \omega^2}{C^{\mathsf{FH}}_c \omega^2_{\mathsf{TO,E1}}}\right),$$

$$\tilde{R}_{\mathsf{Te}} = \begin{pmatrix} A\sin\theta & 0 & -C\cos\theta\cos\varphi \\ 0 & A\sin\theta & -C\cos\theta\sin\varphi \\ -C\cos\theta\cos\varphi & -C\cos\theta\sin\varphi & B\sin\theta \end{pmatrix}, \tag{3.40}$$

and

$$\tilde{R}_{\mathsf{Le}} = \begin{pmatrix} A\cos\theta & 0 & C\sin\theta\cos\varphi \\ 0 & A\cos\theta & C\sin\theta\sin\varphi \\ C\sin\theta\cos\varphi & C\sin\theta\sin\varphi & B\cos\theta \end{pmatrix}, \tag{3.41}$$

with

$$A(\omega) = a_{\mathsf{TO}} \cdot \left(1 + \frac{\omega^2_{\mathsf{TO,A1}} - \omega^2}{C^{\mathsf{FH}}_a \omega^2_{\mathsf{TO,A1}}}\right),$$

and

$$B(\omega) = b_{\mathsf{TO}} \cdot \left(1 + \frac{\omega_{\mathsf{TO,A1}}^2 - \omega^2}{C_b^{\mathsf{FH}} \omega_{\mathsf{TO,A1}}^2}\right).$$

In the limit of $\omega \to \omega_{\mathsf{TO}}$, the coefficients $A(\omega)$, $B(\omega)$, and $C(\omega)$ result in the Raman tensor elements a_{TO}, b_{TO}, and c_{TO}.

3.5 Selection rules

Equation (3.38) describes the Raman scattering intensity of phonons (180° backscattering, 90° scattering geometry or near-forward scattering) as well as phonon polaritons (near-forward scattering). The following discussion will mainly focus on phonons (large wavevectors).
In case of phonons (large wavevectors), the matrix elements in equation (3.38) are

$$|\langle 1 + n_\omega \,|Q_N|\, n_\omega \rangle|^2 = \frac{\hbar\,(1 + n_\omega)}{2V\omega}. \tag{3.42}$$

For angles between wavevector and optical axis in the range $\theta = 0° \ \ldots \ 90°$ the symmetry of the extraordinary TO and LO phonons is of mixed character (see figure 3.3). However, for the angles $\theta = 0°$ and $\theta = 90°$ the phonons can be assigned to the following symmetries: The ordinary TO phonons have symmetry E_1 with polarization in the (x, y) plane independent on the angle θ. The extraordinary TO phonons have symmetry E_1 for $\theta = 0°$ with polarization in the (x, y) plane and symmetry A_1 for $\theta = 90°$ with polarization in direction z. The Raman tensors are then

$$E_1(TO): \qquad -\tilde{R}_{\mathsf{To}}(\varphi = 90°) = -\tilde{R}_{\mathsf{Te}}(\theta = 0°, \varphi = 0°) = \frac{\partial \chi_{ij}}{\partial Q_x} = \begin{pmatrix} & & \\ & & c_{\mathsf{TO}} \\ & c_{\mathsf{TO}} & \end{pmatrix},$$

$$\tilde{R}_{\mathsf{To}}(\varphi = 0°) = -\tilde{R}_{\mathsf{Te}}(\theta = 0°, \varphi = 90°) = \frac{\partial \chi_{ij}}{\partial Q_y} = \begin{pmatrix} & & \\ & & c_{\mathsf{TO}} \\ c_{\mathsf{TO}} & & \end{pmatrix}$$

$$A_1(TO): \qquad \tilde{R}_{\mathsf{Te}}(\theta = 90°) = \frac{\partial \chi_{ij}}{\partial Q_z} = \begin{pmatrix} a_{\mathsf{TO}} & & \\ & a_{\mathsf{TO}} & \\ & & b_{\mathsf{TO}} \end{pmatrix}. \tag{3.43}$$

The extraordinary LO phonons have symmetry A_1 with polarization in direction z for $\theta = 0°$ and symmetry E_1 with polarization in the (x, y) plane for $\theta = 90°$. The Raman tensors are

$$E_1(LO): \qquad \tilde{R}_{\mathsf{Le}}(\theta = 90°, \varphi = 0°) = \begin{pmatrix} & & c_{\mathsf{LO}} \\ & & \\ c_{\mathsf{LO}} & & \end{pmatrix},$$

$$\tilde{R}_{\mathsf{Le}}(\theta = 90°, \varphi = 90°) = \begin{pmatrix} & & c_{\mathsf{LO}} \\ & c_{\mathsf{LO}} & \\ & & \end{pmatrix} \tag{3.44}$$

$$A_1(LO): \qquad \tilde{R}_{\mathsf{Le}}(\theta = 0°) = \begin{pmatrix} a_{\mathsf{LO}} & & \\ & a_{\mathsf{LO}} & \\ & & b_{\mathsf{LO}} \end{pmatrix}.$$

Due to the macroscopic electric field accompanying the LO phonons, their Raman tensor elements are different from the TO phonon ones. The tensor elements are related by

$$\begin{aligned} a_{\mathsf{LO}} &= a_{\mathsf{TO}} \left(1 + \frac{\omega^2_{\mathsf{TO,A1}} - \omega^2_{\mathsf{LO,A1}}}{C_a^{\mathsf{FH}} \cdot \omega^2_{\mathsf{TO,A1}}} \right) \\ b_{\mathsf{LO}} &= b_{\mathsf{TO}} \left(1 + \frac{\omega^2_{\mathsf{TO,A1}} - \omega^2_{\mathsf{LO,A1}}}{C_b^{\mathsf{FH}} \cdot \omega^2_{\mathsf{TO,A1}}} \right) \\ c_{\mathsf{LO}} &= c_{\mathsf{TO}} \left(1 + \frac{\omega^2_{\mathsf{TO,E1}} - \omega^2_{\mathsf{LO,E1}}}{C_c^{\mathsf{FH}} \cdot \omega^2_{\mathsf{TO,E1}}} \right). \end{aligned} \tag{3.45}$$

For completeness the Raman tensors for the nonpolar phonons with E_2 symmetry are presented:

$$E_2: \quad \tilde{R}^{(1)}_{E_2} = \begin{pmatrix} & -d & \\ -d & & \\ & & \end{pmatrix}, \quad \tilde{R}^{(2)}_{E_2} = \begin{pmatrix} d & & \\ & -d & \\ & & \end{pmatrix}. \tag{3.46}$$

In order to determine the scattering efficiency of this twofold degenerated phonon mode the contributions of both Raman tensors given in equation (3.46) have to be added:

$$\left| \vec{e}^{\,\mathsf{S}} \cdot \tilde{R}_{E_2} \cdot \vec{e}^{\,\mathsf{L}} \right|^2 = \left| \vec{e}^{\,\mathsf{S}} \cdot \tilde{R}^{(1)}_{E_2} \cdot \vec{e}^{\,\mathsf{L}} \right|^2 + \left| \vec{e}^{\,\mathsf{S}} \cdot \tilde{R}^{(2)}_{E_2} \cdot \vec{e}^{\,\mathsf{L}} \right|^2. \tag{3.47}$$

The scattering intensity of the E_2 phonon does not depend on the phonon wavevector. Therefore, and due to its strong intensity it is suitable as reference phonon for normalization of the Raman spectra. The calculation of the Raman scattering intensity according to equation (3.38) with the Raman tensors defined in equations (3.39)-(3.41) requires as input data the directions of the polarization vectors and the phonon

wavevector. As mentioned in section 3.4, the direction of the phonon wavevector $\vec{k}_{\mathrm{Ph}}$ can be described by the angle θ between $\vec{k}_{\mathrm{Ph}}$ and the z axis and the angle φ between the orthogonal projection of $\vec{k}_{\mathrm{Ph}}$ on the (x, y) plane and the x axis.

Table 3.1 shows the scattering configurations used in this work allowing to measure the Raman intensity of all observable optical phonons of wurtzite-type GaN. The scattering configurations are given with respect to the Porto notation [83]. $x(zx)y$, for instance, means (from left to right) propagation of the exciting laser light parallel to the x axis of the crystal, z and x refer to the direction of the polarization vectors of incident and scattered light, respectively, and y indicates the direction of the wavevector of the scattered light.

Tab. 3.1: Allowed Raman tensor elements for different scattering configurations which are given with respect to the Porto notation. The angle θ refers to the included angle between phonon wavevector $\vec{k}_{\mathsf{Ph}}$ and z axis (c axis of the crystal).

Scattering configuration	Angle θ	Contribution of Raman tensor elements
		180° scattering geometry
$z(yy)\bar{z}$, $z(xx)\bar{z}$	$0°$	$a_{\mathsf{LO}}^2 + d^2$
$z(yx)\bar{z}$, $z(xy)\bar{z}$	$0°$	d^2
$x(yy)\bar{x}$	$90°$	$a_{\mathsf{TO}}^2 + d^2$
$x(yz)\bar{x}$, $x(zy)\bar{x}$	$90°$	c_{TO}^2
$x(zz)\bar{x}$	$90°$	b_{TO}^2
$x(uu)\bar{x}$	$90°$	$1/4(a_{\mathsf{TO}} + b_{\mathsf{TO}})^2 + c_{\mathsf{TO}}^2 + 1/4d^2$
$x(uv)\bar{x}$	$90°$	$1/4(a_{\mathsf{TO}} - b_{\mathsf{TO}})^2 + 1/4d^2$
		90° scattering geometry
$y(zz)x$	$90°$	b_{TO}^2
$y(zy)x$, $y(xz)x$	$90°$	$1/2c_{\mathsf{TO}}^2 + 1/2c_{\mathsf{LO}}^2$
$y(xy)x$	$90°$	d^2
$x(yy)z$	$45°$	$1/2a_{\mathsf{TO}}^2 + 1/2a_{\mathsf{LO}}^2 + d^2$
$x(yx)z$	$45°$	d^2
$x(zy)z$	$45°$	c_{TO}^2
$x(zx)z$	$45°$	$1/2c_{\mathsf{TO}}^2 + 1/2c_{\mathsf{LO}}^2$
		0° scattering geometry
$x(zz)x$	θ	$\cos^2\theta \cdot b_{\mathsf{LO}}^2 + \sin^2\theta \cdot b_{\mathsf{TO}}^2$
$x(zy)x$, $x(yz)x$	θ	c_{TO}^2
$x(yy)x$	θ	$\cos^2\theta \cdot a_{\mathsf{LO}}^2 + \sin^2\theta \cdot a_{\mathsf{TO}}^2 + d^2$
$x(uz)x$, $x(zu)x$	θ	$1/2\cos^2\theta \cdot b_{\mathsf{LO}}^2 + 1/2\sin^2\theta \cdot b_{\mathsf{TO}}^2 + 1/2c_{\mathsf{TO}}^2$
$x(uy)x$, $x(yu)x$	θ	$1/2\cos^2\theta \cdot a_{\mathsf{LO}}^2 + 1/2\sin^2\theta \cdot a_{\mathsf{TO}}^2 + 1/2c_{\mathsf{TO}}^2 + 1/2d^2$
$x(uu)x$	θ	$1/4\cos^2\theta \cdot (a_{\mathsf{LO}} + b_{\mathsf{LO}})^2 + 1/4\sin^2\theta \cdot (a_{\mathsf{TO}} + b_{\mathsf{TO}})^2 + c_{\mathsf{TO}}^2 + 1/4d^2$
$x(uv)x$	θ	$1/4\cos^2\theta \cdot (a_{\mathsf{LO}} - b_{\mathsf{LO}})^2 + 1/4\sin^2\theta \cdot (a_{\mathsf{TO}} - b_{\mathsf{TO}})^2 + 1/4d^2$

x: $[100]$, y: $[010]$, z: $[001]$, u: $[011]$, v: $[01\bar{1}]$

4 Influence of mechanical strain on Raman modes

Owing to the influence of strain on the phonon frequencies Raman spectroscopy is used for the investigation of strain with high spatial resolution. First, the effect of strain on the frequency shift of Raman scattered light in case of wz-GaN is explained in the framework of continuum mechanics. The experimental setup required for performing confocal micro-Raman measurements in order to analyze residual stress, for instance, is given in detail. Finally, results of a residual stress analysis will be presented.

4.1 Linear elasticity theory

The growth of GaN on foreign substrates typically leads to built-in strain in heteroepitaxial layers due to the lattice mismatch and the differences in thermal expansion coefficients between GaN and the substrate.

The c plane GaN layers grown on sapphire are expected to experience biaxial strain in the basal plane along the two main in-plane directions. Since these directions are parallel to the crystal principal axes, the shear stress components can be assumed to be zero. In the limit of linear elasticity theory, Hookes law (equation (2.3)) gives:

$$\begin{pmatrix} \sigma_1 \\ \sigma_2 \\ \sigma_3 \\ 0 \\ 0 \\ 0 \end{pmatrix} = \begin{pmatrix} C_{11}\varepsilon_1 + C_{12}\varepsilon_2 + C_{13}\varepsilon_3 \\ C_{12}\varepsilon_1 + C_{11}\varepsilon_2 + C_{13}\varepsilon_3 \\ C_{13}\varepsilon_1 + C_{13}\varepsilon_2 + C_{33}\varepsilon_3 \\ C_{44}\varepsilon_4 \\ C_{44}\varepsilon_5 \\ C_{66}\varepsilon_6 \end{pmatrix}. \tag{4.1}$$

As can be seen from equation (4.1), the corresponding shear strain components ε_4, ε_5, and ε_6 yield zero as well. The stress component σ_3 along the growth direction parallel to the c axis vanishes because the surface is free to expand or contract. From equation (4.1) it follows that the strain along the growth direction can be expressed by the two in-plane strain components:

$$\varepsilon_3 = -\frac{C_{13}}{C_{33}}(\varepsilon_1 + \varepsilon_2) \qquad \text{or} \qquad \varepsilon_{zz} = -\frac{C_{13}}{C_{33}}(\varepsilon_{xx} + \varepsilon_{yy}). \tag{4.2}$$

For compressive strain in the basal plane the strain in the growth direction will be tensile. Assuming isotropic biaxial in-plane strain ($\varepsilon_1 = \varepsilon_2$) equation (4.2) reads:

$$\varepsilon_3 = -\frac{2C_{13}}{C_{33}}\varepsilon_1 \qquad \text{or} \qquad \varepsilon_{zz} = -\frac{2C_{13}}{C_{33}}\varepsilon_{xx}, \tag{4.3}$$

where the term $2C_{13}/C_{33}$ denotes the biaxial Poisson ratio R^{biax} (see table 4.2). Inserting equation (4.3) in equation (4.1) the in-plane stress components can be expressed:

$$\begin{aligned} \sigma_1 = \sigma_2 &= (C_{11} + C_{12} - \frac{2C_{13}^2}{C_{33}})\varepsilon_1 \qquad \text{or} \\ \sigma_{xx} = \sigma_{yy} &= (C_{11} + C_{12} - \frac{2C_{13}^2}{C_{33}})\varepsilon_{xx}. \end{aligned} \tag{4.4}$$

The term $[C_{11} + C_{12} - (2C_{13}^2/C_{33})]$ refers to the biaxial modulus Y^{biax} (see table 4.2). The resulting phonon frequencies of a strained wurtzite crystal are shifted or split with respect to the strain-free values ω_0 which is shown schematically in figure 4.1. In the linear strain approximation the relation between these relative shifts or splittings of the Raman active phonon modes and the strain components was described by Briggs *et al.*[84]:

$$\Delta\omega_{\text{A1}} = a_{\text{A1}}(\varepsilon_{xx} + \varepsilon_{yy}) + b_{\text{A1}}\varepsilon_{zz}, \tag{4.5}$$

$$\Delta\omega_{\text{E1}} = a_{\text{E1}}(\varepsilon_{xx} + \varepsilon_{yy}) + b_{\text{E1}}\varepsilon_{zz} \pm c_{\text{E1}}\left[(\varepsilon_{xx} - \varepsilon_{yy})^2 + 4\varepsilon_{xy}^2\right]^{1/2}, \tag{4.6}$$

$$\Delta\omega_{\text{E2}} = a_{\text{E2}}(\varepsilon_{xx} + \varepsilon_{yy}) + b_{\text{E2}}\varepsilon_{zz} \pm c_{\text{E2}}\left[(\varepsilon_{xx} - \varepsilon_{yy})^2 + 4\varepsilon_{xy}^2\right]^{1/2}. \tag{4.7}$$

The degenerated modes E_1 and E_2 experience a splitting in case of (i) non-isotropic biaxial in-plane strain (i.e. $\varepsilon_{xx} \neq \varepsilon_{yy}$) and/or (ii) a non-zero shear strain component ε_{xy}. The coefficients a, b, and c refer to the corresponding phonon deformation potentials. Reports on experimental [54, 85–88] as well as theoretical determinations [89, 90] of the parameters a and b are available in literature. However, depending on the applied set of elastic constants the experimentally determined values of a and b differ as shown in table 4.1 in case of the phonon deformation potentials of the $E_{2,\text{high}}$ phonon mode in wz-GaN.

Neglecting phonon splitting[1] equations (4.5)-(4.7) can be rewritten by inserting equations (4.3) and (4.4):

$$\begin{aligned} \Delta\omega_{\text{Ph}} = \omega_{\text{Ph}} - \omega_0 &= 2a_{\text{Ph}}\varepsilon_{xx} + b_{\text{Ph}}\left(-\frac{2C_{13}}{C_{33}}\right)\varepsilon_{xx} \\ &= \left(\frac{2a_{\text{Ph}}C_{33} - 2b_{\text{Ph}}C_{13}}{C_{33}(C_{11} + C_{12}) - 2C_{13}^2}\right)\sigma_{xx} \\ &= K_{\text{Ph}}^{\text{biax}}\sigma_{xx}, \end{aligned} \tag{4.8}$$

where the index 'Ph' refers to the phonon symmetry[2] and $K_{\text{Ph}}^{\text{biax}}$ denotes the stress coefficient assuming biaxial stress in the c plane.

[1] In case of isotropic biaxial in-plane strain and shear strain components are zero.

[2] i.e. A_1, E_1 or E_2

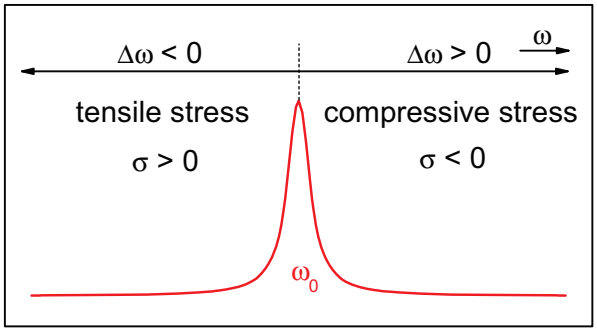

Fig. 4.1: Principle of stress measurement by Raman spectroscopy. The observed phonon frequencies of a strained crystal are shifted with respect to the strain-free values ω_0.

Typically, the relative shift of the $E_{2,high}$ Raman mode is chosen for the residual stress analysis in wz-GaN [7, 9, 17–19]. Inserting the set of elastic constants reported by Wright *et al.*[43] (see table 2.1), one yields the biaxial stress coefficient $K^{biax}_{E2,high}$ in dependence on reported phonon deformation potentials of this Raman active mode (table 4.1). In this work, the biaxial stress coefficient according to Davydov *et al.*[86] is adopted.

Tab. 4.1: Phonon deformation potentials of the $E_{2,high}$ Raman mode of wz-GaN at 300 K and the corresponding biaxial stress coefficient $K^{biax}_{E2,high}$ taking the set of elastic constants by Wright *et al.*[43].

$a_{E2,high}$ (cm^{-1})	$b_{E2,high}$ (cm^{-1})	$K^{biax}_{E2,high}$ (cm^{-1} GPa^{-1})	Reference
-742	-715	-2.49	calc. [90]
-850	-920	-2.74	exp. [86]
-850	-963	-2.69	exp. [87]
-911	-852	-3.09	exp. [88]

4.2 Residual stress analysis

In order to optimize the growth conditions and to understand relaxation mechanisms of thermal strain a series of GaN layers deposited on sapphire substrates differing in film thickness was investigated. As a non-destructive tool for characterization micro-Raman spectroscopy was used in this work. This allows to monitor changes in residual stresses within the GaN films with a high lateral and depth spatial resolution. Moreover, photoluminescence measurements and finite element simulations were applied to complement the Raman results.

4.2.1 Experimental details

Growth of the samples

The epitaxial (0001) GaN layers investigated in the present study were grown by hydride vapor phase epitaxy (HVPE) in a commercial single-wafer Aixtron system with a horizontal design. The HVPE growth was performed on GaN templates with a diameter of 2 inch and a layer thickness of 3 μm grown in an Aixtron 200/4 RF-S MOVPE system. For defect reduction a SiN-interlayer was included [91]. The (0001)-oriented sapphire substrates had a miscut of 0.3° towards the a plane and a thickness of 430 μm. As the growth was carried out in the group of Prof. Dr. Ferdinand Scholz (Ulm University), details of the growth conditions are described by Brückner *et al.*[92]. The total film thickness varied from 20 μm to 300 μm and no separation during cooldown from the growth temperature of 1050°C to room temperature occurred.

Curvature measurement

After the growth, the 2″ wafers were cut into fragments comparable in size and shape as well as the wafer position they were taken from. One piece of every GaN layer thickness, respectively, was used for the investigations described in the following. The curvature values of the wafer fragments were obtained by means of the profile method and were conducted by Dr. Frank Habel (Freiberger Compound Materials GmbH). The diamond tip of a MarSurf perthometer (Mahr GmbH) scanned the surface with constant velocity. The deflexion of the tip was detected and resulted in the surface profile. In order to separate any signal generated by variation of the layer thickness as well as inhomogeneities in the surface morphology, the measurements were carried out on the backside of the sapphire substrate. Assuming spherical bending the obtained surface profiles were exploited to determine the radii of curvature.

FEM simulation

A numerical model of the bilayer system was developed by Dr. Martin Abendroth (TU Bergakademie Freiberg, Institute of Mechanics and Fluid Dynamics) to analyze the elastic strains and stresses across the substrate and the GaN film using the finite element method (FEM). The geometry of the model is an axisymmetric cross section of a circular wafer with a radius of 5 mm. This radius approximately corresponds to the size of the fragments where curvature, Raman, and photoluminescence measurements were performed. The nodes at the outer radius are not constrained which agrees with free edges of the fragments. The ratio of total thickness and radius for the considered specimens ranging between 0.09 and 0.146 raised doubts about the applicability of classical plate theory. Therefore, axisymmetric plate elements in the numerical model were discarded. Instead, axisymmetric 8-node continuum elements

were chosen to simulate all relevant deformation mechanisms using the Abaqus finite element code [93]. Non-linear geometrical effects were taken into account as well.

Raman setup

Room temperature Raman measurements on the wafer fragments were performed in the center region of each sample in backscattering geometry using a Labram HR 800 Horiba Jobin Yvon (Villeneuve d'Ascq, France) spectrometer with a thermoelectrically cooled charge-coupled device (CCD) detector. The spectral calibration was realized employing a mercury vapor lamp. For excitation the 532 nm (2.33 eV) line of a frequency-doubled Nd:YAG laser was used. By passing the laser through a 100x Olympus microscope objective, the linearly polarized laser beam was focused on the surface of the GaN films. The scattered light was collected by the same objective and contained both the $z(yx)\bar{z}$ (crossed polarization) and $z(yy)\bar{z}$ (parallel polarization) configurations with the z direction oriented parallel to the c axis of the samples.

As GaN is transparent in the visible spectral range, it is possible to obtain depth dependent information with a lateral resolution of about 1 μm by using the confocal technique [94]. Figure 4.2(a) shows schematically the described optical path and illustrates the principle of the confocal microscopy. Moving the focal plane indicated by the horizontal solid line allows scanning the GaN layer. The observable Raman modes were fitted in order to obtain the spectral position as function of the distance from the GaN/sapphire interface. By varying the diameter of the confocal hole the depth resolution was adjusted to be 3 μm (up to a GaN layer thickness of 100 μm) and 25 μm (for layer thicknesses greater than 100 μm).

4.2.2 Results and discussion

Wafer curvature model

The curvature of the investigated GaN/sapphire wafer fragments was determined mechanically by the profile method. The fragments of the 2″ wafers comparable in size and shape were assumed to be spherically bended. With this assumption, the obtained surface profiles were exploited to determine the radii of curvature. The observation of a convex curvature confirms that GaN films epitaxially grown on sapphire are under biaxial compression in the plane perpendicular to the c axis at room temperature because GaN has a smaller thermal expansion coefficient than sapphire [45]. The experimental curvature values of the wafer fragments as a function of the GaN layer thickness are plotted as circles in figure 4.3. In order to interpret these curvature data an appropriate wafer bending model is needed. Although, several models on wafer bending have been presented in literature [96–98], the approach established by Etzkorn and Clarke [11] was chosen due to its invariance against

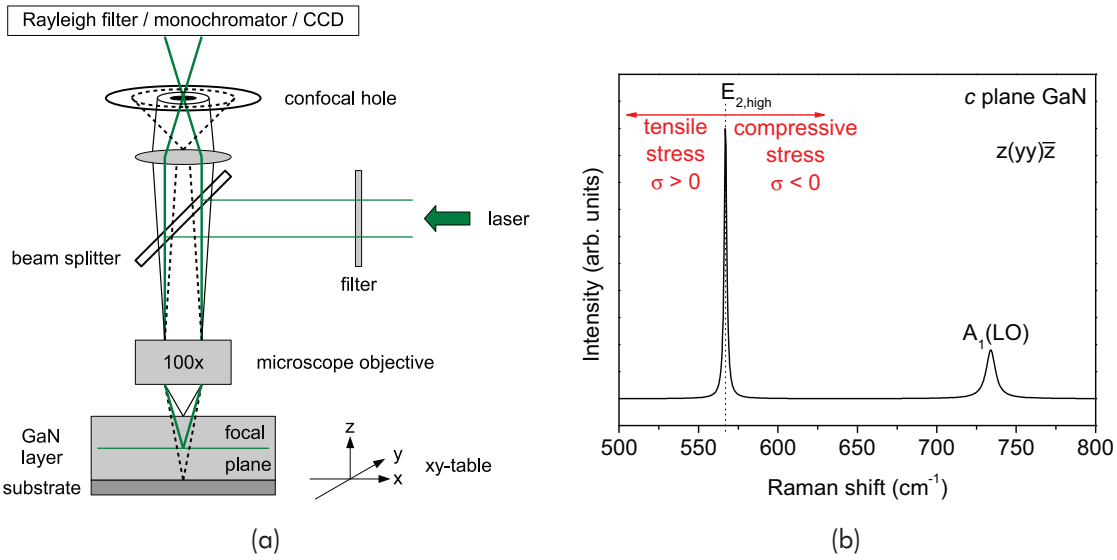

Fig. 4.2: (a) The optical path of the Raman backscattering setup illustrates the principle of the confocal technique. Thus, depth dependent information as function of the distance from the GaN/sapphire interface is obtained. (b) According to the selection rules for GaN the figure shows a typical Raman spectrum recorded in backscattering geometry. The $E_{2,high}$ mode is affected by strain resulting in a shift of the phonon peak position as indicated by the arrows. Reprinted figure with permission from [95]. Copyright 2013 IOP Publishing Ltd.

permutation of the layer and the substrate [12]. It should be noticed that the Etzkorn/Clarke model assumes elastically isotropic materials, spherical bending, a biaxial stress state, and only thermal expansion mismatch strain. According to equation (2.6) the strain perpendicular to the c axis is expressed as

$$\varepsilon_{th} = \int_{T_G}^{T_{RT}} \left(\alpha_a^{substrate}(T) - \alpha_a^{film}(T)\right) \mathrm{dT}, \tag{4.9}$$

where $T_G = 1050°\mathrm{C}$ is the growth temperature, $T_{RT} = 25°\mathrm{C}$ is the room temperature, and $\alpha_a^{substrate}(T)$ and $\alpha_a^{film}(T)$ are the respective temperature dependent thermal expansion coefficients in the a direction. The parameter set (table 4.2) required for the simulations by means of this mechanical bending model was obtained using the elastic stiffness constants C_{ij} of GaN and sapphire reported by Wright *et al.*[43] and Wachtman *et al.*[99], respectively. As the relation $C_{11}+C_{12} \approx C_{13}+C_{33}$ which is identically fulfilled by cubic crystals and elastically isotropic materials [61] holds for GaN, the respective model assumption is suitable as well. Taking the thermal expansion coefficients of sapphire [12] and GaN [42], and neglecting their temperature dependence, the theoretical thermally induced mismatch in-plane strain ε_{th} was calculated. Equation (4.9) results in $\varepsilon_{th} = -1.74 \times 10^{-3}$ at the GaN/sapphire interface. This value was used in the Etzkorn/Clarke model resulting in the simulated wafer curvature as a function of the GaN layer thickness represented by the solid line in figure 4.3. The comparison with the experimentally determined curvature gives a good agreement,

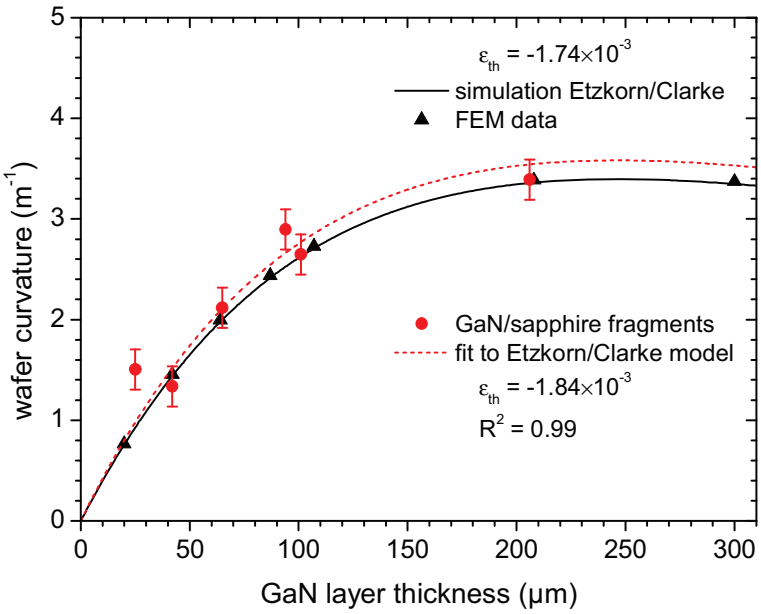

Fig. 4.3: The convex radii of curvature of the wafer fragments (circles) as function of the GaN layer thickness were fitted to the Etzkorn/Clarke bending model [11]. The fit is represented by the dashed line. Curvature values derived from FEM are depicted by triangles whereas the solid line corresponds to the simulation by the Etzkorn/Clarke model. Both numerical calculations were performed assuming only thermal mismatch strain $\varepsilon_{th} = -1.74 \times 10^{-3}$. Reprinted figure with permission from [95]. Copyright 2013 IOP Publishing Ltd.

as can be seen in figure 4.3. Differences could be explained by (i) neglecting the temperature dependence of the thermal expansion coefficients, and (ii) a tensile in-plane strain, already being present during growth [13] which is not considered in this study.

Tab. 4.2: Biaxial modulus Y^{biax}, biaxial Poisson ratio R^{biax}, and thermal expansion coefficient α_a of wz-GaN and sapphire.

	wz-GaN		sapphire	
	(biaxial in c plane)	Reference	(biaxial in c plane)	Reference
Y^{biax}	450 GPa	[43]	612 GPa	[99]
R^{biax}	0.509	[43]	0.445	[99]
α_a	6.2×10^{-6} K^{-1}	[42]	7.9×10^{-6} K^{-1}	[12]

Further, the applicability of the Etzkorn/Clarke model was examined. Thereto, a finite element model of the bilayer system was developed taking non-linear geometrical effects except buckling into account. In order to analyze elastic strains and stresses across the sapphire substrate and the GaN film an axisymmetric cross section of a circular wafer (radius of 5 mm) as well as 8-node axisymmetric continuum elements were used by the FEM approach. The simulation of the circular cross section in

case of an axisymmetrically bent wafer revealed non-zero off-diagonal strain tensor elements. These shear strain components are largest at the outer radius of the model where the nodes were not constrained. This assumption agrees with free edges of the samples. However, the shear strain relaxes rapidly from the outer edge within a horizontal range of approximately the total thickness of the bilayer system. Thus, in the wafer center where FEM data were deduced the off-diagonal strain tensor elements are negligible with respect to the diagonal ones which makes biaxial stress conditions given by $\varepsilon_{xx} = \varepsilon_{yy} \neq \varepsilon_{zz}$ suitable.

The thermal mismatch strain inducing the curvature of the bilayer finite element model can be implemented (i) by setting the thermal expansion coefficients for the two materials and simulating the thermal contractions of the cooling process numerically or (ii) by assuming initial stress in the layers. The values for the initial stress can be determined using the formulas given by Etzkorn and Clarke [11].

Both options were employed and compared with each other and the Etzkorn/Clarke model, respectively. The marginal difference of both curvature curves calculated by FEM (not shown in figure 4.3) is due to the thermal contraction of the composite which is considered in the first case only. The wafer curvature of discrete GaN layer thicknesses derived from FEM simulations was plotted in figure 4.3 assuming the theoretical thermally induced mismatch strain ε_{th}. The computed curvature values of the fragments are about 2% higher than the theoretical values by Etzkorn/Clarke.

In agreement with Freund [100] these discrepancies between the Etzkorn/Clarke model and the FEM calculations are negligible. In his work, Freund focused the discussion on the limit of the linear range considering the relationship between mismatch strain and substrate curvature. For this purpose, two dimensionless parameters - normalized curvature K and normalized mismatch strain S - were introduced. The magnitude of the normalized mismatch strain takes the form

$$S = \frac{3R^2 \varepsilon_{th} h_f Y_f^{\text{biax}}}{2 h_s^3 Y_s^{\text{biax}}} \tag{4.10}$$

where R is the substrate radius, the product $\varepsilon_{th} h_f Y_f^{\text{biax}}$ represents the membrane force in the film, h_s and Y_s^{biax} denote thickness and biaxial modulus of the substrate, respectively.

Assuming spatially uniform curvature, the relation between normalized mismatch strain S and normalized curvature K takes the form

$$S = K \left[1 + (1 - \nu_s) K^2\right] \tag{4.11}$$

in the case $h_f \ll h_s$, where ν_s is the Poisson ratio of the substrate being 0.295 for sapphire [99]. The graph of equation (4.11) is shown as solid line in figure 4.4(a) along with the linear relationship between normalized curvature K and normalized mismatch strain S depicted by the dashed line. In the case of system parameter sets

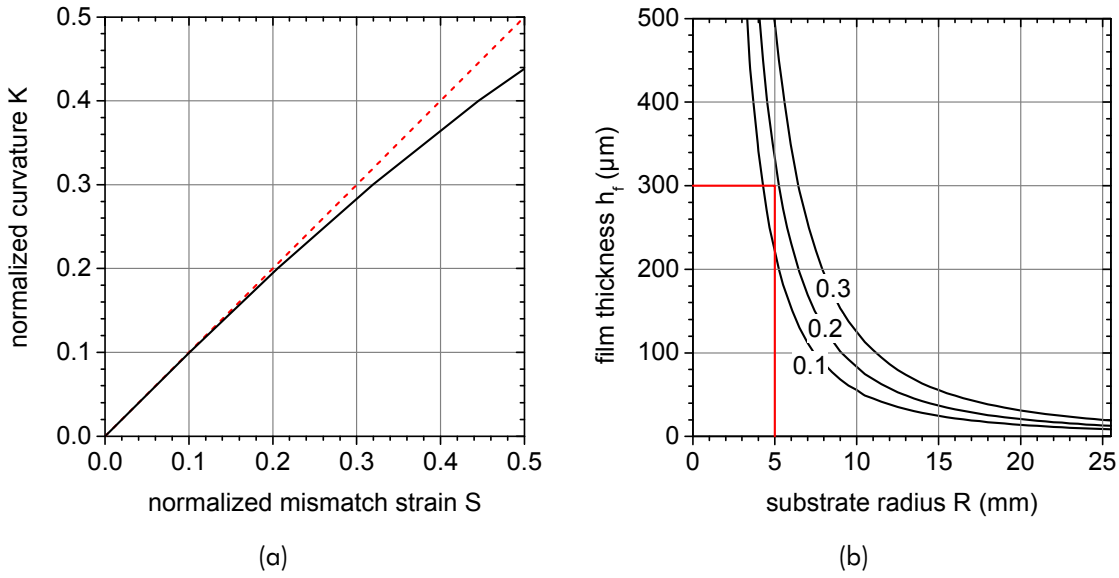

Fig. 4.4: (a) Relationship between normalized curvature K and normalized mismatch strain S implied by equation (4.11) with $\nu_s = 0.295$ for sapphire (solid line). The dashed line represents the linear relationship implied by the Etzkorn/Clarke model. (b) Contour plot showing levels of the normalized mismatch strain S as function of the substrate radius R and the film thickness h_f implied by equation (4.10) with $\varepsilon_{th} = -1.74 \times 10^{-3}$ and $h_s = 430$ μm. The red lines mark the maximum film thickness and substrate radius of the investigated samples, respectively. Reprinted figure with permission from [95]. Copyright 2013 IOP Publishing Ltd.

according to equation (4.10) for which $S > 0.3$, non-linear geometrical effects have to be taken into account. Further, in order to estimate such sets of system parameters, figure 4.4(b) illustrates the contour plot showing levels of the normalized mismatch strain S as function of the substrate radius R and the film thickness h_f with a substrate thickness $h_s = 430$ μm and a theoretical thermal mismatch strain $\varepsilon_{th} = -1.74 \times 10^{-3}$ (see above). The red lines in figure 4.4(b) mark the maximum GaN layer thickness and fragment radius of the investigated samples. As for the dimensions of each specimen analyzed $S < 0.3$ holds, the influence of non-linear geometrical effects on the results can be neglected. Thus, the use of the Etzkorn/Clarke model as approach is justified. However, the advantage of the numerical finite element model taking non-linear geometrical effects into account becomes relevant when considering larger diameter and/or thicker samples.

Finally, the curvature values of the wafer fragments determined by the profile method were fitted to the Etzkorn/Clarke bending model leading to the parameter $\varepsilon_{th} = -1.84 \times 10^{-3}$ which is a measure of the residual thermal strain with a correlation coefficient $R = 0.99$ (six samples). Figure 4.3 shows the fit as function of the GaN layer thickness depicted by the dashed line.

Raman scattering measurements

Confocal Raman measurements were carried out on three different points in the center region at each GaN/sapphire fragment with the same depth resolution (3 μm). The laser focus was adjusted 5 μm below the GaN surface. The scattered light was recorded in backscattering geometry (figure 4.2(a)) and contained both the $z(yx)\bar{z}$ and $z(yy)\bar{z}$ configurations. According to the selection rules discussed in section 3.5 three phonons ($E_{2,low}$, $E_{2,high}$, and A_1(LO)) are allowed. Figure 4.2(b) shows a typical Raman spectrum of c plane GaN recorded in backscattering $z(yy)\bar{z}$ configuration. Due to limitations of the Rayleigh filter the $E_{2,low}$ mode was not accessible.

All observable Raman modes are affected by strain [19, 62, 86, 90] resulting in shifts of the phonon peak positions as indicated by the arrows in figure 4.2(b). The position of the nonpolar $E_{2,high}$ mode was chosen for further investigations because it is the only phonon observable in the used configuration merely affected by strain. On the contrary, a coupling of the A_1(LO) phonon to free charge carriers might also cause a frequency shift and additionally a broadening of the LO phonon peak (see chapter 5). After background correction the $E_{2,high}$ Raman mode was fitted by a Lorentzian function (i) to detect its spectral position as precisely as possible within ± 0.03 cm^{-1} and (ii) to deduce the full width at half maximum (FWHM) of this phonon mode.

Figure 4.5(a) shows the mean peak position of the $E_{2,high}$ Raman mode as function of the GaN layer thickness. The error bars refer to the standard deviations giving a measure for the in-plane strain variation. The observed peak positions of the $E_{2,high}$ mode are shifted to higher wavenumbers compared to the reference value of unstrained bulk GaN ($E_{2,high}$: 567.6 cm^{-1}) reported by Davydov *et al.*[65] which indicates compressive stress as discussed in section 4.1. The difference in the thermal expansion coefficients between GaN and sapphire can explain the compressively stressed GaN layer at room temperature. With an increasing GaN layer thickness, the peak position shifts to lower ω. These results are in accordance with findings reported by Hiramatsu *et al.*[52] investigating the c lattice parameter as function of the GaN layer thickness by means of XRD measurements. They observed a decrease of the c lattice parameter with increasing GaN film thickness indicating a relaxation of the compressive stress in the c plane. Moreover, an increase of the $E_{2,high}$ FWHM values with increasing GaN layer thickness was found as depicted in figure 4.5(b). It should be noted that the relevant measurements were conducted adjusting the laser focus 5 μm below the GaN surface of each sample. To assess the crystalline quality of GaN layers the FWHM is an important criterion as native defects and impurities restrict the phonon propagation [101]. A broadening of the Raman mode FWHM occurs due to the uncertainty of the transferred phonon wavevector in the Raman scattering process. Thus, the observed increase of the FWHM with increasing GaN

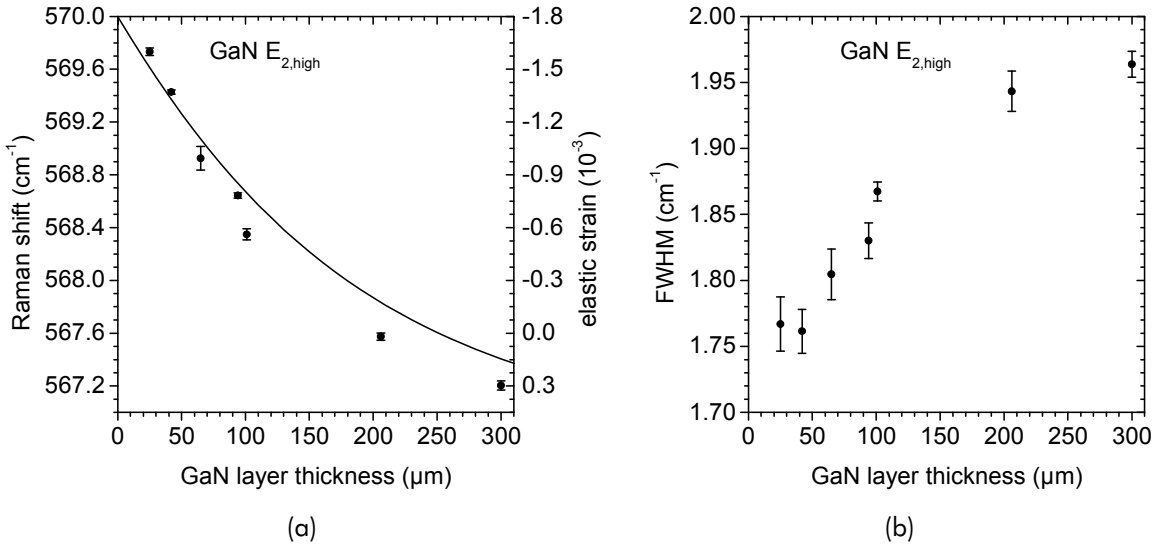

Fig. 4.5: (a) The mean $E_{2,high}$ peak position of three measurements 5 μm beneath the sample surface from different spots (circles) as function of the GaN layer thickness. The solid line represents the simulation derived from the Etzkorn/Clarke model using the fit parameter $\varepsilon_{th} = -1.84 \times 10^{-3}$ obtained in the previous subsection. (b) The mean $E_{2,high}$ full width at half maximum (FWHM) of three measurements 5 μm beneath the sample surface as function of the GaN layer thickness. The increase of the FWHM with increasing GaN film thickness assumably correlates to the dislocation developing as an additional strain relaxation mechanism. Reprinted figure with permission from [95]. Copyright 2013 IOP Publishing Ltd.

layer thickness can be correlated directly to a dislocation developing which is an additional mechanism of strain relaxation.

Taking the fit parameter $\varepsilon_{th} = -1.84 \times 10^{-3}$ previously obtained, the $E_{2,high}$ peak position 5 μm beneath the GaN surface was calculated by means of the Etzkorn/Clarke model in dependence on the GaN layer thickness. It should be reemphasized that the Etzkorn/Clarke model assumes a biaxial stress state. This seems most likely as the Raman measuring points were in the center region of the GaN/ sapphire fragments. With respect to the results of the axisymmetric FEM model discussed above shear strain/stress components can be neglected. For the determination of the $E_{2,high}$ peak position equation (4.8) and the following parameters were used: ω_0 = 567.6 cm^{-1} ($E_{2,high}$ Raman frequency of unstrained bulk GaN [65]) and $K^{biax}_{E2,high}$ = -2.7 cm^{-1}GPa^{-1} ($E_{2,high}$ stress coefficient assuming biaxial stress in the c plane reported by Davydov *et al.*[86]). It is seen from figure 4.5(a) that the simulation which is based merely on wafer bending and represented by the solid line agrees well with the Raman results. Nevertheless, the deviation of the experimental findings from the numerical calculation in case of thicker samples should be ascribed to an additional strain relaxation mechanism like dislocation developing as supported by the FWHM analysis. Furthermore, the residual stress distribution within each GaN film has been studied applying the confocal technique. Scanning the GaN layer by varying the focal plane

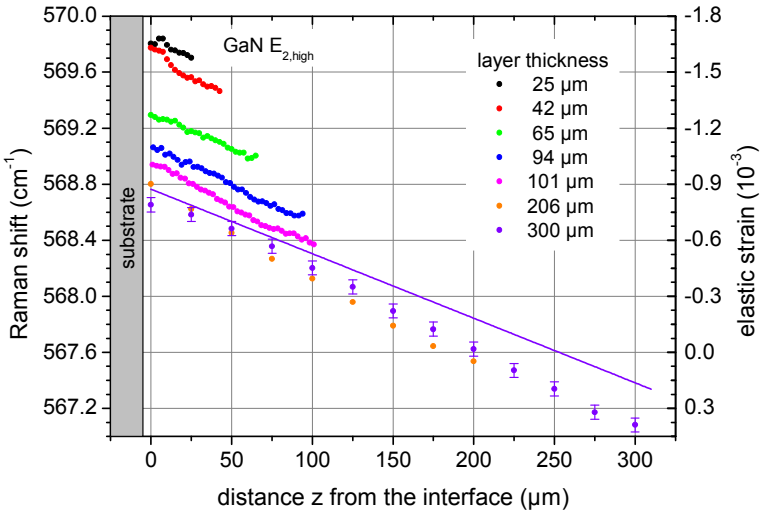

Fig. 4.6: The peak position of the $E_{2,high}$ Raman mode as function of the distance z from the interface according to figure 4.2(a). The solid line represents the simulation for the 300 μm thick GaN sample derived from the Etzkorn/Clarke model using the fit parameter $\varepsilon_{th} = -1.84 \times 10^{-3}$ (see previous subsection). The calculation predicts a neutral axis being within the 300 μm thick GaN film. Reprinted figure with permission from [95]. Copyright 2013 IOP Publishing Ltd.

from the top to the GaN/sapphire interface as illustrated in figure 4.2(a) and analyzing the $E_{2,high}$ Raman mode, allowed changes in residual stress to be monitored non-destructively. The peak position of the $E_{2,high}$ phonon as function of the z-coordinate starting at the interface is shown in figure 4.6. A shift to higher wavenumbers within all layers compared to the reference value of unstrained, bulk GaN was found. In principle, this indicates compressive stress which is expected for GaN layers epitaxially grown on sapphire substrates due to the thermal expansion mismatch. The total strain energy of heteroepitaxial systems containing strained layers can be reduced by bending. As convex radii of curvature were determined on the investigated wafer fragments, a stress relaxation should occur. The decreasing wavenumber of the $E_{2,high}$ spectral position within one GaN layer from the GaN/sapphire interface to the top confirms a stress relaxation from the interface to the top of the GaN layer. Moreover, the experimental results for the 300 μm thick GaN layer coincide quite well to the simulation derived from the Etzkorn/Clarke model using the fit parameter $\varepsilon_{th} = -1.84 \times 10^{-3}$ (solid line in figure 4.6). Therefore, one relaxation mechanism of thermally induced strain is wafer bending. In addition, the results show a decreasing compressive stress on the top of each layer with an increasing film thickness of GaN as predicted by the wafer bending model (see figure 4.5(a)). This observation can be explained by simple mechanics and is ascribed to the thickness ratio of film and substrate: The thicker the GaN layer the larger the curvature of the bilayer system (see figure 4.3).

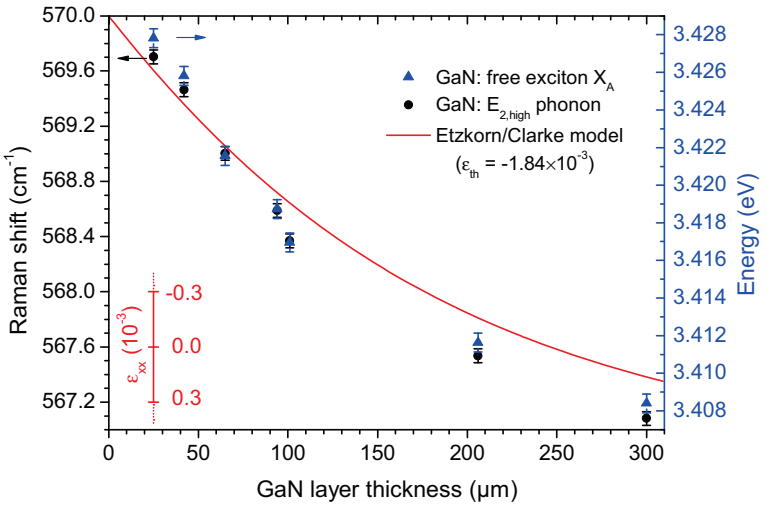

Fig. 4.7: Correlation of Raman data measured at the sample surface (circles) and PL results (triangles) as function of the GaN layer thickness. As the shift of the $E_{2,high}$ phonon mode and the A free exciton, respectively, depends linearly on strain, the scaled plot evidences the same origin of the observed effects. The solid line represents the simulation of the elastic in-plane strain ε_{xx} at the GaN surface derived from the Etzkorn/Clarke model. For this purpose, the previously obtained parameter ε_{th} by fitting the experimental curvature values to the Etzkorn/Clarke model was employed. The scale of the in-plane strain ε_{xx} refers to the reference $E_{2,high}$ phonon position of unstrained GaN (567.6 cm^{-1}). A difference in the Raman shift of +0.4 cm^{-1} (-0.4 cm^{-1}) corresponds to a compressive (tensile) strain of approximately 0.3×10^{-3}. Reprinted figure with permission from [95]. Copyright 2013 IOP Publishing Ltd.

When a critical radius of curvature is reached a neutral axis within the GaN layer and tensile stress in the topmost layer of the film can be observed. By means of the developed FEM bilayer model the elastic stresses across the GaN film for different layer thicknesses were simulated. In the case of a 300 μm thick GaN layer the numerical calculations as well as the simulation derived from the Etzkorn/Clarke model predict a neutral axis being within the GaN film. Assuming 567.6 cm^{-1} to be the strain-free $E_{2,high}$ Raman frequency, the existence of a neutral axis according to beam theory is experimentally evidenced for the 300 μm thick GaN layer at about 200 μm from the GaN/sapphire interface as can be seen in figure 4.6.

In addition to FEM simulations and Raman investigations, photoluminescence measurements on the wafer fragments have been performed. The photoluminescence (PL) measurements were carried out at room temperature using the 325 nm (3.82 eV) line of a cw Kimmon HeCd laser. At room temperature the optical transition $\Gamma_{9v} \rightarrow \Gamma_{7c}$ referred to as the A exciton transition (see figure 2.3(b)) is observable with the energy gap influenced by strain [10, 62, 63]. The strain dependence of the A free exciton transition energy E_A neglecting spin-orbit interaction is given by equation (2.7) (see section 2.4).

The experimentally determined energy positions of the A free exciton are presented in

figure 4.7 as function of the GaN layer thickness. From the PL results the GaN layers investigated are exposed to compressive stress as the above Raman measurements have already shown. As the shift of the $E_{2,high}$ Raman mode is also linearly connected with strain, both Raman and PL results measured at the sample surface are expected to correlate if the obtained shifts result from an effect of strain with the same origin. The scaled plot of PL and Raman data as function of the GaN layer thickness shows a good correlation as can be seen in figure 4.7. The solid line in figure 4.7 represents the simulation of the elastic in-plane strain ε_{xx} at the GaN surface derived from the Etzkorn/Clarke model. For this purpose, the parameter $\varepsilon_{th} = -1.84 \times 10^{-3}$ obtained previously by fitting the experimental curvature values to the respective mechanical wafer bending model was employed.

4.3 Conclusion

The effects of residual strain due to the difference in thermal expansion coefficients in GaN/sapphire heterostructures have been studied using confocal micro-Raman spectroscopy and photoluminescence measurements. The GaN layers deposited on sapphire substrates were found to be exposed to compressive stress. Confocal Raman investigations revealed that wafer bending is an effective relaxation mechanism of thermally induced stress. The wafer curvature of the specimens investigated was obtained by means of profilometry. The comparison of experimental radii of curvature with theoretical ones simulated by a mechanical wafer bending model as well as a numerical FEM model taking non-linear geometrical effects into account gives an excellent agreement.

The limitations of applicability of the Etzkorn/Clarke model describing the wafer curvature were discussed regarding sample dimensions such as GaN film thickness and substrate radius. Since the use of the Etzkorn/Clarke approach was justified by FEM simulations, the experimentally determined radii of curvature were fitted to this mechanical bending model. Using the fit parameter ε_{th}, the Etzkorn/Clarke model was exploited to simulate the $E_{2,high}$ Raman frequency in dependence on the GaN layer thickness. Deviations between these numerical calculations and the experimental results observed for thicker GaN layers give rise to additional relaxation mechanisms involved. Most likely, the dislocation developing plays an important role in the residual stress relaxation which is supported by the FWHM analysis of the $E_{2,high}$ Raman mode. Systematic research studies of residual stress are necessary to understand the stress relaxation phenomena involved.

5 Influence of free charge carriers on Raman modes

In polar semiconductors collective excitations of free charge carriers (plasmons) interact with longitudinal optical (LO) phonons via their associated macroscopic electric fields. This interaction results in two coupled modes appearing instead of a pure plasmon and a pure LO phonon. First, basic equations are introduced allowing to access the charge carrier concentration as well as the mobility by Raman scattering from measured frequencies, bandwidths, and intensities of coupled phonon plasmon modes. Afterwards, results of the Raman spectroscopic determination of carrier concentration and mobility on wz-GaN are presented and discussed.

5.1 Dielectric approach

As described in section 3.2 a uniaxial crystal is characterized by dielectric functions for the optically isotropic (x, y) plane $($see equations (3.7) and (3.17)$)$ and for the direction perpendicular to this plane which is referred to as the optical axis c $($see equations (3.8) and (3.20)$)$. In presence of free carriers and including damping, the dielectric function for the direction parallel to the optical axis c is written by (i) the phonon contribution given by equation (3.20) and (ii) the plasmon (electronic) term (see [28, 102], for instance):

$$\varepsilon_{\parallel}(\omega) = \varepsilon_{\infty\parallel}\left[1 + \frac{\omega_{\mathsf{L}\parallel}^2 - \omega_{\mathsf{T}\parallel}^2}{\omega_{\mathsf{T}\parallel}^2 - \omega^2 - \mathrm{i}\omega\Gamma_{\parallel}} - \frac{\omega_{\mathsf{P}}^2}{\omega^2 + \mathrm{i}\omega\gamma}\right], \tag{5.1}$$

where $\omega_{\mathsf{T}\parallel}$ and $\omega_{\mathsf{L}\parallel}$ denote the uncoupled frequencies of the transverse and longitudinal optical phonon polarized along the optical axis c, respectively, $\varepsilon_{\infty\parallel}$ refers to the high-frequency dielectric constant (see section 3.2), $\Gamma_{\parallel}$ is the phonon damping constant and can be interpreted macroscopically as full width at half maximum (FWHM) of the pure LO phonon peak at $\omega_{\mathsf{L}\parallel}$.
The plasma frequency ω_{P} is given by:

$$\omega_{\mathsf{P}} = \sqrt{\frac{e^2 n}{\varepsilon_0 \varepsilon_\infty m^*}}, \tag{5.2}$$

where e denotes the elementary charge, and n and m^* refer to the concentration and the effective mass of the free charge carriers. Barker *et al.*[103] demonstrated that the plasmon frequency in GaN is isotropic within the experimental resolution.
The plasmon damping γ is related to the charge carrier mobility μ and can be expressed as:

$$\gamma = \frac{e}{m^* \mu}. \tag{5.3}$$

Similarly, the dielectric function for the optical isotropic (x, y) plane can be treated. For further reading and details see [26, 27].

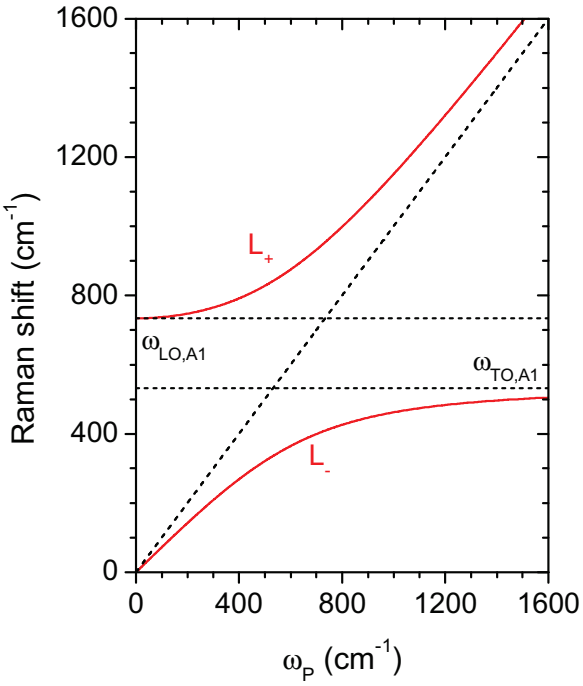

Fig. 5.1: Solutions of equation (5.4): dispersion of the L_+ and the L_- branches in wz-GaN (A_1 type) as a function of the plasma frequency ω_P.

The interaction of free charge carriers (plasmons) with longitudinal optical phonons via their associated macroscopic electric fields results in two coupled modes appearing instead of a pure plasmon and a pure LO phonon. The TO phonon is uneffected. Coupled LO phonon plasmon modes which have mixed plasmon phonon character were first proposed by Varga [104] and first observed by Mooradian and Wright [105] in GaAs and by Hon and Faust [106] in GaP. The lineshape and peak frequency of the two coupled modes change sensitively with the carrier concentration n and mobility μ. A crude estimation of the charge carrier concentration can be obtained using simple Drude theory. Neglecting the damping terms in equation (5.1) and solving the relation $\varepsilon_{\parallel}(\omega) = 0$, one obtains the coupled mode equation:

$$\omega_{\pm}^2 = \frac{1}{2}\left[\left(\omega_P^2 + \omega_{L\parallel}^2\right) \pm \sqrt{\left(\omega_P^2 - \omega_{L\parallel}^2\right)^2 + 4\omega_P^2\left(\omega_{L\parallel}^2 - \omega_{T\parallel}^2\right)}\right]. \tag{5.4}$$

The roots of equation (5.4) denote the frequencies ω_+ and ω_- of the resulting L_+ and L_- coupled modes, respectively. In figure 5.1 both, the L_+ and L_- branches are shown as function of the plasma frequency ω_P in case of A_1 symmetry. In the limit of $\omega_P \to 0$, i.e. carrier density $n \to 0$, the lower branch converges to zero and the upper to the frequency of the (pure) A_1(LO) phonon mode. With increasing ω_P the L_+ mode shifts to higher frequency. For large ω_P the L_- branch approaches the frequency of the transverse phonon TO(A_1).

For a more precise evaluation of the charge carrier concentration as well as the mobility, a lineshape fitting analysis based on a semiclassical approach taking the scattering mechanisms into consideration can be applied [28]. The Raman scattering by LO phonon plasmon modes is due to the following mechanisms:

A) modulation of the optical polarizability by atomic displacements (deformation potential scattering) and by the macroscopic longitudinal electric field (electro-optical scattering),

B) scattering due to charge density fluctuations of the free carriers.

As the Raman scattering of the coupled modes in wz-GaN is dominated by the first mechanism [34] the following discussion will be confined to this case. The Raman lineshape can then be described by:

$$I(\omega) = S\ A(\omega)\ \mathrm{Im}\left[-\frac{1}{\varepsilon(\omega)}\right], \tag{5.5}$$

where S is a constant factor and $A(\omega)$ is given by:

$$\begin{aligned} A(\omega) = 1 &+ C_\alpha^{\mathrm{FH}}\ \frac{2\omega_{\mathrm{TO},\alpha}^2}{\Delta}\left[\omega_{\mathrm{P}}^2\gamma\left(\omega_{\mathrm{TO},\alpha}^2 - \omega^2\right) - \omega^2\Gamma\left(\omega^2 + \gamma^2 - \omega_{\mathrm{P}}^2\right)\right] \\ &+ C_\alpha^{\mathrm{FH}2}\ \frac{\omega_{\mathrm{TO},\alpha}^4}{\Delta\left(\omega_{\mathrm{LO},\alpha}^2 - \omega_{\mathrm{TO},\alpha}^2\right)}\left\{\omega_{\mathrm{P}}^2\left[\gamma\left(\omega_{\mathrm{LO},\alpha}^2 - \omega_{\mathrm{TO},\alpha}^2\right) + \Gamma\left(\omega_{\mathrm{P}}^2 - 2\omega^2\right)\right] + \omega^2\Gamma\left(\omega^2 + \gamma^2\right)\right\} \end{aligned} \tag{5.6}$$

with

$$\Delta = \omega_{\mathrm{P}}^2\gamma\left[\left(\omega_{\mathrm{TO},\alpha}^2 - \omega^2\right)^2 + \omega^2\Gamma^2\right] + \omega^2\Gamma\left(\omega_{\mathrm{LO},\alpha}^2 - \omega_{\mathrm{TO},\alpha}^2\right)\left(\omega^2 + \gamma^2\right)$$

and C_α^{FH} refers to the Faust-Henry coefficients. According to its wurtzite structure, in hexagonal GaN three Faust-Henry coefficients associated with phonon modes of different symmetry exist (see equation (3.37) in section 3.4). The symmetry of the polar phonon mode and the corresponding Raman tensor element is denoted by the index α. The Faust-Henry coefficients are ratios describing the relative influence of lattice displacements and the electric field onto the dielectric susceptibility [26, 29, 30]. However, in the case of wz-GaN merely the Faust-Henry coefficient connected with the polar phonon mode of A_1 symmetry and its assigned Raman tensor elements a_{TO} and a_{LO} has been reported with differing values and questionable sign [31–35]. This issue will be discussed in chapter 6.

5.2 Determination of charge carrier concentration and mobility

In order to assess free charge carrier density and mobility in GaN layers Raman measurements were carried out. By means of the confocal technique depth dependent information, e.g. concerning the doping profile, can be obtained. Employing the lineshape fitting analysis the carrier concentration and mobility was estimated from measured frequencies, bandwidths and intensities.

5.2.1 Experimental details

Growth of the sample

The epitaxial (0001) GaN layer investigated in the present study was grown by hydride vapor phase epitaxy (HVPE) in a commercial single-wafer system. The HVPE growth was performed on GaN MOVPE[1] templates with a diameter of 2 inch and a layer thickness of 4 μm. The (0001)-oriented sapphire substrate had a thickness of 430 μm. During the growth the epitaxial GaN layer was intentionally doped with silicon (Si).

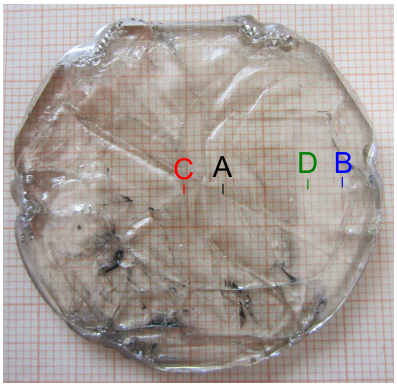

Fig. 5.2: GaN sample grown by HVPE and intentionally doped with Si. The indicated positions mark the measuring points of the confocal Raman scans.

Raman setup

Confocal micro-Raman measurements were carried out at room temperature using backscattering geometry. The experimental setup was the same as described in section 4.2.1. The position z of the focal plane refers to the distance from the surface in this case (cf. figure 4.2(a)).

[1] abbreviation: Metal Organic Vapor Phase Epitaxy

Lineshape fitting

Based on the semiclassical approach introduced in section 5.1 a fitting routine was implemented in MATHEMATICA using the plasma frequency ω_P and the plasmon damping γ as adjustable parameters. Using equations (5.2) and (5.3) the carrier density n and the mobility μ were deduced from the best fit results. As input data the fitting procedure requires the measured spectra as well as several material parameters summarized in table 5.1. According to equation (5.6) the Faust-Henry coefficient C_α^{FH} related to the symmetry of the polar phonon mode and its Raman tensor element is needed for the analysis. The experimental determination of the Faust-Henry coefficients of wz-GaN will be discussed in chapters 6 and 7. Here, it is necessary to anticipate the result of the Faust-Henry coefficient connected with the polar phonon mode of A_1 symmetry and its assigned Raman tensor elements a_{TO} and a_{LO}.

Tab. 5.1: Material parameters of wz-GaN used for the lineshape fitting

Parameter		Reference
$\omega_{\mathrm{TO,A1}}$	531.8 cm^{-1}	[65]
$\omega_{\mathrm{LO,A1}}$	734 cm^{-1}	[65]
Γ	6 cm^{-1}	own data
$\varepsilon_{\infty\parallel}$	5.31	[71]
m^*	0.2 m_0	[103]
C_a^{FH}	-3.46	chapter 6

5.2.2 Results and discussion

Confocal Raman measurements were performed on four different points (see figure 5.2). The scattered light was recorded in backscattering geometry and contained both the $z(yx)\bar{z}$ and $z(yy)\bar{z}$ configurations. According to the selection rules discussed in section 3.5 three phonons ($E_{2,\mathrm{low}}$, $E_{2,\mathrm{high}}$, A_1(LO)) are allowed. Figure 5.3 shows Raman spectra measured at the sample surface (z = 0 μm) and 25 μm beneath the surface. All spectra were normalized with respect to the strong nonpolar $E_{2,\mathrm{high}}$ phonon mode. Contrary to the previous analysis of the residual stress (chapter 4), the present study focuses on the determination of the charge carrier density and mobility. Here, particular attention is paid to the A_1(LO) phonon spectral region. Comparing the two spectra in figure 5.3(a), the observed shift to higher wavenumbers and the broadening of the LO phonon peak in the spectrum taken 25 μm beneath the sample surface can be ascribed to the coupling of free charge carriers to the A_1(LO) phonon resulting in the L_+ coupled mode at 780 cm^{-1}. The corresponding L_- coupled mode appears at about 270 cm^{-1} (see figure 5.3(a)).

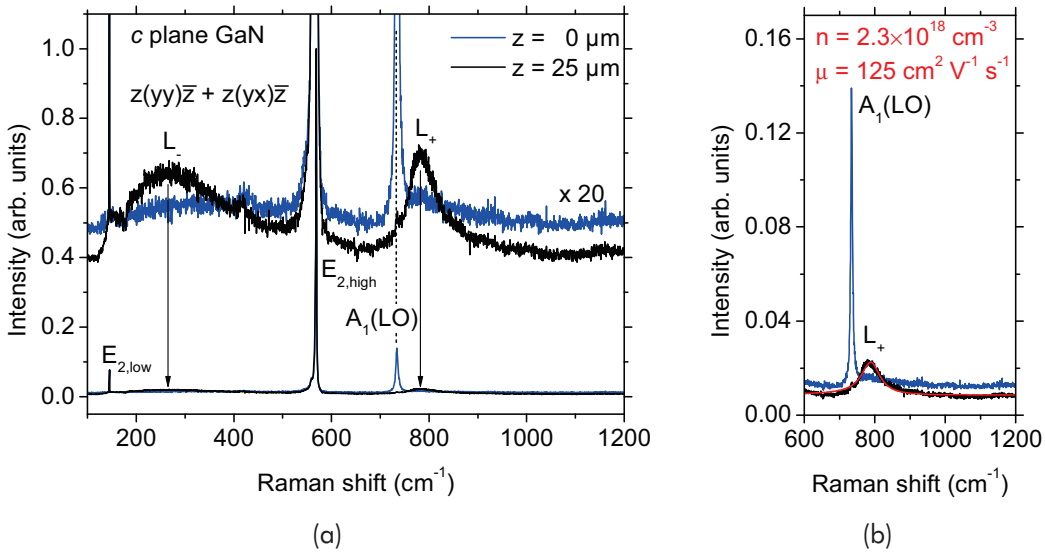

Fig. 5.3: Raman spectra recorded in backscattering geometry at the sample surface (z = 0 μm) and 25 μm beneath the surface. (a) The observed shift to higher frequencies and the broadening in the A_1(LO) phonon spectral region is due to the coupling of free charge carriers to the A_1(LO) phonon resulting in the L_+ coupled mode. The corresponding L_- coupled mode can be detected as well. (b) The charge carrier concentration and mobility was determined by lineshape fitting of the L_+ coupled mode. The fitted curve is represented by the red line.

Using the implemented MATHEMATICA routine which takes the deformation potential and electro-optical scattering mechanisms into account, the lineshape fitting of the L_+ coupled mode revealed a carrier density of about 2.3×10^{18} cm^{-3} and a mobility of 125 cm^2 V^{-1} s^{-1} (see figure 5.3(b)).
The carrier concentration is in fair agreement with the density of 1.19×10^{18} cm^{-3} determined by electrical Hall measurements[2]. In contrast to this classical approach, micro-Raman spectroscopy takes advantage of being a contactless method with high spatial resolution. As GaN is transparent in the visible spectral range, it is possible to obtain depth dependent information by means of the confocal technique. In figure 5.4 a series of Raman spectra taken at point C (see figure 5.2) in dependence on the distance z from the surface (z = 0 μm) is depicted. The depth resolution of about 5 μm was adjusted by the diameter of the confocal hole. All spectra were normalized with respect to the nonpolar $E_{2,high}$ Raman mode and shifted for clarity. The black Raman spectrum from the sample surface (z = 0 μm) is comparable to that one shown in figure 5.3. Within the topmost 25 μm of the GaN layer investigated the intensity of the pure A_1(LO) phonon decreases. Simultaneously, significant indications of the L_+ coupled mode at about 780 cm^{-1} appear. The orange spectrum recorded 25 μm beneath the specimen surface is similar to that one shown in figure 5.3. In the limit of the experimental resolution the carrier density and mobility are the same.

[2]Data kindly provided by Freiberger Compound Materials GmbH.

From the measurements it can be deduced that the influence of free charge carriers dominates up to about 15 μm before end of the GaN layer growth which provides beneficial feedback on the growth process.

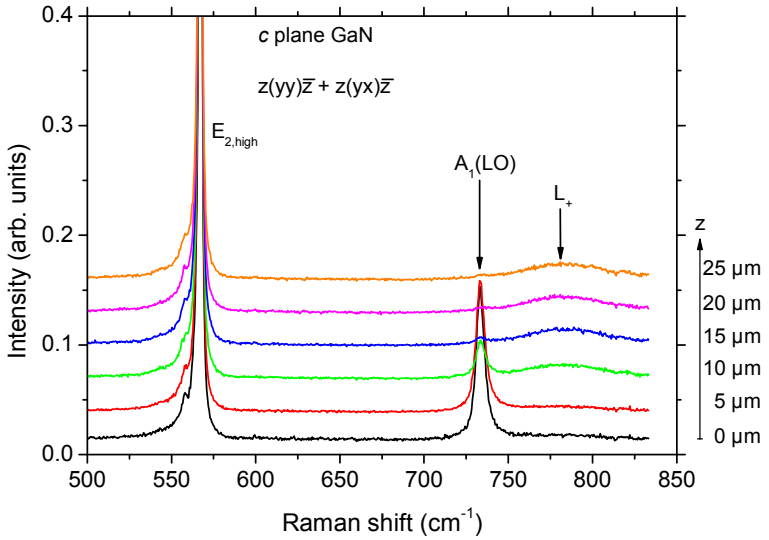

Fig. 5.4: A series of confocal Raman spectra taken in backscattering geometry at point C (see figure 5.2) in dependence on the distance z from the surface (z = 0 μm). All spectra were normalized with respect to the nonpolar $E_{2,high}$ Raman mode.

Furthermore, in case of potential industrial applications (i.e. providing semiconducting GaN wafer for post-processing) it is worth to monitor the vertical extension of the doped zone. For this purpose, confocal measurements were carried out at the points A and B (see figure 5.2) as function of the distance z from the sample surface. The Raman spectra were recorded in backscattering geometry with a depth resolution of about 25 μm. This is meaningful since (i) the measurements are non-destructively and (ii) LO phonons of E_1 symmetry and thus coupled LO phonon plasmon modes are not accessible in backscattering configurations from a surface perpendicular to the c plane (e.g. side edge in direction x), see table 3.1. After background correction the A_1(LO) Raman mode was fitted by a Lorentzian function to detect its spectral position, full width at half maximum (FWHM), and intensity. In figure 5.5 the best fit results in dependence on the distance z from the sample surface are shown. The profiles at point A and B turned out to be very similar indicating the homogeneity of the sample since the scans were performed in the center region and at the edge of the wafer, respectively (see figure 5.2). In order to correlate the experimental findings with the growth process of the GaN layer, the interpretation starts at back side of the investigated sample following the growth direction, i.e. decreasing z (reverse measuring direction). In a first stage, epitaxial GaN was grown intentionally undoped. The recorded spectra in the range 2100 μm ... 1400 μm are similar to that one obtained at the sample surface (see figures 5.3(a) and 5.4). This is confirmed by the spectral

position (figure 5.5(a)) as well as the FWHM (figure 5.5(b)) of the analyzed A_1(LO) phonon mode. The difference in the absolute intensity (figure 5.5(c)) can be ascribed to the attenuation of the incident and scattered light due to the Lambert-Beer law.

In the second growth stage, silicon was added as dopant at a constant level. Within the range 1400 μm ... 900 μm both, coupled L_+ and A_1(LO) modes were observed in the spectra. The intensity of the LO phonon plasmon peak increases whereas the contribution of the A_1(LO) phonon diminishes (see figure 5.5(c)). For comparison, the scaled intensity of the nonpolar $E_{2,high}$ Raman mode (dashed line in figure 5.5(c)) was plotted. In case of the absence of free charge carriers no LO phonon plasmon coupling occurs and the intensity of the A_1(LO) mode shows the same behavior as the intensity of the $E_{2,high}$ phonon (see figure 5.5(c) in the range 2100 μm ... 1400 μm). For distances z from the sample surface smaller than 900 μm (missing data points in figure 5.5) the observed Raman mode in the spectrum is interpreted as coupled mode rather than an A_1(LO) phonon. The deduced charge carrier density is about 2.3×10^{18} cm^{-1} (see figure 5.3(b)).

In the final stage of the growth, the addition of silicon as dopant was ceased in order to prevent undesired effects in the near surface region. The recorded Raman spectrum at the position z = 0 μm was similar to that shown in figure 5.4. No substantial intensity of the L_+ coupled mode was detected.

5.3 Conclusion

In this chapter the influence of free charge carriers on LO phonon modes has been studied. Micro-Raman measurements analyzing the LO phonon plasmon coupling are widely used because such measurements are contactless, non-destructive, and with excellent resolution lateral and in the depth. By means of the confocal technique it was possible to monitor the doping profile of a wz-GaN single crystal. The experimental observations can be directly correlated to the growth process and provide beneficial feedback to the crystal grower. Analyzing the A_1(LO) phonon spectral region of wz-GaN in series of confocal Raman spectra the doped range of the material was deduced to be about 1400 μm. Raman measurements with a high depth resolution revealed the topmost 15 μm GaN layer as well as the first (i.e. in terms of the growth process) 700 μm to be undoped. From the lineshape fitting of the observed L_+ coupled mode the charge carrier density and mobility was determined.
The results $n = 2.3\times10^{18}$ cm^{-3} and $\mu = 125$ cm^2 V^{-1} s^{-1} are in good agreement with Hall measurements. The applied semiclassical approach takes the deformation potential and electro-optical scattering mechanisms into account. Thus, the use of the determined Faust-Henry coefficients was successfully demonstrated.

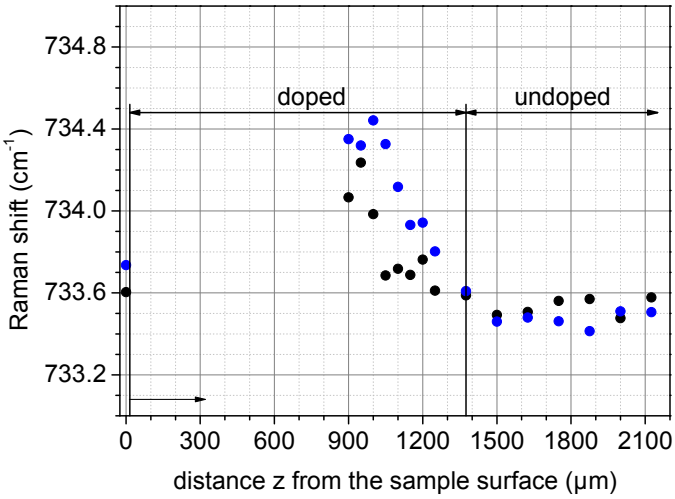

(a)

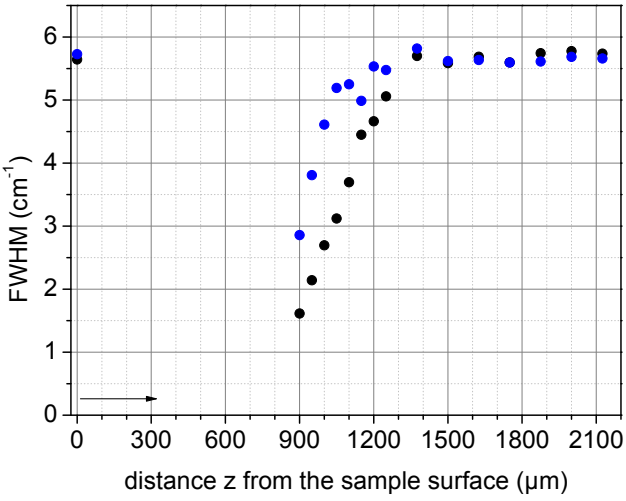

(b)

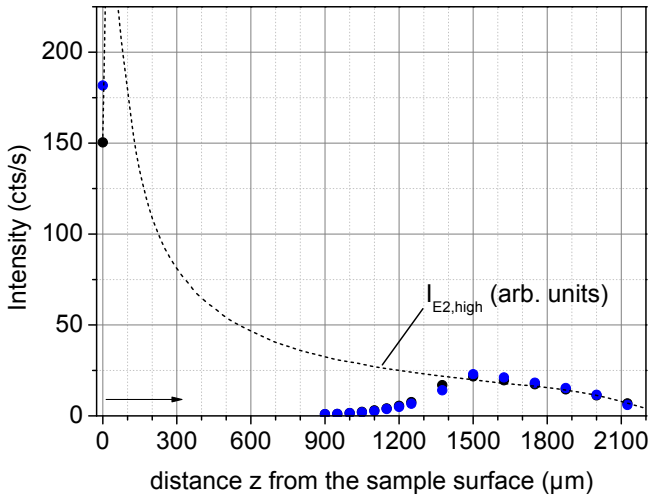

(c)

Fig. 5.5: Fit results of a series of confocal Raman spectra as function of the distance z from the sample surface. The A_1(LO) Raman mode was analyzed with respect to its (a) spectral position, (b) full width at half maximum (FWHM), and (c) intensity. The color indicates depth profiles A and B (see figure 5.2).

6 Faust-Henry coefficients and Raman tensor elements

The results of systematic Raman measurements on wz-GaN single crystals in order to access the Raman scattering efficencies of A_1(TO), A_1(LO), E_1(TO), and E_1(LO) phonons are presented. The experimental setup using different scattering geometries, i.e. 180°, 90°, and 0°, is described in detail. The Faust-Henry coefficients of wz-GaN are calculated based on the ratio of the measured Raman efficiency of the TO phonon to the one of the LO phonon. From the relative Raman scattering cross sections the absolute value of each Raman tensor element of wurtzite-type GaN are determined in dependence on the respective phonon frequency.

6.1 Raman scattering intensity

Equation (3.38) describes the Raman scattering intensity of phonons as well as phonon polaritons. In case of phonons and large wavevectors the matrix elements in equation (3.38) are given by equation (3.42). The term $\left|\vec{e}^{\,\mathsf{S}} \cdot \tilde{R}_N \cdot \vec{e}^{\,\mathsf{L}}\right|^2$ in equation (3.38) denotes the contribution of the Raman tensor elements to the Raman scattering intensity for given polarization vectors of incident and scattered light. In case of polar phonon modes the relation between the Raman tensor elements of transverse and longitudinal optical phonons can be expressed by equation (3.45) using Faust-Henry coefficients. Consequently, the Faust-Henry coefficients (see equation (3.36) in section 3.4) can be obtained by measuring the Raman scattering intensities I_{LO} and I_{TO} of the corresponding LO and TO phonons in an undoped crystal:

$$\frac{I_{\mathsf{LO}}}{I_{\mathsf{TO}}} = \frac{(\omega_{\mathsf{L}} - \omega_{\mathsf{LO}})^4}{(\omega_{\mathsf{L}} - \omega_{\mathsf{TO}})^4} \cdot \frac{\omega_{\mathsf{TO}}}{\omega_{\mathsf{LO}}} \cdot \frac{n(\omega_{\mathsf{LO}}) + 1}{n(\omega_{\mathsf{TO}}) + 1} \cdot \left| 1 + \frac{\omega_{\mathsf{TO}}^2 - \omega_{\mathsf{LO}}^2}{C_\alpha^{\mathsf{FH}} \omega_{\mathsf{TO}}^2} \right|^2 , \tag{6.1}$$

where ω_{L} refers to the frequency of the exciting laser expressed in cm^{-1}. The determination of the Raman scattering intensities requires 180°, 90°, and 0° scattering experiments which are described in the next section.

6.2 Experimental setup

In order to determine the Raman scattering efficiency of all optical phonons accessible in wz-GaN, various scattering geometry configurations are required. Many phonons are detectable in 180° backscattering geometry, the LO(E_1) phonon in 90° geometry and the Raman tensor element b_{LO} of the LO(A_1) phonon only in 0° geometry. The different scattering geometry arrangements used are shown in figure 6.1. In table 3.1 the scattering configurations as well as the corresponding contribution of the Raman tensor elements are summarized as discussed in section 3.5.

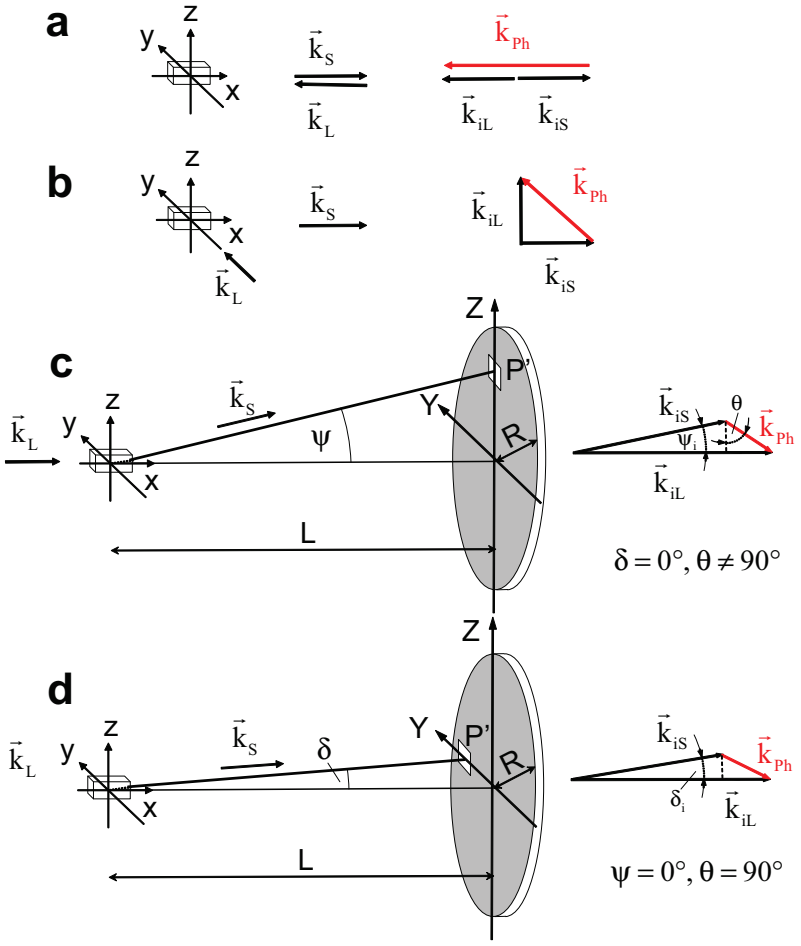

Fig. 6.1: Scattering configurations and transferred phonon wavevector: (a) 180° scattering (backscattering), (b) 90° scattering, (c) 0° scattering (near-forward scattering) in the (x, z) plane, (d) 0° scattering (near-forward scattering) in the (x, y) plane. $\vec{k}_L$ and $\vec{k}_S$ denote the wavevector of the laser light and scattered light, respectively, and $\vec{k}_{Ph}$ refers to the phonon wavevector. The index 'i' indicates the corresponding values inside the crystal.

Most Raman spectra were obtained at room temperature, some backscattering experiments were performed in a temperature range T = 80 K ... 380 K. The lat-

eral dimensions of a typical wz-GaN single crystal investigated in this work were 5×5 mm^2. The typical thickness was about 1 mm.

a. 180° scattering:
Raman measurements were conducted using a Labram HR 800 Raman spectrometer with a thermoelectrically cooled charge-coupled device (CCD) detector. The spectra were excited applying the 532 nm (2.33 eV) line of a frequency-doubled Nd:YAG laser at a power level of about 10 mW at the sample. By passing the linearly polarized laser light through an Olympus microscope objective, the laser beam was focused on the sample surface. The scattered light was collected by the same objective and its polarization was analyzed. In figure 6.1(a) the scattering configuration is depicted with the propagation direction of the exciting laser light and the scattered light along the x axis. Thus, the electric field of incident and scattered light was polarized in the (y, z) plane. If the GaN sample is positioned beneath the microscope with its c axis parallel to the z axis of the laboratory coordinate system, an angle $\theta = 90°$ between phonon wavevector and z axis is realized. Other backscattering measurements were performed with the c axis oriented parallel to the x axis.

b. 90° scattering:
In figure 6.1(b) the 90° scattering arrangement is shown. Raman spectra were obtained using a T 64000 Raman spectrometer (Horiba, Jobin Yvon). The GaN sample was positioned in the macro chamber with its c axis oriented parallel to the z axis of the laboratory coordinate system. The spectra were excited applying the 514.5 nm (2.41 eV) line of an Ar^+-laser at a power level of about 100 mW at the sample. The laser beam was focused onto the sample by a laser objective. After passing the spectrometer equipped with gratings of 1800 grooves/mm in subtractive mode, the scattered light was analyzed by a liquid nitrogen cooled CCD detector. By means of a polarization rotator the laser beam polarization could be changed from (i) parallel to the z axis to (ii) parallel to the x axis. The scattered light was analyzed with polarization parallel or perpendicular to the z axis using an analyzer positioned in the parallel light path between sample and entrance slit of the spectrometer.

c. Near-forward scattering:
The scattering configurations are shown in figures 6.1(c) and 6.1(d). The exciting laser beam was directed along the x axis and enters the entrance surface of the prismatic sample. The screen placed directly in front of the entrance lens of the imaging system is open for scattered light with a small window P' around the point (Y, Z). The scattered light beam includes the angle ψ with the (x, y) plane, and its orthogonal projection on the (x, y) plane the angle δ with the x axis. Afterwards,

the scattered light originating from the focus plane of the entrance lens passes an analyzer and a quartz waveplate which rotates the polarization axis in the position for which the spectrometer throughput is optimized.
Both, laser beam and sample were thoroughly adjusted in order to avoid the capture of laser light into the spectrometer. The laser beam leaving the sample was masked in the centre of the entrance lens of the imaging system. Furthermore, care is necessary to avoid gathering of scattered light excited by the laser beam partly backscattered at the inner crystal surface. As in the case of 90° scattering the 514.5 nm line of the exciting Ar^+-laser was used and the sample was mounted in the macro chamber of the Raman spectrometer T 64000. The exciting laser beam was focused onto the sample by a laser objective.

6.3 Results and discussion

6.3.1 180° scattering

The corresponding scattering configurations listed in table 3.1 depend on the Raman tensor elements a_{TO}, a_{LO}, b_{TO}, c_{TO}, and d. In the following the determination of the Raman scattering cross sections of both, the A_1(TO) and the A_1(LO) phonons is discussed in more detail. Figure 6.2 shows results of a typical measurement. All spectra were normalized with respect to the strong and narrow nonpolar $E_{2,\mathrm{high}}$ phonon mode. The Raman scattering intensities were determined as areas under the phonon bands by numerical integration. In order to separate the bands to be measured from weak phonon bands forbidden according to the selection rules the phonons were fitted by a sum of peak functions. As all phonon bands are more or less asymmetrically as shown in figure 6.3 fitting with one simple function does not work well. In order to exclude a possible contribution of two-phonon modes, temperature dependent measurements in the range 80 K ... 380 K have been performed. Due to the different temperature dependence of one-phonon and two-phonon processes the contribution of the latter should be negligible at low temperatures. However, the asymmetry can be also observed at low temperatures, see figure 6.3.

6.3.2 90° scattering

The measurement of the E_1(LO) phonon requires a 90° scattering arrangement. Figure 6.4 shows typical spectra of a wz-GaN single crystal. In this case the wavevectors of incident and scattered light are

$$\begin{aligned} \vec{k}_{\mathrm{L}} &= k_{\mathrm{L}}(0,1,0), \\ \vec{k}_{\mathrm{S}} &= k_{\mathrm{S}}(1,0,0), \end{aligned} \tag{6.2}$$

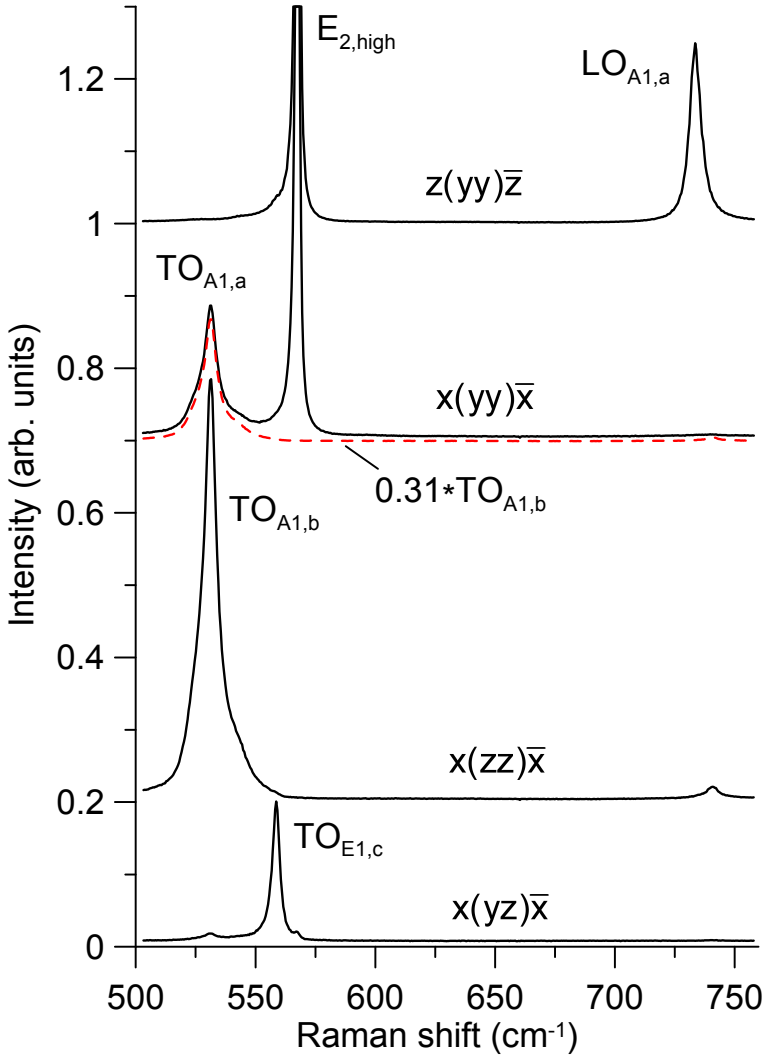

Fig. 6.2: Raman spectra of a wz-GaN single crystal recorded in backscattering geometry employing (i) $z()\bar{z}$ configuration (z along growth direction of the crystal) and (ii) $x()\bar{x}$ configurations (from a surface in direction x). The two letters in brackets indicate the polarization direction of the incident and scattered light, respectively. The spectra were normalized with respect to the $E_{2,high}$ phonon mode and shifted for clarity.

and according to equation (3.27) the phonon wavevector is

$$\vec{k}_{\mathrm{Ph}} = \vec{k}_{\mathrm{L}} - \vec{k}_{\mathrm{S}} \approx k_{\mathrm{Ph}} \cdot \frac{1}{\sqrt{2}}(-1, 1, 0). \tag{6.3}$$

Due to $k_{\mathrm{S}} \approx k_{\mathrm{L}}$, the angles are $\varphi = 135°$ and $\theta = 90°$. For the polarization configuration (zy) the polarization vectors are

$$\begin{aligned} \vec{e}^{\,\mathrm{L}} &= (0, 0, 1), \\ \vec{e}^{\,\mathrm{S}} &= (0, 1, 0). \end{aligned} \tag{6.4}$$

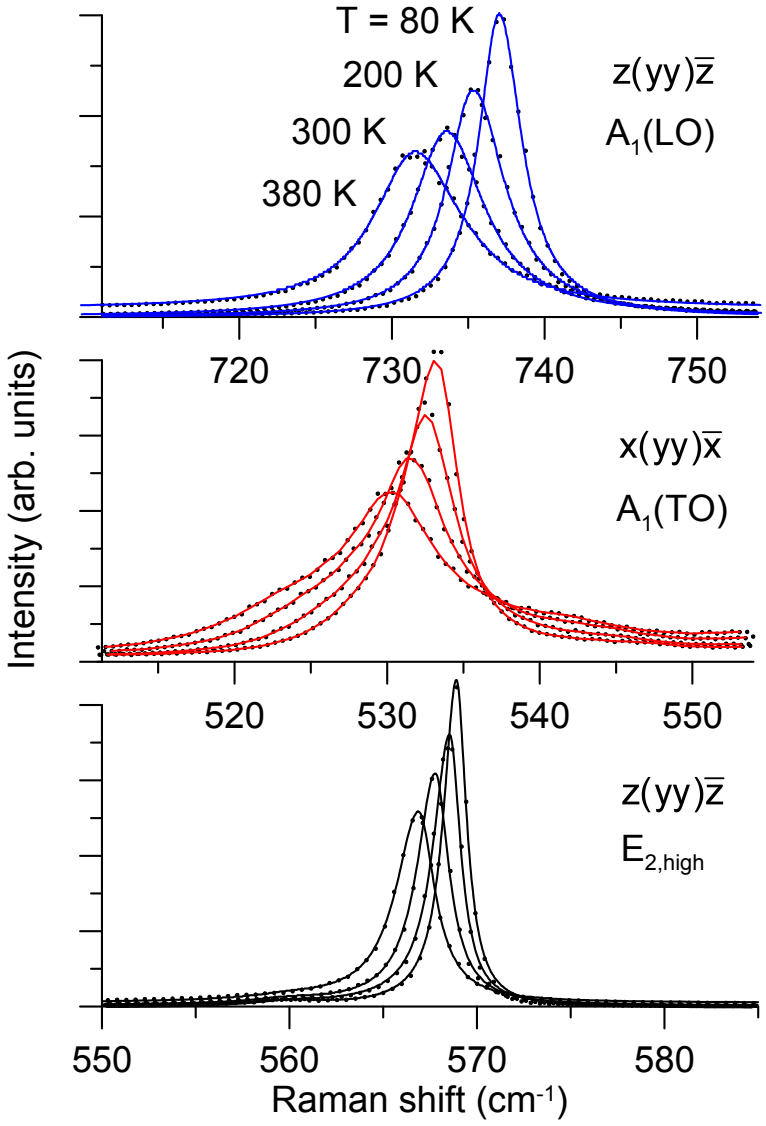

Fig. 6.3: Profiles of phonon bands as function of the temperature. The Raman spectra recorded in backscattering of the A_1(LO) and A_1(TO) phonons were normalized with respect to the $E_{2,high}$ phonon intensity obtained in $z(yy)\bar{z}$ and $x(yy)\bar{x}$ configuration, respectively.

With $\omega = \omega_{TO,E1}$ in equation (3.39) and $\omega = \omega_{LO,E1}$ in equation (3.41) one obtains

$$\begin{aligned} \left| \vec{e}^{\,S} \cdot \tilde{R}_{To} \cdot \vec{e}^{\,L} \right|^2 &= \frac{1}{2} c_{TO}^2, \\ \left| \vec{e}^{\,S} \cdot \tilde{R}_{Le} \cdot \vec{e}^{\,L} \right|^2 &= \frac{1}{2} c_{LO}^2. \end{aligned} \tag{6.5}$$

The two other expressions deduced from equations (3.40) and (3.47) are

$$\left| \vec{e}^{\,S} \cdot \tilde{R}_{Te} \cdot \vec{e}^{\,L} \right|^2 = \left| \vec{e}^{\,S} \cdot \tilde{R}_{E_{2,high}} \cdot \vec{e}^{\,L} \right|^2 = 0. \tag{6.6}$$

For the polarizations (zz) and (xy) the nonvanishing expressions are

$$\left| \vec{e}^{\,S} \cdot \tilde{R}_{Te} \cdot \vec{e}^{\,L} \right|^2 = b_{TO}^2, \tag{6.7}$$

with $\omega = \omega_{\mathrm{TO,A1}}$ and

$$\left| \vec{e}^{\,\mathrm{S}} \cdot \tilde{R}_{E_{2,\mathrm{high}}} \cdot \vec{e}^{\,\mathrm{L}} \right|^2 = d^2. \tag{6.8}$$

In the spectrum $y(zy)x$ the E_1(LO) as well as the E_1(TO) phonon can be observed, whose intensity can be obtained from backscattering measurements as well (see figure 6.2).

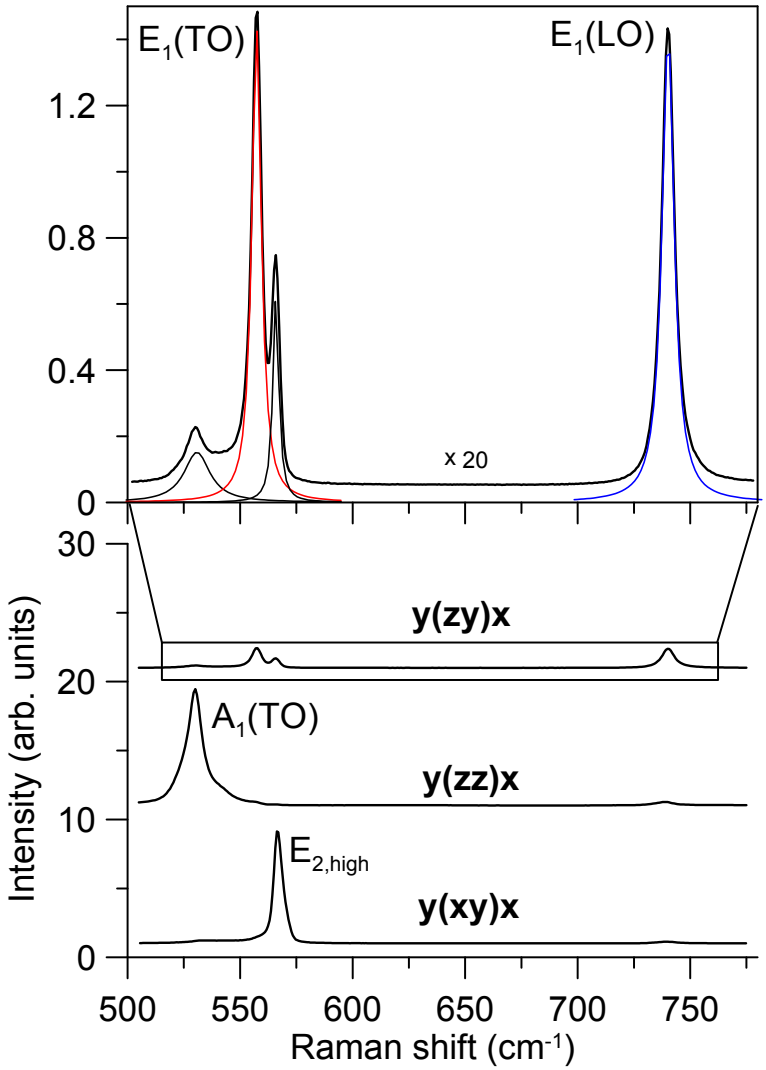

Fig. 6.4: Raman spectra of a wz-GaN crystal recorded in 90° scattering geometry. The spectra were normalized with respect to the $E_{2,\mathrm{high}}$ phonon intensity obtained in $y(xy)x$ configuration. All spectra in the lower panel are shifted for clarity. The upper panel shows the experimental data of the $y(zy)x$ configuration and the fit results in more detail.

It should be noted that the determination of the intensity ratio $r = I_{\mathrm{LO,E1}}/I_{\mathrm{TO,E1}}$ requires special care. Small deviations Δ from the exact scattering angle 90° have strong influence onto the ratio r which is given by

$$r(\Delta) = r(90°) \cdot \frac{\sin^2(90° + \Delta)}{[1 - \cos(90° + \Delta)]^2}. \tag{6.9}$$

The ratio r has no extremum at $\Delta = 0$ but diminishes for $\Delta > 0$ and rises for $\Delta < 0$. Therefore, the crystal has to be positioned very carefully. The relative intensity $I_{\mathrm{LO,E1}}$ presented in table 6.1 is the mean value of 8 measurements with different rectangular single crystals and changing the crystal orientation by 90° rotation around the z axis.

6.3.3 0° scattering

Raman scattering of the A_1(LO) phonon with the tensor element b_{LO} responsible for it requires the polarization (zz) of the incident/scattered light. On the other hand a wavevector component in z direction is necessary for observation of the A_1(LO) phonon propagating in z direction. This can be achieved with near-forward scat-

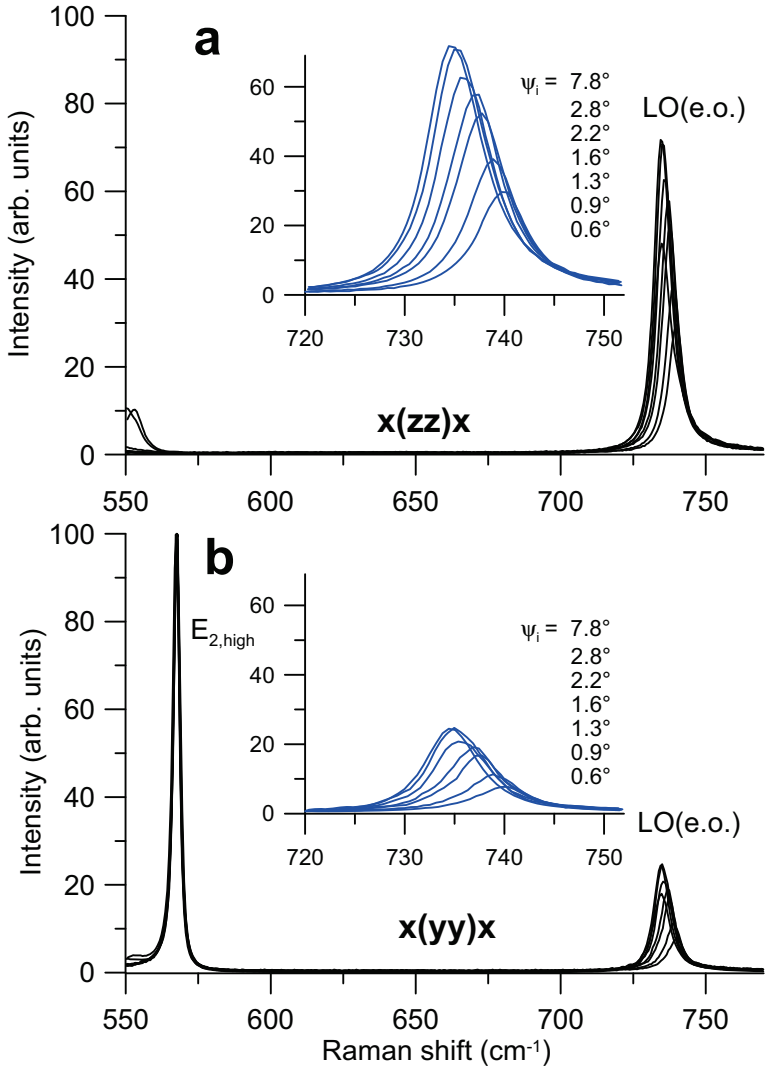

Fig. 6.5: Raman spectra of the LO(e.o.) phonon: 0° scattering in the (x, z) plane (see figure 6.1(c)). The spectra are shown as function of the angle ψ_{i} between incident and scattered light wavevectors k_{iL} and k_{iS}. The spectra were normalized with respect to the $E_{2,\mathrm{high}}$ phonon intensity. The Raman tensor elements b_{LO} and a_{LO} are responsible for the scattered intensity of the LO(e.o.) phonon using the $x(zz)x$ and $x(yy)x$ configurations, respectively.

tering in (x, z) plane, for instance (see figure 6.1(c)). Observation is possible with a near-forward scattering in x direction. Assuming $\vec{k}_S \approx \vec{k}_L$ the phonon wavevector would be nearly parallel to the z axis for small angles ψ_i. However, for Stokes scattering due to $k_S = 2\pi n_S/\lambda_S < k_L = 2\pi n_L/\lambda_L$ the phonon wavevector has also components in x direction. Taking the refraction at the crystal boundary into account, the smallest angle θ between the phonon wavevector and the z axis achievable using the laser wavelength 514.5 nm is about 19°. From table 3.1 it is apparent that the intensity of the A_1(LO) phonons measured in the configurations $x(zz)x$ and $x(yy)x$ gives the b_{LO}^2/a_{LO}^2 ratio independent on the angle θ. Figure 6.5 shows spectra measured

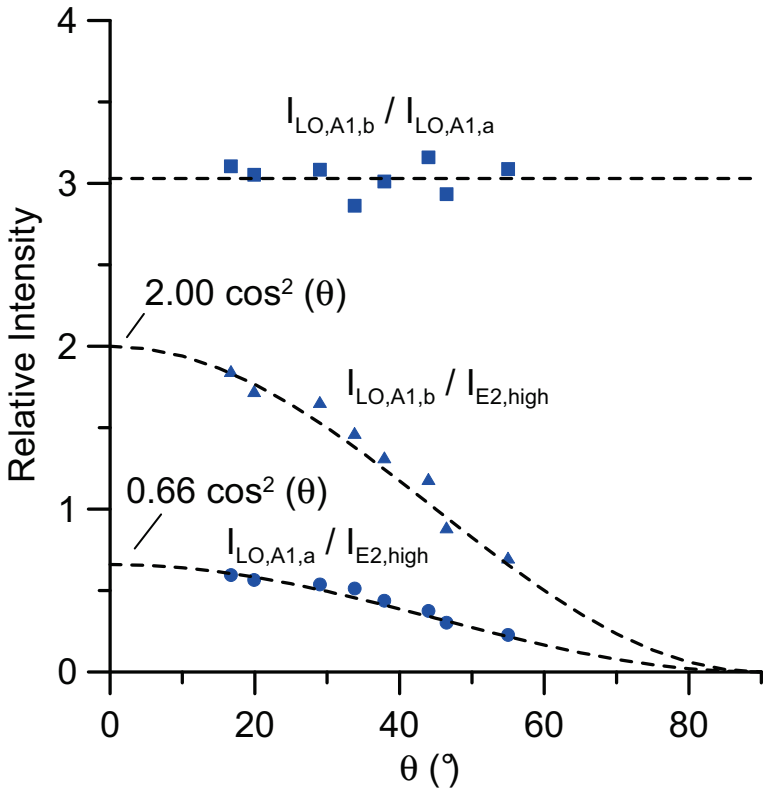

Fig. 6.6: Intensities of the LO(e.o.) phonon obtained in the $x(zz)x$ and $x(yy)x$ scattering configuration as function of the angle θ between phonon wavevector and c axis of the wz-GaN single crystal. The spectra were normalized with respect to the $E_{2,high}$ phonon intensity. The mean value of the ratio of the LO(e.o.) phonon intensities from the two configurations is 3.03.

with different positions of the window P′ on the Z axis of the screen in front of the entrance lens of the spectrometer ($Y = 0$). The scattered light stems from scattering processes inside the crystal with angles ψ_i between the wavevectors k_{iS} and k_{iL}. With decreasing angle ψ_i the x component of k_{Ph} and the angle θ enlarge. Accordingly, the frequency of the extraordinary LO phonon shifts and the contribution of the Raman tensor elements with A_1 symmetry diminishes. The configuration $x(zz)x$ allows contributions of the element b_{TO} as well. Due to the small phonon wavevector magnitude in near-forward scattering extraordinary polaritons with frequencies downshifted

from the frequency $\omega_{\mathrm{TO,A1}}$ are observed. Further details concerning phonon polaritons will be discussed in the next chapter. The spectra in figure 6.5 were normalized with respect to the $E_{2,\mathrm{high}}$ intensity. In figure 6.6 it is shown that the intensity ratio of the LO(A_1) phonons measured with both polarizations is nearly constant.

6.3.4 Relative Raman scattering cross sections

In table 6.1 the Raman scattering cross sections of wz-GaN relative to the $E_{2,\mathrm{high}}$ phonon mode are summarized. Reports on measurements of relative or absolute Raman cross sections of phonons in wz-GaN are scarce in the literature. Loa *et al.*[36] describe measurements of absolute and relative efficiencies of the phonons which are accessible in backscattering configurations. Using their values obtained on the sample wz-GaN (3.4 μm) the ratio

$$\frac{I_{\mathrm{LO,A1,a}}(z(xx)\bar{z})}{I_{\mathrm{TO,A1,a}}(x(yy)\bar{x})} = \frac{0.43}{0.54} = 0.80 \tag{6.10}$$

arises.
Pezzotti *et al.*[107] investigated intensity variations of the polarized Raman bands of E_1(TO), A_1(TO) and E_2 wz-GaN phonons by 180° scattering as a function of the in-plane rotation angle using the a plane of the crystal. However, comparisons between the intensities of the different phonons are not given. From fits of the A_1(TO) phonon intensities as function of the rotation angle they found for the two Raman tensor contributions $a = 0.181$ and $b = -0.859$. This corresponds to an intensity ratio

$$\frac{I_{\mathrm{TO,A1,a}}}{I_{\mathrm{TO,A1,b}}} = \frac{a^2}{b^2} = 0.044 \tag{6.11}$$

which is much lower than the result 0.32 for this ratio obtained in the present work or the value 0.22 calculated with relative intensities given in [36]. A possible reason for the differences could be the fit procedure for A_1(TO) based on an incorrect equation (20) in [107]. Inserting $\vec{e}^{\,\mathrm{S}} = \vec{e}^{\,\mathrm{L}} = (0, \cos\phi, \sin\phi)$, $\theta = 90°$ and $\omega_{\mathrm{TO,A1}} = 531.8$ cm^{-1} in equations (3.38) and (3.40) one yields

$$\begin{aligned} I^{\parallel}_{\mathrm{TO,A1}} \sim \left| \vec{e}^{\,\mathrm{S}} \cdot \tilde{R}_{\mathrm{Te}} \cdot \vec{e}^{\,\mathrm{L}} \right|^2 &= \left(a_{\mathrm{TO}} \cos^2\phi + b_{\mathrm{TO}} \sin^2\phi \right)^2 \\ &= \frac{1}{4} \left[(a_{\mathrm{TO}} + b_{\mathrm{TO}}) + (a_{\mathrm{TO}} - b_{\mathrm{TO}}) \cos 2\phi \right]^2 . \end{aligned} \tag{6.12}$$

This corresponds to the 180° scattering along the x axis of an a plane oriented crystal (see figure 6.1) where the angle ϕ lies in the a plane and is defined as angle between the rotator/analyzer and the c axis. Measurements with angles $\phi = 0°$ and $\phi = 90°$ correspond to the configurations $x(yy)\bar{x}$ with $I^{\parallel}_{\mathrm{TO,A1}} \sim a^2_{\mathrm{TO}}$ and $x(zz)\bar{x}$ with $I^{\parallel}_{\mathrm{TO,A1}} \sim b^2_{\mathrm{TO}}$, shown in figure 6.2. Measurements of $I_{\mathrm{TO,A1,a}}$ and $I_{\mathrm{TO,A1,b}}$ are easy to perform

with our backscattering configurations $x(yy)\bar{x}$ and $x(zz)\bar{x}$, rotating the sample around the x-axis by 90°.

Regarding the scattering cross sections of the E_1(LO) phonon and the A_1(LO) phonon related to the b_{LO} Raman tensor element there is no data available in literature.

Tab. 6.1: Raman scattering cross section of wz-GaN relative to the $E_{2,high}$ phonon mode

Raman mode	Raman shift (cm^{-1})	Relative scattering cross section
$E_{2,high}$	567.6	1
$E_{2,low}$	144	$(0.40\pm0.05)\cdot10^{-2}$
A_1(TO)	531.8	0.63 ± 0.02
		1.98 ± 0.03
A_1(LO)	734	0.66 ± 0.02
		2.00 ± 0.03
E_1(TO)	558.8	0.35 ± 0.02
E_1(LO)	741	0.43 ± 0.02

6.3.5 Faust-Henry coefficients

The relative Raman scattering intensities summarized in table 6.1 were used in order to calculate the Faust-Henry-coefficients according to equation (6.1). Owing to the quadratic term for each coefficient C_α^{FH} two possible solutions can be found. The two analytical solutions are shown in figure 6.7 by the red solid line in case of A_1 symmetry. The vertical lines refer to the intensity ratio $I_{LO,A1,a}/I_{TO,A1,a} = 1.05$ (green) and $I_{LO,A1,b}/I_{TO,A1,b} = 1.01$ (blue), respectively. The intersections give the graphical solutions of the corresponding Faust-Henry coefficients C_a^{FH} and C_b^{FH}. The calculation yields:

$$\begin{aligned} C_a^{FH} &= \{0.40, -3.46\}, \\ C_b^{FH} &= \{0.40, -3.81\}, \\ C_c^{FH} &= \{0.33, -2.31\}. \end{aligned}$$

The two solutions with different sign correspond to destructive or constructive superposition of the deformation potential scattering and the electro-optical scattering.

Among the three Faust-Henry coefficients, C_a^{FH} is the only one that has been used up to now in connection with determination of free carrier concentration and mobility with coupled LO phonon plasmon modes (see chapter 5). Some authors used simple Drude theory for cubic crystals without any Faust-Henry coefficients in order to obtain carrier concentrations from coupled LO phonon plasmon modes [108–112] or an empiric equation [113, 114], but this level is suitable only for crude estimations of

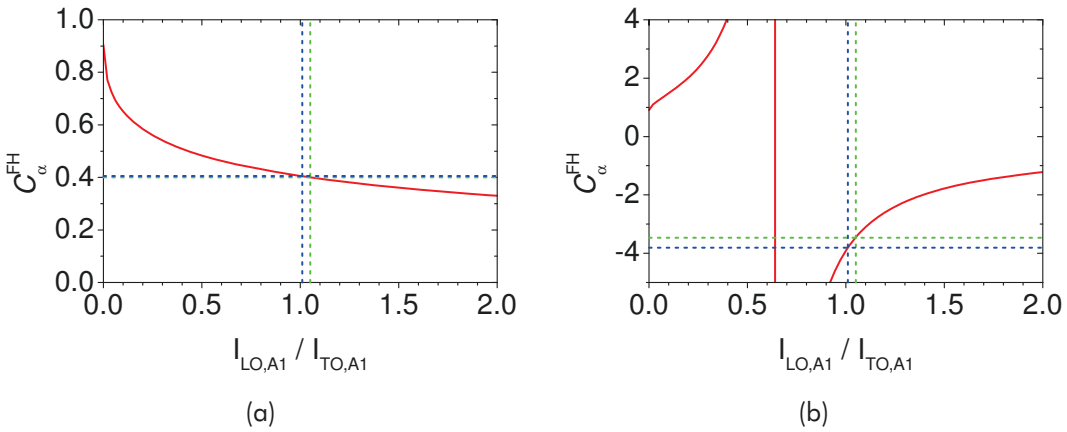

Fig. 6.7: Two analytical solutions of equation (6.1) with respect to C_α^{FH} in case of A_1 symmetry. The vertical dashed lines indicate the experimentally determined intensity ratios $I_{LO,A1,a}/I_{TO,A1,a}$ = 1.05 (green) and $I_{LO,A1,b}/I_{TO,A1,b}$ = 1.01 (blue), see table 6.1. The intersections between the vertical dashed lines and the red curve denote the Faust-Henry coefficients connected with the Raman tensor elements a and b, respectively.

carrier concentrations. The value of the Faust-Henry coefficient was introduced applying different methods. In the period before its first determination, some authors used the value C^{FH} = -0.5 of cubic GaAs [115, 116]. Later, in the analysis of coupled LO phonon plasmon modes C_a^{FH} was simply regarded as a fit parameter and the values 0.4 [31, 117, 118] or 0.48 [25, 34, 119, 120] were used. Measurements based on the determination of TO(A_1) and LO(A_1) phonons gave the values -5.2 [32], -3.8 [33] and 0.52 [121]. The values -5.2 and -3.8 were later adopted by other authors, too [22, 24].

Using the relative Raman scattering efficiency $I_{LO,A1,a}/I_{TO,A1,a}$ = 0.80 reported by Loa *et al.*[36] and applying equation (6.1) results in the Faust-Henry coefficient C_a^{FH} = $\{0.43, -9.1\}$. Better agreement with the ratio $I_{LO,A1,a}/I_{TO,A1,a}$ = 1.05 of this work (see table 6.1) results from comparison with measurements of the relative scattering cross sections of these phonons performed by other authors. The values 1.01 and 0.95 for the ratio $I_{LO,A1,a}/I_{TO,A1,a}$ can be deduced from the Faust-Henry coefficient C_a^{FH} reported by Demangeot *et al.*[33] and Wetzel *et al.*[32], respectively.

Due to most common c plane orientation of wz-GaN crystals, the Faust-Henry coefficient C_a^{FH} is most important in order to deduce charge carrier density and mobility from Raman measurements in backscattering geometry (see chapter 5). Additionally, the temperature dependence of this Faust-Henry coefficient C_a^{FH} was examined in the range T = 80 K ... 380 K (see figure 6.8). However, at this stage the sign of the Faust-Henry coefficients in wz-GaN can not be clearly assigned. In the next chapter it is shown that near-forward scattering of phonon polaritons depending on the frequency allows to determine the sign of Faust-Henry coefficients unambiguously. Here, it is necessary to anticipate the result excluding the solutions with the positive

sign of the coefficients (see chapter 7). Therefore, in figure 6.8 the value of C_a^{FH} with the negative sign is depicted as function of the temperature.

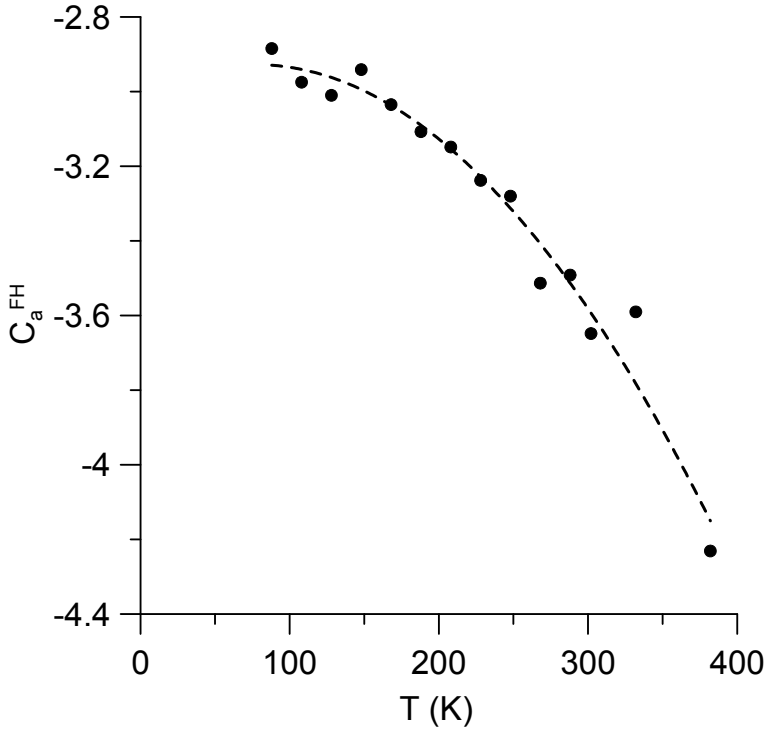

Fig. 6.8: Faust-Henry coefficient C_a^{FH} of wz-GaN as function of temperature.

6.3.6 Raman tensor elements

Conclusions from Raman scattering intensities on Raman tensor elements require account for the dependence of the scattering cross sections on the phonon frequencies. In order to determine the Raman tensor elements of the TO phonons relative to the one of the $\mathsf{E}_{2,\mathsf{high}}$ phonon mode the following expression similar to equation (6.1) was used:

$$t_l^2 = \frac{(\omega_{\mathsf{L}} - \omega_{E_{2,\mathsf{high}}})^4}{(\omega_{\mathsf{L}} - \omega_l)^4} \cdot \frac{\omega_l}{\omega_{E_{2,\mathsf{high}}}} \cdot \frac{n(\omega_{E_{2,\mathsf{high}}}) + 1}{n(\omega_l) + 1} \cdot \frac{I_l}{I_{E_{2,\mathsf{high}}}} \cdot d^2_{E_{2,\mathsf{high}}}, \tag{6.13}$$

where l numbers the Raman tensor element $t_l = (a_{\mathsf{TO}}, b_{\mathsf{TO}}, c_{\mathsf{TO}})$ and the relative Raman intensity $I_l = (I_{\mathsf{TO,A1}}, I_{\mathsf{TO,A1}}, I_{\mathsf{TO,E1}})$ connected with the contribution of the corresponding Raman tensor element. $\omega_1 = \omega_2 = \omega_{\mathsf{TO,A1}}$ ($\omega_3 = \omega_{\mathsf{TO,E1}}$) denote the Raman frequencies of the TO phonon of A_1 (E_1) symmetry.

Subsequently, the Raman tensor elements of the LO phonons were calculated using equation (3.45). For this purpose, the solutions of the Faust-Henry coefficients with the negative sign were applied (for details see section 7.3):

C_a^{FH} = -3.46, C_b^{FH} = -3.81, and C_c^{FH} = -2.31.

The Raman tensor elements are summarized in table 6.2. It should be noted that the ratio $I_{\mathrm{LO,A1,b}}/I_{\mathrm{LO,A1,a}}$ equals $b^2_{\mathrm{LO}}/a^2_{\mathrm{LO}}$.

Tab. 6.2: Raman tensor elements of wz-GaN relative to the $E_{2,\mathrm{high}}$ phonon mode

Raman mode	Raman shift (cm^{-1})	Raman tensor element
$E_{2,\mathrm{high}}$	567.6	$d^2_{\mathrm{E2,high}} = 1$
$E_{2,\mathrm{low}}$	144	$d^2_{\mathrm{E2,low}} = (0.49\pm0.05)\cdot10^{-3}$
A_1(TO)	531.8	$a^2_{\mathrm{TO}} = 0.58\pm0.02$
		$b^2_{\mathrm{TO}} = 1.82\pm0.03$
A_1(LO)	734	$a^2_{\mathrm{LO}} = 0.92\pm0.02$
		$b^2_{\mathrm{LO}} = 2.78\pm0.03$
E_1(TO)	558.8	$c^2_{\mathrm{TO}} = 0.34\pm0.02$
E_1(LO)	741	$c^2_{\mathrm{LO}} = 0.61\pm0.02$

6.4 Conclusion

For the first time, a complete set of the relative Raman scattering cross sections of all Raman modes for wz-GaN was determined. The systematic Raman measurements in order to access the Raman scattering efficiencies require the application of different scattering geometries which were described in detail. Based on these measurements, the Faust-Henry coefficients in wz-GaN were deduced. Faust-Henry coefficients describe the contributions of the lattice displacements and the electric field associated with them to the Raman scattering efficiency. Whereas in cubic crystals one Faust-Henry coefficient is sufficient, in wurtzite crystals three coefficients appear (see section 3.4). They give important information about the deformation potential and the electro-optic tensor. Nevertheless, the sign of these coefficients can not be clearly assigned at this stage of the work.

Values of the Faust-Henry coefficients are necessary for the determination of charge carrier concentration and mobility from Raman measurements (see chapter 5). Up to now in the literature only the coefficient C^{FH}_a was determined with different results and signs. In the present study an accurate determination of that Faust-Henry coefficient including its temperature dependence is reported. Whereas the coefficient C^{FH}_a is important for measurements on the commonly used c plane GaN, for other orientations and measurements the coefficients C^{FH}_b and C^{FH}_c become necessary.

Using the determined Raman scattering cross sections and the obtained Faust-Henry coefficients, the Raman tensors for wz-GaN were calculated. For this purpose, the dependence of the Raman scattering cross sections on the phonon frequencies was taken into account.

7 Light scattering by phonon polaritons in uniaxial crystals

Besides discussion of general aspects of phonon polaritons for uniaxial crystals, theoretical expressions of their Raman scattering efficiency are derived in this chapter. After a detailed description of the novel experimental near-forward scattering setup using rectangular apertures, systematic measurements of ordinary and extraordinary phonon polaritons with defined symmetry as function of the wavevector magnitude are presented. It is demonstrated which range of wavevectors is attainable by Raman measurements using the developed experimental near-forward scattering setup. This strongly depends on the anisotropic properties of the hexagonal crystal and can be selected by a proper polarization arrangement. The conditions which have to be fulfilled in order to detect the topmost dispersion branch (more photonlike) are discussed. Moreover, it will be shown, that measurements of scattering efficiencies on phonon polaritons depending on frequency can be also used to determine Faust-Henry coefficients unambiguously. These coefficients are essential in order to access the charge carrier concentration as well as the mobility by Raman scattering from measured frequencies, bandwidths, and intensities of coupled phonon plasmon modes as demonstrated in chapter 5.

7.1 Theoretical background

In polar crystals, infrared photons strongly interact with the transverse modes of infrared active phonons if their energies are nearly equal. The elementary excitations derived are called phonon polaritons. They have mixed electromagnetic and mechanical nature and their existence has been predicted by Huang [66, 67].
Henry and Hopfield [122] were the first who observed Raman scattering of phonon polaritons in GaP in 1965. Later, phonon polaritons of several other polar semiconductors [123–127] and numerous ferroelectric crystals [128–140] have been investigated (for reviews see: [69, 81, 141–143]) and also surface polaritons in thin films and confined structures [144–146].
However, reports on Raman studies of phonon polaritons in uniaxial semiconductors are scarce. There is especially a lack of data on the relative scattering intensities of

the phonon polaritons. They reflect the changing character of the phonon polaritons depending on their frequency from more photonlike to more phononlike. Contributions of the lattice displacements and the electric field associated with them to the scattering efficiency interfere constructively or destructively.
First, the dispersion of the ordinary and extraordinary polaritons will be discussed.

7.1.1 Ordinary polaritons

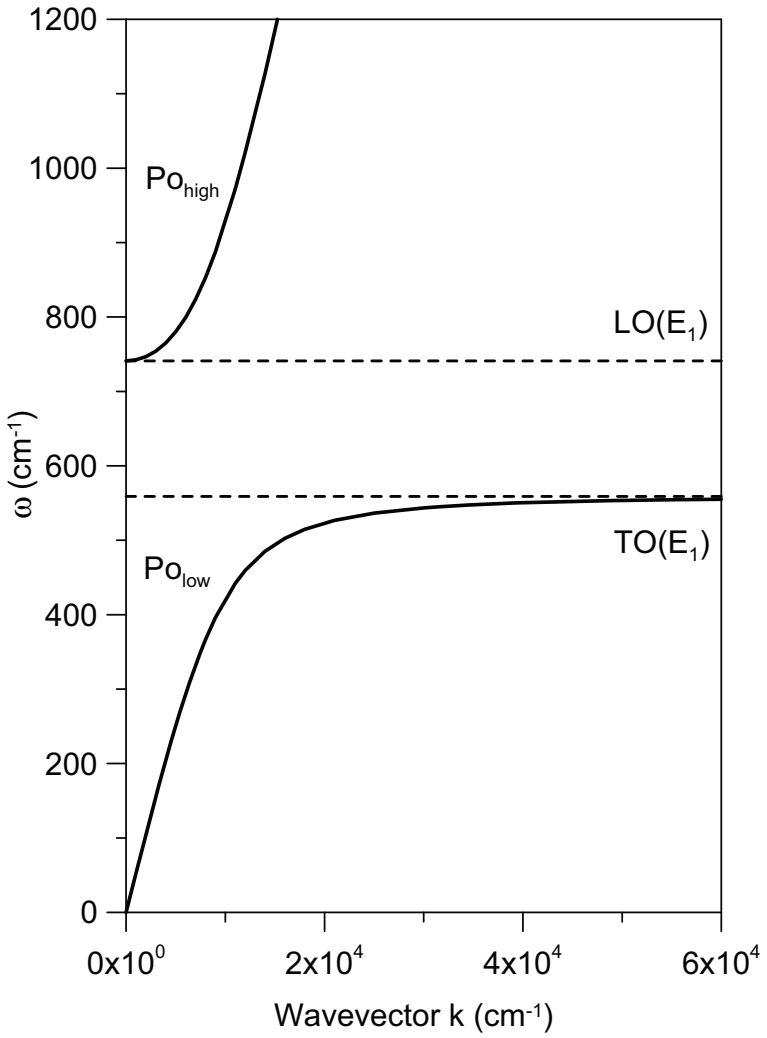

Fig. 7.1: Solutions of equation (3.16): Dispersion of the phononlike Po_{low} and the photonlike Po_{high} branches of the ordinary polariton in wz-GaN (E_1 type) as function of the wavevector k. Reprinted figure with permission from [68]. Copyright 2013 American Physical Society.

The dielectric function for the propagation in the optically isotropic plane $\varepsilon_\perp(\omega)$ was already derived in section 3.2.1 and is given by equation (3.17). The dependence on the wavevector k is expressed by equation (3.16). This equation is a quadratic equation in ω^2. Its solution gives two polariton branches which do not depend on the angle θ. For $k \to 0$ the lower branch converges to zero and the upper to the frequency

of the LO(E_1) phonon mode. For large k the lower branch reaches the frequency of the transverse phonon TO(E_1) (see figure 7.1).

7.1.2 Extraordinary polaritons

In case of extraordinary polaritons the dielectric function was derived in section 3.2.2. Equation (3.19) describes the directional dispersion (see section 3.2.3) as well as the dispersion as a function of the wavevector. As mentioned above, this equation is cubic in ω^2 and can be solved analytically using Cardano's formula[72]. The three real solutions describe the three branches of the extraordinary polaritons[1]. In the following, $\omega(\vec{k})$ in dependence on the angle θ between the wavevector and the z axis is discussed.

a. $\theta = 0°$:
The low branch converges for $k \to 0$ to zero and the high branch to $\omega_{\mathrm{LO,E1}}$. From the solution $\varepsilon_{\parallel}(\omega) = 0$, the LO($A_1$) phonon is obtained with $\omega = \omega_{\mathrm{L}\parallel}$. The other solutions describe the extraordinary transverse polaritons associated with polaritons of E_1 type with displacements parallel to the c axis. These branches coincide with the directionally independent ordinary polariton of E_1 type (figure 7.1). The frequency of the middle branch is independent on k. For large k, the low branch reaches $\omega_{\mathrm{TO,E1}}$.

b. $\theta = 90°$:
The low branch converges for $k \to 0$ to zero and the high branch to $\omega_{\mathrm{LO,E1}}$. The frequency of the middle branch corresponds to $\omega_{\mathrm{LO,E1}}$ and is independent on k. Since the polariton is of A_1 type for large k the low branch reaches $\omega_{\mathrm{TO,A1}}$.

c. $0° < \theta < 90°$:
For $k \to 0$ the low branch reaches zero and the high branch $\omega_{\mathrm{LO,E1}}$. The middle branch shows dispersion depending on the value k with frequencies ranging between $\omega_{\mathrm{LO,A1}}$ and $\omega_{\mathrm{LO,E1}}$. The low branch converges for large k to a frequency value between $\omega_{\mathrm{TO,A1}}$ and $\omega_{\mathrm{TO,E1}}$. The frequency limits for $k \to \infty$ can be calculated for the low and the middle branch using equation (3.19). As an example, figure 7.2 shows the extraordinary polaritons for $\theta = 45°$ and in the insets for other angles θ

[1] Conventionally, the notation polariton is restricted to the transverse polariton branches with their strong frequency dependence. On the contrary, the changes in the LO frequencies are minor. However, for small wavevectors ($k < 5 \times 10^3$ cm^{-1}) interaction between phonon and photon can be seen (figure 7.2). Therefore, in this work the notation polariton is used for all branches which are solutions of equation (3.19).

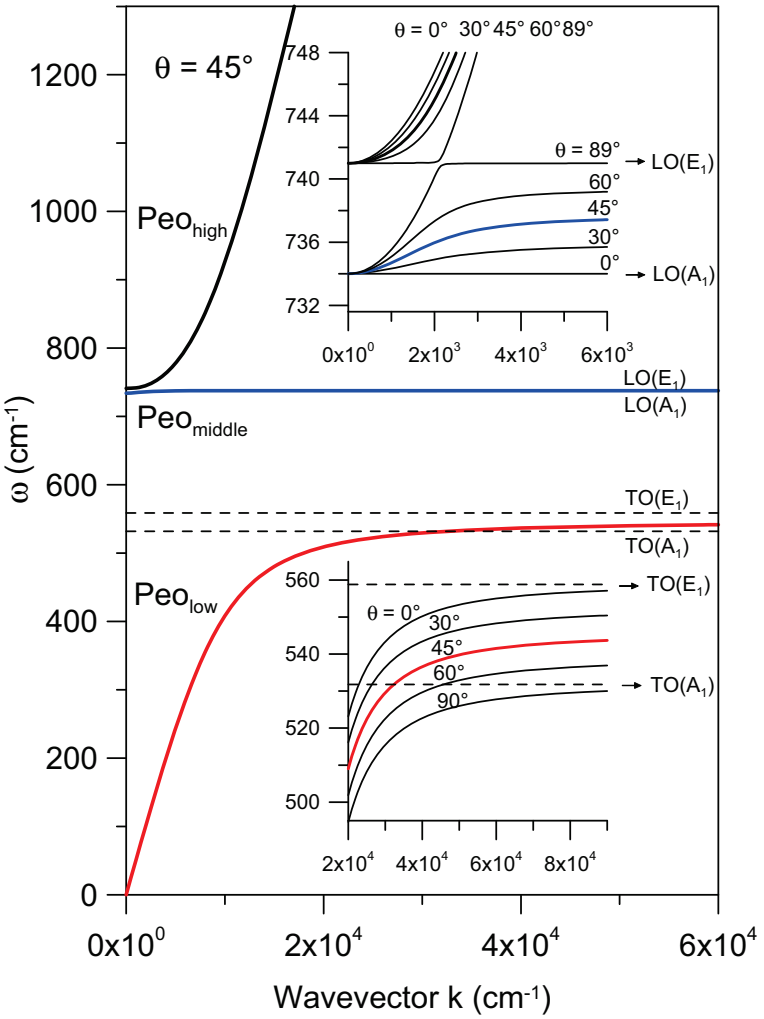

Fig. 7.2: Solutions of equation (3.19): Dispersion of the TO-phononlike Peo_{low}, the LO-phononlike $\text{Peo}_{\text{middle}}$ and the photon-like Peo_{high} extraordinary polariton branches in wz-GaN in dependence on the wavevector k for a fixed angle $\theta = 45°$ between the wavevector and the z axis. The insets show the dispersion of the extraordinary polariton branches for small wavevectors in dependence on the angle θ. Reprinted figure with permission from [68]. Copyright 2013 American Physical Society.

as well. For $k \to 0$, the polaritons are independent on the angle θ of the wavevector with the c axis and approach the limiting frequencies 0, $\omega_{\text{LO,A1}}$ and $\omega_{\text{LO,E1}}$. From a physical point of view, if the wavelength approaches infinity, then the lattice vibrations cease to sense the wavevector direction. The lattice displacements and associated electric fields are parallel or perpendicular to the c axis.

7.1.3 Raman scattering intensity of phonon polaritons in uniaxial crystals

In section 3.4 equation (3.38) was derived describing the Raman scattering intensity of phonons (180° backscattering, 90° scattering geometry or near-forward scattering) as well as phonon polaritons (near-forward scattering). The matrices $\tilde{R}_N$ where the

index N refers to the ordinary transverse polariton (N = To), extraordinary transverse polariton (N = Te), and extraordinary longitudinal polariton (N = Le) are given by equation (3.39)-(3.41). The matrix elements $|\langle 1+n_\omega|\, Q_N\, |n_\omega\rangle|^2$ in equation (3.38) have been calculated for polar modes in cubic crystals by Mills and Burstein [81] introducing a so called phonon strength function with electromagnetic and mechanical contributions to the polaritons energy. However, generalizing for uniaxial crystals, the calculation of the matrix elements using equation (3.32) leads to the following:

$$\begin{aligned}
|\langle 1+n_\omega|\, Q_{\mathsf{To}}\, |n_\omega\rangle|^2 &= \left[\frac{\hbar(1+n_\omega)}{2V\omega_{\mathsf{TO,E1}}}\right] S_{\mathsf{p,E1}}\,, \\
|\langle 1+n_\omega|\, Q_{\mathsf{Te}}\, |n_\omega\rangle|^2 &= \left[\frac{\hbar(1+n_\omega)}{2V}\right] \left(\frac{S_{\mathsf{p,E1}}}{\omega_{\mathsf{TO,E1}}}\cos^2\theta + \frac{S_{\mathsf{p,A1}}}{\omega_{\mathsf{TO,A1}}}\sin^2\theta\right), \\
|\langle 1+n_\omega|\, Q_{\mathsf{Le}}\, |n_\omega\rangle|^2 &= \left[\frac{\hbar(1+n_\omega)}{2V}\right] \left(\frac{S_{\mathsf{p,E1}}}{\omega_{\mathsf{TO,E1}}}\sin^2\theta + \frac{S_{\mathsf{p,A1}}}{\omega_{\mathsf{TO,A1}}}\cos^2\theta\right),
\end{aligned} \tag{7.1}$$

with

$$\begin{aligned}
S_{\mathsf{p,E1}}(\omega) &= \frac{\omega\omega_{\mathsf{TO,E1}}\left(\omega^2_{\mathsf{LO,E1}} - \omega^2_{\mathsf{TO,E1}}\right)}{\left(\omega^2_{\mathsf{TO,E1}} - \omega^2\right)^2 + \omega^2_{\mathsf{TO,E1}}\left(\omega^2_{\mathsf{LO,E1}} - \omega^2_{\mathsf{TO,E1}}\right)}, \\
S_{\mathsf{p,A1}}(\omega) &= \frac{\omega\omega_{\mathsf{TO,A1}}\left(\omega^2_{\mathsf{LO,A1}} - \omega^2_{\mathsf{TO,A1}}\right)}{\left(\omega^2_{\mathsf{TO,A1}} - \omega^2\right)^2 + \omega^2_{\mathsf{TO,A1}}\left(\omega^2_{\mathsf{LO,A1}} - \omega^2_{\mathsf{TO,A1}}\right)}.
\end{aligned} \tag{7.2}$$

The phonon strength functions $S_{\mathsf{p,E1}}(\omega)$ and $S_{\mathsf{p,A1}}(\omega)$ provide a measure of the phonon content of the polaritons depending on their frequency. If the frequencies of the transverse polaritons reach the phonon frequencies ($\omega \to \omega_{\mathsf{TO,E1}}$ and $\omega \to \omega_{\mathsf{TO,A1}}$) in case of large wavevectors, the phonon strength functions approach unity. As discussed in the last subsection for $\theta = 0°$ the extraordinary transverse polaritons have pure E_1 symmetry and for $\theta = 90°$ pure A_1 symmetry. Thus, the first two rows of equation (7.1) equal the matrix element in case of transverse phonons given by equation (3.42) in section 3.5.
For the longitudinal polaritons with $\omega \to \omega_{\mathsf{LO,E1}}$ and $\omega \to \omega_{\mathsf{LO,A1}}$, one obtains:

$$\begin{aligned}
S_{\mathsf{p,E1}} &= \frac{\omega_{\mathsf{TO,E1}}}{\omega_{\mathsf{LO,E1}}}, \\
S_{\mathsf{p,A1}} &= \frac{\omega_{\mathsf{TO,A1}}}{\omega_{\mathsf{LO,A1}}}.
\end{aligned} \tag{7.3}$$

In that case and assuming pure symmetry of the extraordinary longitudinal polaritons[2] the equality of the latter matrix element in equation (7.1) and the one in equation (3.42) is fulfilled.

[2] For $\theta = 0°$: pure A_1 symmetry and for $\theta = 90°$: pure E_1 symmetry

7.2 Experiment

7.2.1 Near-forward scattering

For uniaxial crystals the conventionally used experimental setup applying annular apertures with varying diameters in front of the entrance slit of the spectrometer is meaningful only if the incident laser beam in near-forward scattering geometry is directed parallel to the c axis of the crystal and the isotropic plane coincides with the aperture plane. However, also in this case the polaritons observed will depend on the angle and will be of mixed character.
To our knowledge only one investigation on a 70 μm thick hexagonal GaN bulk crystal measured with near-forward scattering parallel to the c axis and annular apertures is reported by Torii *et al.*[40]. However, in that work the dependence of the Raman scattering efficiency of the polaritons on the frequency was not studied and the polaritons observed were of mixed character.

In order to observe phonon polaritons with pure symmetry, a new method for near-forward scattering with a screen positioned in a plane before the first image lens which enables to open small rectangular windows in this plane was developed.
The scattering configuration is shown in figure 7.3. The exciting laser beam is directed along the x axis and enters the entrance surface of the prismatic sample. The screen placed directly in front of the entrance lens of the imaging system is open for scattered light with a small adjustable window around the point (Y, Z). The scattered light beam includes the angle ψ with the (x, y) plane, and its orthogonal projection on the (x, y) plane the angle δ with the x axis. Afterwards, the scattered light originating from the focus plane of the entrance lens passes an analyzer and a quartz waveplate which rotates the polarization axis in the position for which the spectrometer throughput is optimized. For the Stokes scattering process inside the crystal (see figure 7.3(b) and 7.3(c), index 'i') wavevector conservation requires according to equation (3.27):

$$\vec{k}_{\mathsf{iL}} = \vec{k}_{\mathsf{iS}} + \vec{k}_{\mathsf{P}}, \tag{7.4}$$

and according to equation (3.28) energy conservation requires:

$$\hbar\omega_{\mathsf{L}} = \hbar\omega_{\mathsf{S}} + \hbar\omega_{\mathsf{P}} \qquad \text{or} \qquad \frac{1}{\lambda_{\mathsf{L}}} = \frac{1}{\lambda_{\mathsf{S}}} + \omega. \tag{7.5}$$

The laser wavevector and its magnitude are given by:

$$\begin{aligned} \vec{k}_{\mathsf{iL}} &= \frac{2\pi\, n_{\mathsf{L}}}{\lambda_{\mathsf{L}}}\,(1,0,0)\,, \\ \left|\vec{k}_{\mathsf{iL}}\right| &= \frac{2\pi\, n_{\mathsf{L}}}{\lambda_{\mathsf{L}}}, \end{aligned} \tag{7.6}$$

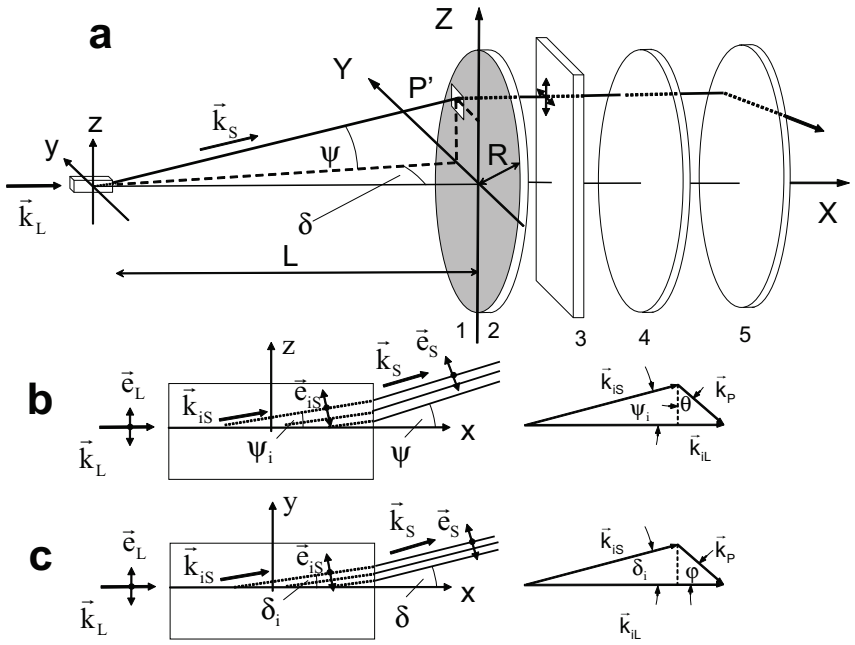

Fig. 7.3: Setup for near-forward Raman scattering taken from [68]. (Copyright 2013 American Physical Society.)
(a) Scattered light with wavevector $\vec{k}_S$ outside the crystal enters the window P' at (Y, Z) on the masking screen (1) positioned in front of the lens (2), passes the analyzer (3), $\lambda/2$ quartz waveplate (4) and lens (5). Introducing spherical coordinates the scattered light beam includes the angle ψ with the (x, y) plane and the azimuthal angle δ.
Refraction at the crystal boundary:
(b) Special case: scattering in the (x, z) plane. The wavevector $\vec{k}_S$ of the scattered light (angle ψ with the x axis) corresponds to the wavevector $\vec{k}_{iS}$ with the angle ψ_i inside the crystal.
(c) Special case: scattering in the (x, y) plane. The wavevector $\vec{k}_S$ of the scattered light (angle δ with the x axis) corresponds to the wavevector $\vec{k}_{iS}$ with the angle δ_i inside the crystal.

where λ_L denotes the wavelength of the incident light outside the crystal. Wavevector and magnitude of the scattered light are written as:

$$\begin{aligned} \vec{k}_{iS} &= \frac{2\pi\, n_S}{\lambda_S} \left(\cos\psi_i \cdot \cos\delta_i, \cos\psi_i \cdot \sin\delta_i, \sin\psi_i\right), \\ \left|\vec{k}_{iS}\right| &= \frac{2\pi\, n_S}{\lambda_S}, \end{aligned} \tag{7.7}$$

where λ_S indicates the wavelength of the scattered light outside the crystal. In equations (7.4) and (7.5), $\vec{k}_P$ refers to the wavevector of the polariton excited in a Stokes process and ω to its energy. For small scattering angles and $\left|\vec{k}_{iL}\right| \approx \left|\vec{k}_{iS}\right|$, it can be assumed that $\vec{k}_P \perp \vec{k}_{iL}$. In the case of very small scattering angles, also components of the transferred polariton wavevector in the (x, y) plane have to be considered. With equations (7.4)-(7.7), the polariton wavevector can be expressed as:

$$\vec{k}_P = \frac{2\pi\, n_S(1-\omega\lambda_L)}{\lambda_L} \left(\frac{n_L}{n_S}\frac{1}{1-\omega\lambda_L} - \cos\psi_i \cdot \cos\delta_i, -\cos\psi_i \cdot \sin\delta_i, -\sin\psi_i\right). \tag{7.8}$$

The magnitude of the polariton wavevector is

$$k_{\mathsf{P}} = 2\pi \sqrt{\frac{1}{\lambda_{\mathsf{L}}^2}\left(n_{\mathsf{L}}^2 + n_{\mathsf{S}}^2\right) - n_{\mathsf{S}}^2 \omega \left(\frac{2}{\lambda_{\mathsf{L}}} - \omega\right) - 2 n_{\mathsf{L}} n_{\mathsf{S}} \frac{1}{\lambda_{\mathsf{L}}} \left(\frac{1}{\lambda_{\mathsf{L}}} - \omega\right) \cos\psi_{\mathsf{i}} \cdot \cos\delta_{\mathsf{i}}}. \quad (7.9)$$

In this equation, k_{P} is obtained in cm^{-1} if λ_{L} is expressed in cm and the Raman shift ω in cm^{-1}.

The angle θ between the polariton wavevector $\vec{k}_{\mathsf{P}}$ and the z axis (see figure 7.3(b)) is defined by:

$$\cos\theta = \frac{k_{\mathsf{P},z}}{k_{\mathsf{P}}} = \frac{-2\pi\, n_{\mathsf{S}}\,(1 - \omega\lambda_{\mathsf{L}})\sin\psi_{\mathsf{i}}}{\lambda_{\mathsf{L}}\, k_{\mathsf{P}}} \quad (7.10)$$

The angle φ between the polariton wavevector and the x axis (see figure 7.3(c)) is determined by:

$$\sin\varphi = \frac{k_{\mathsf{P},y}}{\sqrt{k_{\mathsf{P}}^2 - k_{\mathsf{P},z}^2}} \quad (7.11)$$

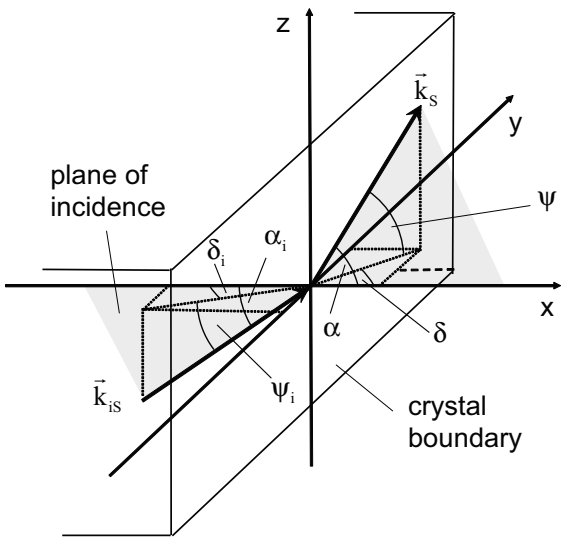

Fig. 7.4: Refraction of the scattered light at the crystal boundary. Suitably, the angles α and α_{i} between the unit wavevector of the scattered light (outside and inside the crystal) and the x axis are introduced in order to derive the unit wavevector of the scattered light inside the crystal in dependence on the angles ψ and δ using the law of refraction. Reprinted figure with permission from [68]. Copyright 2013 American Physical Society.

Since wz-GaN is a uniaxial crystal, one has to differentiate between ordinary and extraordinary rays of the incident and scattered light. The refraction indices n_{L} and n_{S} are used for ordinary (extraordinary) rays. For ordinary rays the electric field is polarized in the (x, y) plane. The proper refractive index is $n_{\mathsf{o}} = \sqrt{\varepsilon_{\infty\perp}}$. For extraordinary rays the electric field is polarized parallel to the z axis and the corresponding

refractive index can be expressed by $n_{\mathsf{eo}} = \sqrt{\varepsilon_{\infty\parallel}}$. $\varepsilon_{\infty\perp}$ indicates the high-frequency dielectric constant in the (x, y) plane and $\varepsilon_{\infty\parallel}$ for directions parallel to the z axis (see section 3.2).
In the following near-forward scattering with the c axis of the crystal oriented parallel to the Z axis of the laboratory coordinate system and the scattering geometries $x(zz)x$, $x(zy)x$, $x(yz)x$, and $x(yy)x$ given with respect to Porto's notation (see section 3.5) are considered.
It is assumed that the distance L of the imaging lens and the lens radius R are large in comparison with the lateral size of the crystal and the exciting laser path length within the crystal (see figure 7.3(a)). Furthermore, R should be small in comparison with L. In our case L = 80 mm and R = 14 mm. Light scattered inside the crystal with wavevector $\vec{k}_{\mathsf{iS}}$ enters the small window P′ on the screen located at $(Y, Z) = (L\tan\delta, L\tan\psi)$ with wavevector $\vec{k}_{\mathsf{S}}$. The vectors $\vec{k}_{\mathsf{iS}}$, $\vec{k}_{\mathsf{P}}$, and $\vec{e}_{\mathsf{iS}}$ characterizing the scattering process inside the crystal can be expressed as functions of the window position (angles ψ and δ).
It is appropriate to introduce spherical coordinates

$$\begin{aligned} x &= r \cdot \cos\psi \cdot \cos\delta, \\ y &= r \cdot \cos\psi \cdot \sin\delta, \\ z &= r \cdot \sin\psi. \end{aligned}$$

Thus, the unit vector $\vec{q}_{\mathsf{S}}(\psi,\delta) = \vec{k}_{\mathsf{S}}(\psi,\delta) \,/\, \left|\vec{k}_{\mathsf{S}}(\psi,\delta)\right|$ of the scattered light beam outside the crystal can be expressed as:

$$\vec{q}_{\mathsf{S}}(\psi,\delta) = (\cos\psi\cdot\cos\delta, \cos\psi\cdot\sin\delta, \sin\psi)\,, \tag{7.12}$$

where ψ denotes the angle between the scattered light vector and the (x, y) plane, and δ the azimuthal angle between the orthogonal projection of the scattered light vector on the (x, y) plane and the x axis (figure 7.4). The lens center is located at $\psi = \delta = 0°$, an adjustable rectangular window in the aperture in front of lens 1 can be described by:

$$\Delta Y \cdot \Delta Z = \frac{\Delta\psi\cdot\Delta\delta\cdot L^2}{(\cos^2\psi\cdot\cos^2\delta)} \approx \Delta\psi\cdot\Delta\delta\cdot L^2. \tag{7.13}$$

Further, the direction of the x axis is oriented perpendicularly to the boundary surface of the crystal. The x axis as well as the scattered light vectors inside and outside the crystal are located in the plane of incidence (see figure 7.4). It is convenient to introduce the angles of the unit vectors of the scattered light beams outside ($\vec{q}_{\mathsf{S}}$) and inside the crystal ($\vec{q}_{\mathsf{iS}}$) with the axis x, y, and z:

$$\vec{q}_{\mathsf{S}} = (q_{\mathsf{S},x}, q_{\mathsf{S},y}, q_{\mathsf{S},z}) = (\cos\alpha, \cos\beta, \cos\gamma)\,, \tag{7.14}$$

$$\vec{q}_{\mathsf{iS}} = (q_{\mathsf{iS},x}, q_{\mathsf{iS},y}, q_{\mathsf{iS},z}) = (\cos\alpha_{\mathsf{i}}, \cos\beta_{\mathsf{i}}, \cos\gamma_{\mathsf{i}})\,. \tag{7.15}$$

Using the law of refraction $\sin\alpha_\mathsf{i} = \sin\alpha/n_\mathsf{S}$ one receives the wavevector (unit vector) of the scattered light inside the crystal in dependence on the angles ψ and δ:

$$\vec{q}_{\mathsf{iS}} = \left(\sqrt{1-a}, \frac{-\sqrt{a}}{\sqrt{1+b}}, \frac{\sqrt{ab}}{\sqrt{1+b}} \right), \tag{7.16}$$

where $a = \left(1 - \cos^2\psi \cdot \cos^2\delta\right)/n_\mathsf{S}^2$ and $b = \tan^2\psi/\sin^2\delta$. Depending on the polarization, the refractive index rates as $n_\mathsf{S} = n_\mathsf{o}$ (ordinary ray) or $n_\mathsf{S} = n_\mathsf{eo}$ (extraordinary ray). It should be noted that equation (7.16) holds for the ordinary ray, but is not valid for the extraordinary ray in all cases. If the plane of incidence does not coincide with the principal plane (defined as a plane containing the wavevector and the z axis), the refracted extraordinary ray no longer lies in the plane of incidence [147, 148]. Further, its refractive index depends on the angle ψ. However, in our case the angles between the scattered light beam and the x axis inside the crystal are small (the largest possible angles are about 4° for scattered light entering the border of the imaging lens), and the difference between the two refraction indices n_o and n_eo is only small in the case of wz-GaN. Therefore, it is justified to use equation (7.16) for the extraordinary ray as well. The transferred polariton wavevector $\vec{k}_\mathsf{P}$ in dependence on the angles ψ and δ is obtained using equation (7.4):

$$\vec{k}_\mathsf{P}(\psi,\delta) = 2\pi \left[\frac{n_\mathsf{L}\,\vec{q}_{\mathsf{iL}}}{\lambda_\mathsf{L}} - \frac{n_\mathsf{S}\,\vec{q}_{\mathsf{iS}}(\psi,\delta)}{\lambda_\mathsf{S}} \right]. \tag{7.17}$$

For the polarization configuration (yz) the component $k_{\mathsf{P},x}$ can also be negative (see figure 7.5).

The exciting laser beam is directed parallel to the x axis and penetrates the crystal surface perpendicularly without refraction and change of the polarization. For the measurements the following polarizations of the electric field were used: The letters V(H) indicate vertical (horizontal) polarization. As already previously mentioned, the index 'i' refers to the inner part of the crystal. The polarization vectors perpendicular to the wavevector of the incident laser beam are $\vec{e}^{\,\mathsf{H}}_\mathsf{L}(\vec{e}^{\,\mathsf{H}}_{\mathsf{iL}})$ with horizontal direction parallel to the y axis and $\vec{e}^{\,\mathsf{V}}_\mathsf{L}(\vec{e}^{\,\mathsf{V}}_{\mathsf{iL}})$ with vertical direction parallel to the z axis of the laboratory coordinate system:

$$\begin{aligned} \vec{e}^{\,\mathsf{H}}_\mathsf{L} &= \vec{e}^{\,\mathsf{H}}_{\mathsf{iL}} = (0,1,0)\,, \\ \vec{e}^{\,\mathsf{V}}_\mathsf{L} &= \vec{e}^{\,\mathsf{V}}_{\mathsf{iL}} = (0,0,1)\,. \end{aligned} \tag{7.18}$$

A beam of scattered light reaches the window on the screen positioned at $(Y,Z) = (L\tan\delta, L\tan\psi)$ in front of the entrance lens of the imaging system and then passes the analyzer with vertical (V) or horizontal (H) position parallel to the x axis. The light beam arises from the scattered light leaving the crystal face with a wavevector given by equation (7.16) and characterized by the two angles ψ and δ. The direction of the beams wavevector inside the crystal is determined by the refraction law relating to the

crystal surface. The polarization vectors of the beam between the crystal and lens 1 are

$$\begin{aligned} \vec{e}_{\mathsf{S}}^{\,\mathsf{H}} &= (-\sin\delta, \cos\delta, 0)\,, \\ \vec{e}_{\mathsf{S}}^{\,\mathsf{V}} &= (-\sin\psi, 0, \cos\psi)\,. \end{aligned} \tag{7.19}$$

The polarization vectors of the corresponding scattered beam inside the crystal are

$$\begin{aligned} \vec{e}_{\mathsf{iS}}^{\,\mathsf{H}} &= \frac{\vec{q}_{\mathsf{iS}} \times \vec{e}_z}{|\vec{q}_{\mathsf{iS}} \times \vec{e}_z|} = \frac{1}{\sqrt{q_{\mathsf{iS},x}^2 + q_{\mathsf{iS},y}^2}} \left(q_{\mathsf{iS},y}, -q_{\mathsf{iS},x}, 0\right), \\ \vec{e}_{\mathsf{iS}}^{\,\mathsf{V}} &= \vec{e}_{\mathsf{iS}}^{\,\mathsf{H}} \times \vec{q}_{\mathsf{iS}} = \frac{\left(-q_{\mathsf{iS},x} \cdot q_{\mathsf{iS},z}, -q_{\mathsf{iS},y} \cdot q_{\mathsf{iS},z}, q_{\mathsf{iS},x}^2 + q_{\mathsf{iS},y}^2\right)}{\sqrt{q_{\mathsf{iS},x}^2 + q_{\mathsf{iS},y}^2}}. \end{aligned} \tag{7.20}$$

The polarization vectors can be expressed as functions of ψ and δ using equation (7.16).

7.2.2 Experimental conditions

Raman spectra were obtained at room temperature using a T 64000 Raman spectrometer (Horiba, Jobin Yvon) in a nearly forward scattering geometry. For this purpose, the GaN sample was positioned in the macro chamber with its c axis oriented parallel to the z axis of the laboratory coordinate system. The spectra were excited applying the 514.5 nm line of an Ar^+ laser at a power level of about 100 mW at the sample. After passing the spectrometer equipped with gratings of 1800 grooves/mm in subtractive mode, the scattered light was detected by a LN cooled CCD detector. The laser beam was focused onto the sample by a laser objective. By means of a polarization rotator the laser beam polarization could be changed from (i) parallel to the y axis (H) with the ordinary ray inside the crystal to (ii) parallel to the z axis (V) with extraordinary ray inside the crystal (see figure 7.3). The scattered light was analyzed with polarization parallel or perpendicular to the z axis using an analyzer positioned in the parallel light path between sample and entrance slit of the spectrometer. Both laser beam and sample were carefully adjusted in order to avoid the capture of laser light into the spectrometer. The laser beam leaving the sample was masked in the center of the entrance lens of the imaging system. Furthermore, care is necessary to avoid gathering of scattered light excited by the laser beam partly backscattered at the inner crystal surface. The reflectivity at 514.5 nm wavelength is about 0.174 (0.157) for the ordinary (extraordinary) beam [103].

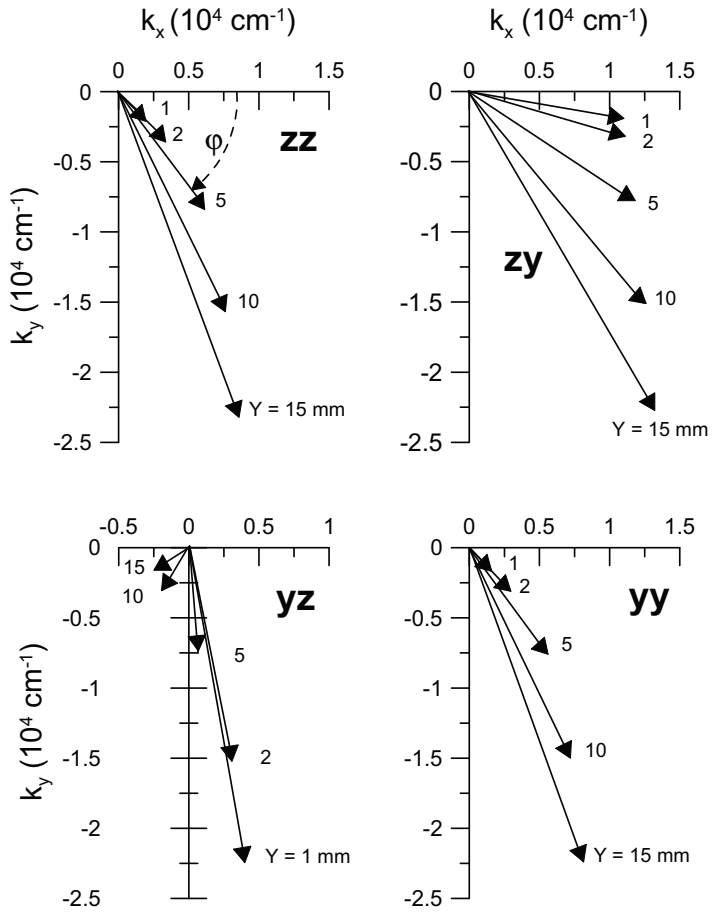

Fig. 7.5: Polariton wavevectors for near-forward scattering in direction x in the (x, y) plane. The wavevector of the scattered light is directed to the window P′ at Y (and for $Z = 0$) on the masking screen (see figure 7.3(a)). The two letters indicate the polarization direction of the incident and scattered light, respectively. Reprinted figure with permission from [68]. Copyright 2013 American Physical Society.

7.3 Results and discussion

Although the birefringence of wz-GaN is only weak ($n_o = \sqrt{\varepsilon_{\infty\perp}} = 2.280, n_e = \sqrt{\varepsilon_{\infty\parallel}} = 2.304$ [71]), its optical anisotropy has a strong impact on the polariton spectra measured with different polarizations of the incident and scattered light. Figure 7.5 shows transferred polariton wavevectors for scattering in the (x, y) plane for the near-forward scattering configurations $x(yy)x$, $x(zz)x$, $x(zy)x$, and $x(yz)x$. The parameter Y describes the position of the opened window in horizontal direction ($Z = 0$) on the screen in front of the entrance lens. Note the strong difference between the polarizations (zy) and (yz) for hexagonal wz-GaN. In the case of cubic β-GaN, however, the polariton wavevectors and the Raman spectra of the two polarizations should be the same. The ordinary ($\vec{e}_\mathrm{L} \parallel y$) or extraordinary ($\vec{e}_\mathrm{L} \parallel z$) laser light propagates inside the crystal along the x axis. The outgoing scattered light is extraordinary ($\vec{e}_\mathrm{S} \parallel z$) or ordinary ($\vec{e}_\mathrm{S} \parallel y$). The extraordinary polaritons are observable with (zz) or (yy)

polarizations, whereas the ordinary ones can be detected in (zy) or (yz) polarization configuration.

The subfigures (a) and (b) of the figures 7.6 - 7.9 show the near-forward Raman scattering spectra and the dispersion of the phonon polaritons in dependence on the polariton wavevector for scattering in the (x, y) plane ($\theta = 90°$). The intensities of the Raman spectra were normalized with respect to the intensity of the $E_{2,high}$ Raman mode at 567.6 cm^{-1} which is allowed in the configuration $x(yy)x$. This nonpolar phonon is connected with lattice displacements parallel to the (x, y) plane and is not influenced by the electric field. Its intensity does not depend on the parameter Y displayed in the figures 7.6 - 7.9. The Raman bands of the phonon polaritons are shifted towards lower frequencies with decreasing parameter Y. The smaller the value of Y the smaller the angle δ_i between the scattered light beam and the x axis (see figure 7.3(c)) and thus the smaller the magnitude of the transferred polariton wavevector (see figure 7.5). Values of $Y \approx 2$ mm could be realized. This corresponds to an angle $\delta_i \approx 0.5°$. The exciting laser beam passing the crystal was blocked off in the centre of the screen in order to avoid entrance of laser light in the spectrometer. The overlay of the scattered light with exciting laser light limits the parameter Y at small values.

Besides the phonon polariton Raman bands small Raman bands at fixed frequencies can be observed, in the Raman spectra of the extraordinary polaritons the TO(A_1) phonons at 531.1 cm^{-1} and in the Raman spectra of the ordinary polaritons the TO(E_1) phonon at 558.9 cm^{-1} as well as weak bands of the (very strong) $E_{2,high}$ phonon. Their origin is due to some scattered light which stems from a 180° backscattering process of phonons with wavevectors of about 6×10^5 cm^{-1} overlaying the near-forward scattering. Part of the incident laser beam is reflected inside the crystal and gives rise to these weak bands which could be minimized by careful adjustment. Figures 7.6(a) - 7.9(a) show insets with the measured LO phonons with symmetry E_1 and location at about 741 cm^{-1} in accordance with scattering in the (x, y) plane. The stable position of the measured LO phonon indicates that the scattering occurs in the (x, y) plane ($\theta = 90°$).

The dispersion of the polariton modes is shown in figures 7.6(b) - 7.9(b). The curves $PO_{eo,low}$, $PO_{eo,middle}$, and $PO_{eo,high}$ in figure 7.6(b) and figure 7.7(b) for the extraordinary polariton modes are solutions of equation (3.19) and the curves $PO_{o,low}$ and $PO_{o,high}$ in figure 7.8(b) and figure 7.9(b) are solutions of equation (3.16). The dashed curves show solutions of equations (7.4) and (7.5) for scattering angles δ_i inside the crystal, with combinations of values (ω) and (k_P), allowed due to energy and momentum conservation. The intersections with the theoretical dispersion curves yield the allowed polaritons.

The smaller the angle δ_i the broader the Raman bands since the slope of the curve becomes steeper. The small bands at 317 cm^{-1}, 410 cm^{-1}, and 420 cm^{-1} are

acoustic overtones of the second-order Raman spectra [149]. The dashed curves in figure 7.9(b) illustrate that only the configuration $x(yz)x$ allows one to observe photonlike polaritons on the branch $PO_{o,high}$ in principle. However, for this scattering configuration the scattering intensity is more than one order smaller than for the other configurations. Further, the slope of this branch rises steeply with increasing δ_i which increases the halfwidth of the expected band. Therefore, despite careful search this branch could not be detected. Figure 7.10 shows Raman spectra of the extraordinary polariton with near-forward scattering in the (x, z) plane. The parameter Z indicates the position on the screen in vertical direction ($Y = 0$). Figure 7.10(a) displays spectra with polarization (zz) and figure 7.10(b) with polarization (yy) of the electric field vectors of the incident and scattered light. The intensities of the Raman spectra were normalized with respect to the intensity of the nonpolar $E_{2,high}$ phonon. The intensity of the $E_{2,high}$ phonon is (nearly) independent on the parameter Z in the considered Z range. Depending on the parameter Z, the transferred polariton wavevectors include different angles θ with the z axis (see figure 7.3(b)). Each Raman spectrum corresponds to different dispersion curves (see figure 7.2). Therefore, the corresponding dispersion curves were omitted.

The circles in figures 7.6(c) - 7.8(c) give the Raman scattering intensities of the polariton spectra shown in figures 7.6(a) - 7.8(a) for scattering in the (x, y) plane ($\theta = 90°$). The spectra were recorded with different polarizations which filter out the contributions of the Raman tensor elements a, b, and c, respectively. The phonon polaritons in the (yz) polarization exhibit only weak scattering intensities. Therefore, they were not analyzed. The intensities shown are the areas beneath the polariton bands normalized with respect to the $E_{2,high}$ Raman mode which is allowed in the (yy) polarization. In order to calculate the Raman intensity of phonon polaritons equations (3.38)-(3.41) were used. For this purpose, the positive as well as the negative solutions of the Faust-Henry coefficients obtained in section 6.3.5 were considered. The expressions for the matrix element in equation (3.38) in case of phonon polaritons were derived in section 7.1.3. In figures 7.6(c), 7.7(c), and 7.8(c) the measured intensities as function of the frequency (full circles) are compared with calculated intensities for both solutions of the Faust-Henry coefficients connected with the corresponding Raman tensor elements (solid lines). The comparison excludes the solutions with the positive sign of the coefficients. Based on the measurements of TO phonon polaritons with near-forward scattering, the three Faust-Henry coefficients in wz-GaN are therefore C_a^{FH} = -3.46, C_b^{FH} = -3.81, and C_c^{FH} = -2.31.

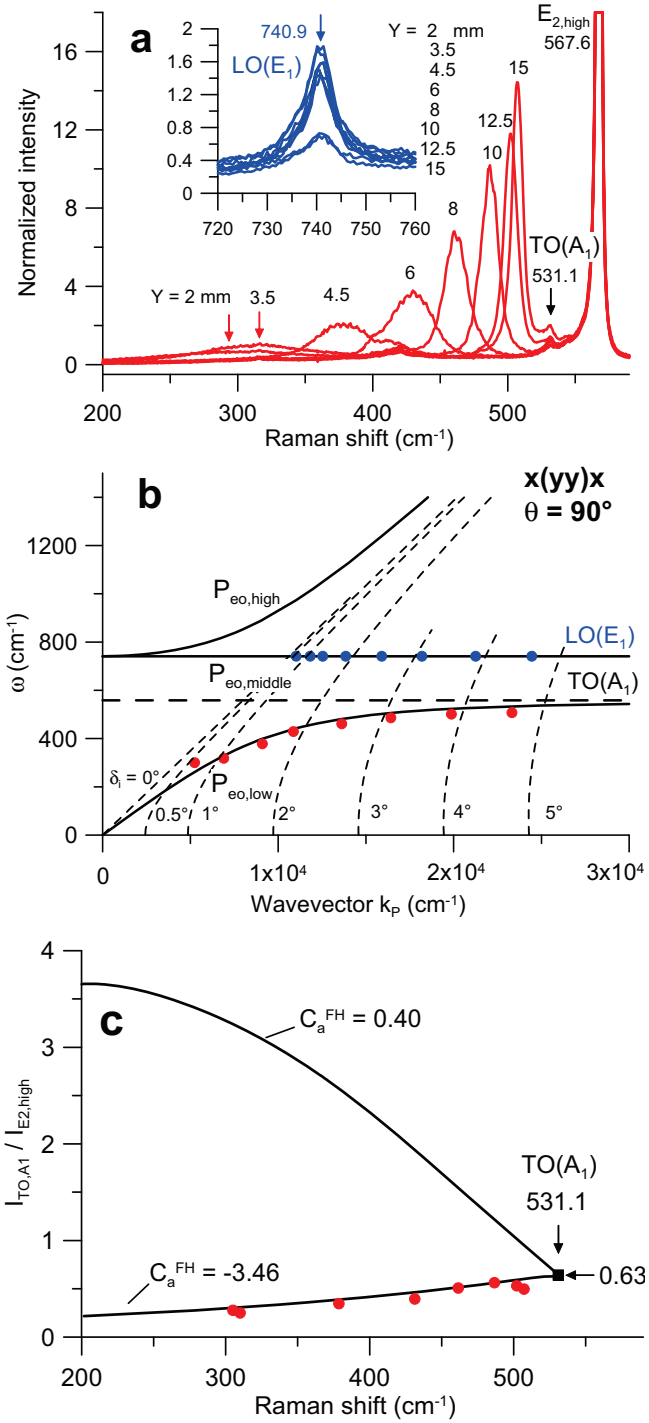

Fig. 7.6: (a) Raman spectra of the extraordinary polariton, $\theta = 90°$, $x(yy)x$. Near-forward scattering in direction x, scattering in the (x, y) plane, polarization parallel $y(y)$ of the incident (scattered) light vectors. The parameter Y indicates the position of the entrance window P′ for the scattered light on the screen (1), $Z = 0$. The inset shows the LO(E_1) phonon at fixed spectral position.
(b) Dispersion of the extraordinary polariton branches for $\theta = 90°$ in dependence on the polariton wavevector (solutions of equation (3.19)). The dashed curves (solutions of equation (7.9)) show possible $(\omega, \vec{k}_P)$ values for scattering angles δ_i inside the crystal (see figure 7.3).
(c) Polariton Raman efficiency as function of the frequency (full circles). The solid lines indicate calculations using the previously determined Faust-Henry coefficients C_a^{FH}. For $\omega \to \omega_{TO,A1}$ (large k_{Ph}) the branches reach the relative Raman cross section connected with a_{TO}.

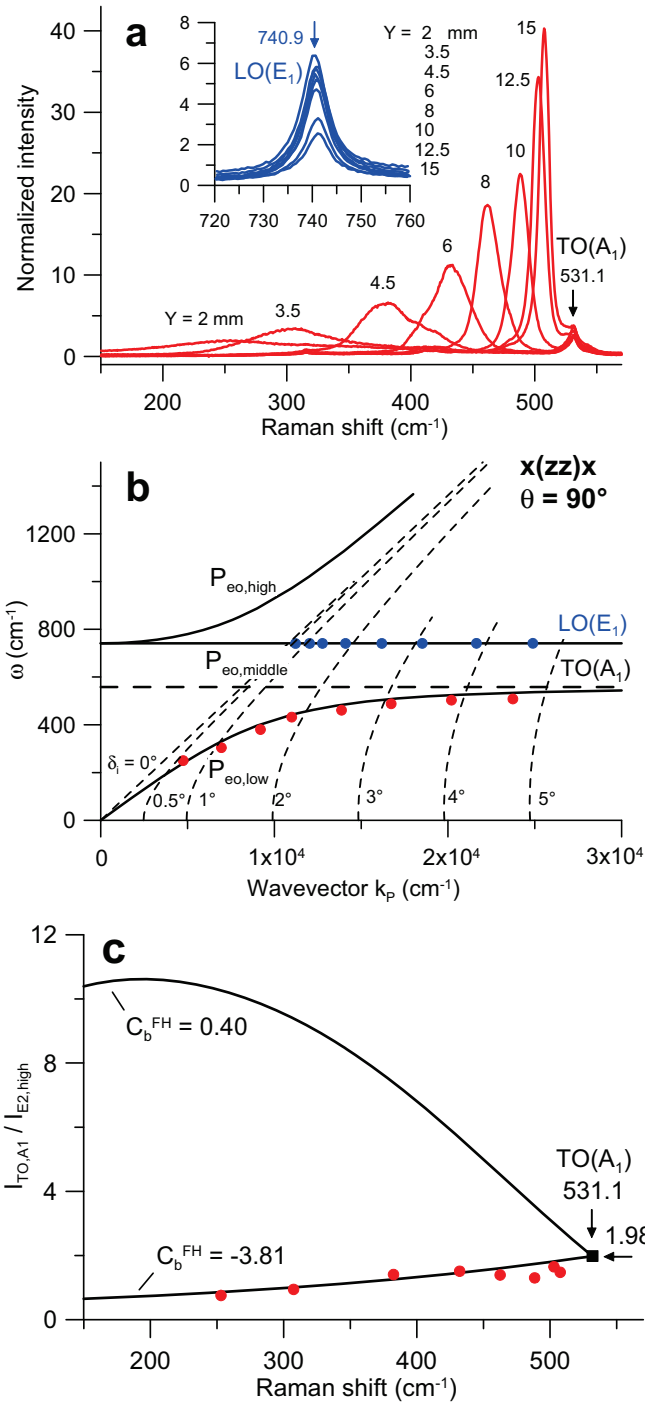

Fig. 7.7: (a) Raman spectra of the extraordinary polariton, $\theta = 90°$, $x(zz)x$. Near-forward scattering in direction x, scattering in the (x, y) plane, polarization parallel $z(z)$ of the incident (scattered) light vectors. The parameter Y indicates the position of the entrance window P′ for the scattered light on the screen (1), $Z = 0$. The inset shows the LO(E_1) phonon at fixed spectral position.
(b) Dispersion of the extraordinary polariton branches for $\theta = 90°$ in dependence on the polariton wavevector (solutions of equation (3.19)). The dashed curves (solutions of equations (7.9)) show possible (ω, k_P) values for scattering angles δ_i inside the crystal (see figure 7.3).
(c) Polariton Raman efficiency as function of the frequency (full circles). The solid lines indicate calculations using the previously determined Faust-Henry coefficients C_b^{FH}. For $\omega \to \omega_{TO,A1}$ (large k_{Ph}) the square refers to the relative Raman cross section connected with b_{TO}.

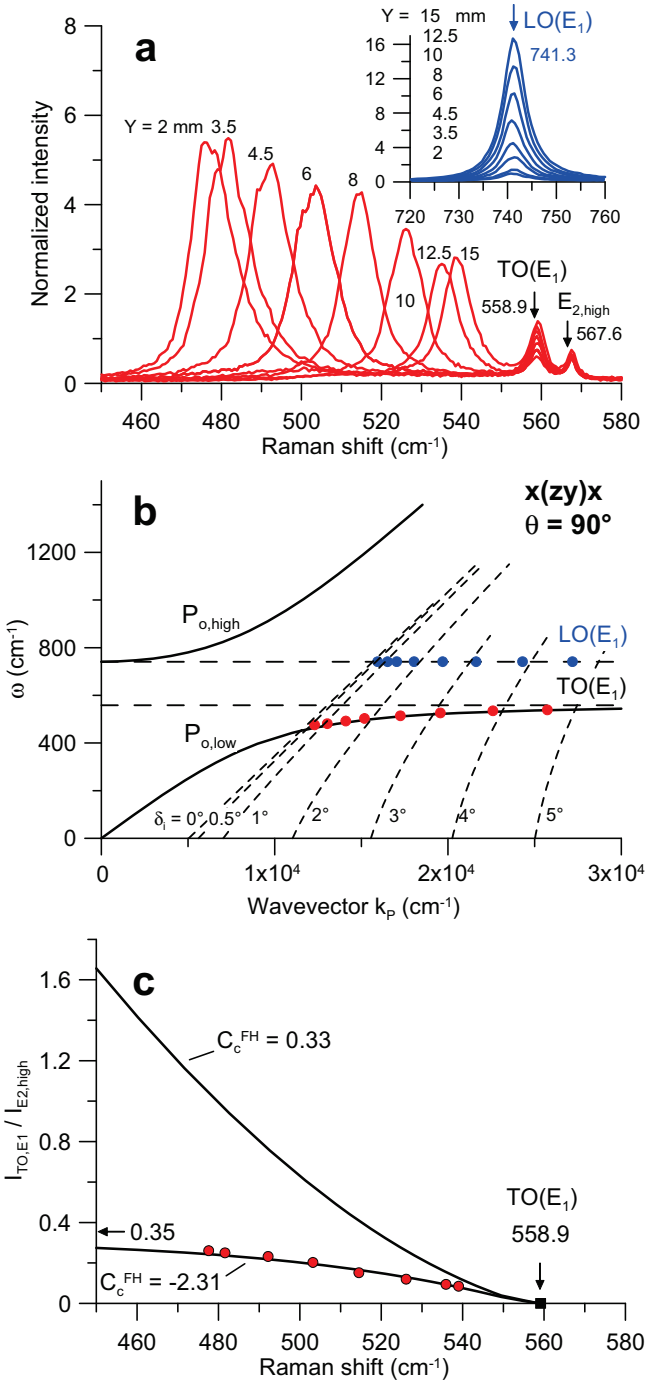

Fig. 7.8: (a) Raman spectra of the ordinary polariton, $\theta = 90°$, $x(zy)x$. Near-forward scattering in direction x, scattering in the (x, y) plane, polarization parallel $z(y)$ of the incident (scattered) light vectors. The parameter Y indicates the position of the entrance window P′ for the scattered light on the screen (1), $Z = 0$. The inset shows the LO(E_1) phonon at fixed spectral position.
(b) Dispersion of the ordinary polariton branches for $\theta = 90°$ in dependence on the polariton wavevector (solutions of equation (3.16)). The dashed curves (solutions of equation (7.9)) show possible $(\omega, \vec{k}_P)$ values for scattering angles δ_i inside the crystal (see figure 7.3).
(c) Polariton Raman efficiency as function of the frequency (full circles). The solid lines indicate calculations using the previously determined Faust-Henry coefficients C_c^{FH}. In the limit $\delta_i \to 0$ the low branch converges to the relative Raman cross section connected with c_{TO}.

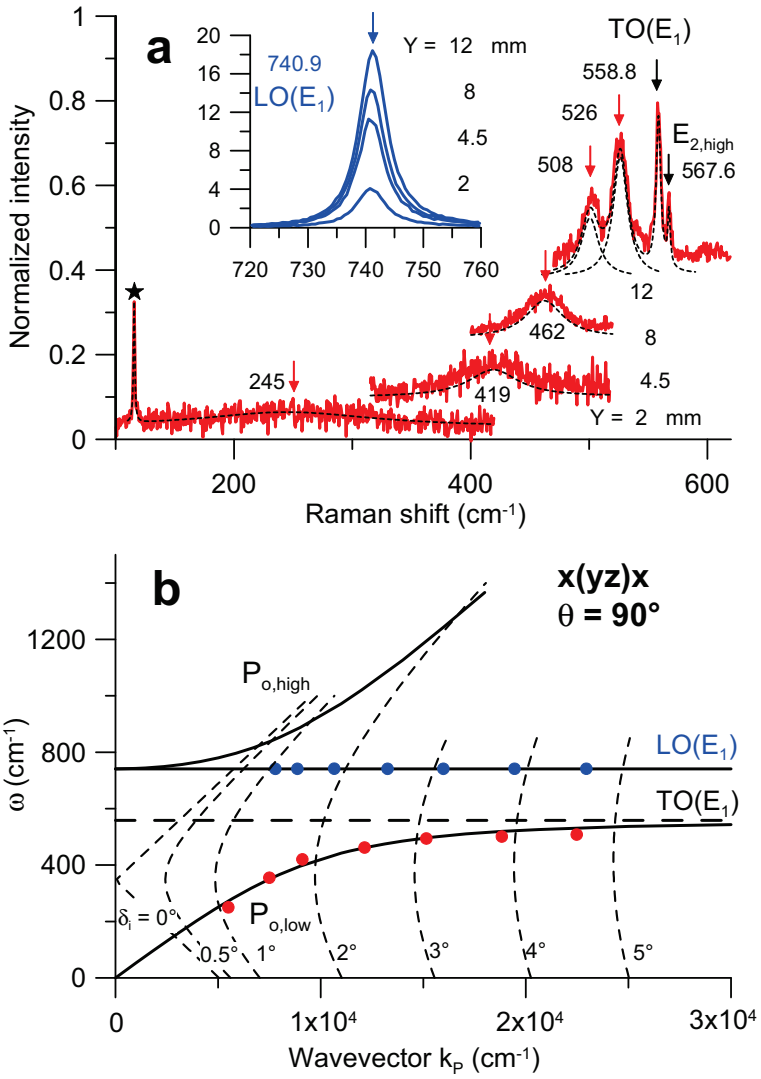

Fig. 7.9: (a) Raman spectra of the ordinary polariton, $\theta = 90°$, $x(yz)x$. Near-forward scattering in direction x, scattering in the (x, y) plane, polarization parallel $y(z)$ of the incident (scattered) light vectors. The parameter Y indicates the position of the entrance window P′ for the scattered light on the screen (1), $Z = 0$. The inset shows the LO(E_1) phonon at fixed spectral position.
(b) Dispersion of the ordinary polariton branches for $\theta = 90°$ in dependence on the polariton wavevector (solutions of equation (3.16)). The dashed curves (solutions of equation (7.9)) show possible $(\omega, \vec{k}_P)$ values for scattering angles δ_i inside the crystal (see figure 7.3).
Reprinted figure with permission from [68]. Copyright 2013 American Physical Society.

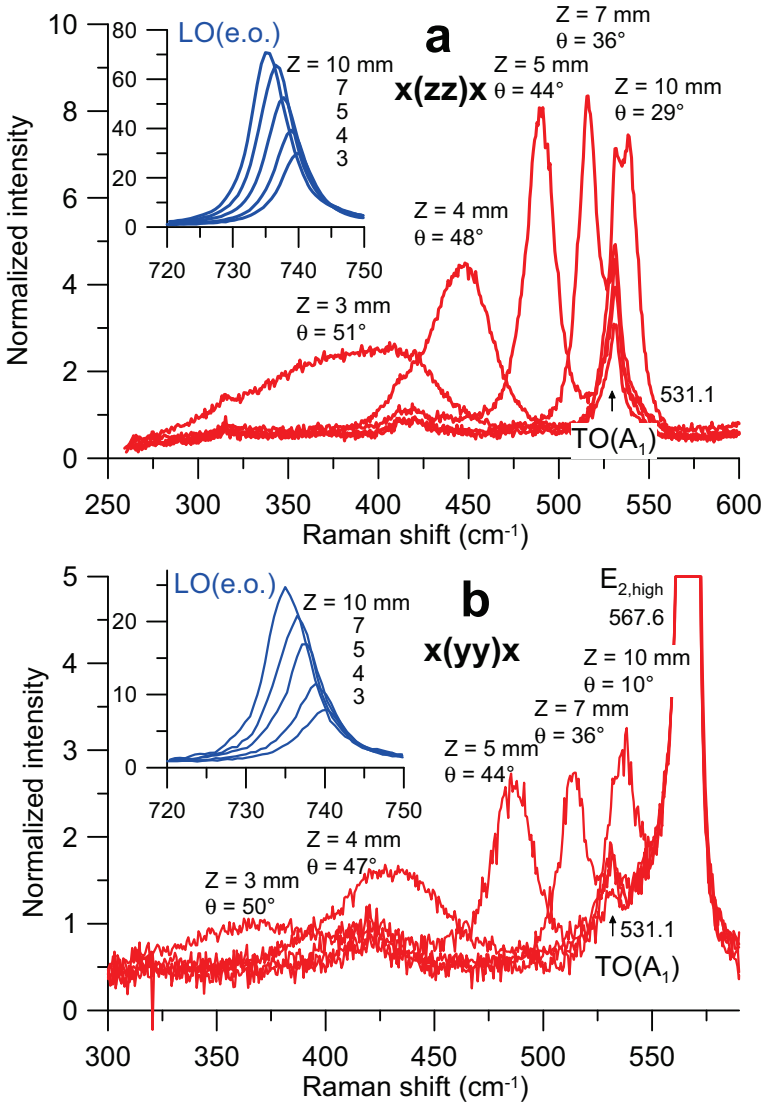

Fig. 7.10: Raman spectra of the extraordinary polariton, near-forward scattering in the (x, z) plane. The parameter Z indicates the position of the entrance window P′ for the scattered light on the screen (1), $Y = 0$. θ is the corresponding angle between the polariton wavevector and the z axis. The two insets show that the position of the LO phonon is shifted owing to the variation of θ (see figure 3.3). The upper panel shows the spectra taken with polarization $z(z)$ of the electric field vector of the incident (scattered) light, the spectra in the lower panel are measured with polarization $y(y)$. Reprinted figure with permission from [68]. Copyright 2013 American Physical Society.

7.4 Conclusion

In this chapter, Raman scattering of phonon polaritons in uniaxial crystals of wurtzite-type was investigated. The dispersion and the Raman scattering efficiency of the ordinary and extraordinary polaritons were discussed in detail. Expressions for the Raman scattering intensity were derived for arbitrary directions of the polaritons in the crystal. In the limit of large wavevector magnitudes, the equations describe the behavior of the polar phonons.

A novel experimental setup was developed using a rectangular window in front of the entrance lens. This setup enables measurements of phonon polaritons of defined E_1 and A_1 symmetry depending on their wavevector. Near-forward Raman scattering measurements with angles between laser beam and scattered light beam down to about 0.5° were possible.

Polariton spectra of wz-GaN were measured for different scattering geometries and polarizations. The experimental results are in accordance with the theoretical derivations.

Although the birefringence for light in the optical range is only small, strong differences between the polariton Raman spectra in the near-forward configurations $x(zy)x$ and $x(yz)x$ occur. The observation of the photonlike polariton branch should be possible, in principle, in the $x(yz)x$ configuration but escaped detection due to weak Raman signals.

Analyzing the Raman scattering efficiency of TO phonon polaritons enables to assign one solution of the Faust-Henry coefficients unambiguously. Based on the experimentally determined intensities of the phonon polaritons and the comparison of these values with calculated ones, the three Faust-Henry coefficients in wz-GaN are $C_a^{\mathrm{FH}} = -3.46$, $C_b^{\mathrm{FH}} = -3.81$, and $C_c^{\mathrm{FH}} = -2.31$.

8 Conclusion

Group III nitrides have emerged as important materials system in the field of high-frequency, high-power, and high-temperature optoelectronic and microelectronic applications. Especially, applications of these materials realizing bright, white light-emitting diodes appear very promising. In the present study, Raman spectroscopy was applied as a versatile and sensitive technique in characterizing phonon dynamics and other elementary excitations in wz-GaN, which complement results obtained by x-ray diffraction or photoluminescence measurements, for instance. In particular, micro-Raman measurements are widely used since they take advantage of being non-destructive, contactless, and providing an excellent lateral resolution. For materials which are transparent in the range of the employed excitation wavelength a high resolution in the depth is achieved by means of the confocal technique.

First, the influence of mechanical strain on Raman modes was discussed. Using confocal micro-Raman spectroscopy changes of the residual stress within GaN films have been studied with high lateral and depth resolution. The Raman investigations revealed that wafer bending is an effective relaxation mechanism of thermally induced stress due to the difference in thermal expansion coefficients of GaN/sapphire heterostructures. The experimentally determined wafer curvature of the investigated specimens was compared with theoretical ones simulated by a mechanical wafer bending model established by Etzkorn and Clarke as well as a FEM model. The limitations of applicability of the Etzkorn/Clarke model were discussed regarding sample dimensions such as GaN film thickness and substrate radius. By FEM simulations the use of the Etzkorn/Clarke approach was justified in order to simulate the $E_{2,\mathrm{high}}$ Raman frequency in dependence on the GaN layer thickness.

Second, coupled LO phonon plasmon modes were examined in order to determine concentration and mobility of free charge carriers from measured frequencies, bandwidths, and intensities. The doping profile of a wz-GaN c plane single crystal was analyzed and directly correlated to the growth process which provides beneficial feedback to the crystal grower. In particular, confocal Raman measurements in backscattering geometry are meaningful since (i) the measurements are non-destructive and (ii) LO phonons of E_1 symmetry and thus coupled LO phonon plasmon modes are not accessible in backscattering configurations from a surface perpendicular to the c plane (e.g. side edge in direction x). Using a standard dielectric approach from the lineshape fitting of the observed L_+ coupled mode the charge carrier density and

mobility was successfully determined. The obtained results are in good agreement with Hall measurements.

For the application of this semiclassical dielectric approach taking the deformation potential and electro-optical scattering mechanisms into account Faust-Henry coefficients are strictly necessary as input parameter. Faust-Henry coefficients are ratios describing the relative influence of lattice displacements and electric field onto the dielectric susceptibility. Whereas in cubic crystals one Faust-Henry coefficient is sufficient, in wurtzite crystals three coefficients appear according to the symmetry of the Raman tensors. Up to now in the literature merely the coefficient C_a^{FH} was determined with different results and signs. Depending on the sign of the Faust-Henry coefficients contributions of the lattice displacements and the electric field associated with them to the Raman scattering efficiency interfere constructively or destructively.

The Faust-Henry coefficients associated with phonon modes of different symmetry can be obtained by measuring the Raman scattering intensities I_{LO} and I_{TO} of the corresponding LO and TO phonons. In order to access the Raman scattering efficiencies, systematic Raman measurements on undoped wz-GaN single crystals were performed using different scattering geometries. The backscattering as well as the right-angle and near-forward scattering configurations were described in detail. For the first time, a complete set of the relative Raman scattering cross sections of all Raman modes for wz-GaN was determined.

In the present study an accurate determination of the Faust-Henry coefficients including the temperature dependence was reported. Based on the obtained Raman scattering intensities, the Faust-Henry coefficients in wz-GaN were deduced. However, for each coefficient two possible solutions can be found. It was shown that the Raman scattering efficiency of TO phonon polaritons enables to assign one solution of the Faust-Henry coefficients unambiguously.

For this purpose, theoretical expressions of the Raman scattering efficiency for arbitrary directions of phonon polaritons in uniaxial crystals were derived. In the limit of large wavevector magnitudes, the equations describe the behavior of the polar phonons.

A novel experimental near-forward scattering setup was developed using an adjustable rectangular window in front of the entrance lens. This setup enables measurements of phonon polaritons of defined E_1 and A_1 symmetry depending on their wavevector. Polariton spectra of wz-GaN were recorded in different scattering geometries and polarizations. The experimental results are in accordance with the theoretical dispersion curves depending on the transferred polariton wavevector for ordinary and extraordinary phonon polaritons.

The experimentally determined Raman scattering intensities of the phonon polaritons were compared with calculated intensities using the derived theoretical expressions. The comparison excludes the solutions of the Faust-Henry coefficients with the posi-

tive sign. The three Faust-Henry coefficients in wz-GaN are therefore C_a^{FH} = -3.46, C_b^{FH} = -3.81, and C_c^{FH} = -2.31.

Using the determined Raman scattering cross sections and the obtained Faust-Henry coefficients, the Raman tensors for wz-GaN relative to the tensor element of the nonpolar $E_{2,\mathrm{high}}$ phonon were calculated taking the dependence of the Raman scattering efficiency on the phonon frequencies into consideration.

Summarizing all these findings, a full description of the phonon polariton Raman scattering efficiency in wz-GaN was provided. In general the derived scattering efficiency expressions are valid for all uniaxial crystals with wurtzite structure.

Bibliography

[1] H. Morkoc, S. Strite, G. B. Gao, M. E. Lin, B. Sverdlov, and M. Burns. Large-band-gap SiC, III-V nitride, and II-VI ZnSe-based semiconductor device technologies. *J. Appl. Phys.*, 76(3):1363–1398, 1994.

[2] S. Nakamura, T. Mukai, and M. Senoh. Candela-class high-brightness InGaN/AlGaN double-heterostructure blue-light-emitting diodes. *Appl. Phys. Lett.*, 64(13):1687–1689, 1994.

[3] S. Nakamura. III-V nitride based light-emitting devices. *Solid State Commun.*, 102 (2-3):237–248, 1997.

[4] I. Akasaki and H. Amano. Crystal growth and conductivity control of group III nitride semiconductors and their application to short wavelength light emitters. *Jpn. J. Appl. Phys.*, 36(9 A):5393–5408, 1997.

[5] J. S. Speck and S. F. Chichibu. Nonpolar and Semipolar Group III Nitride-Based Materials. *MRS Bulletin*, 34(05):304–312, 2009.

[6] W. Li and W. X. Ni. Residual strain in GaN epilayers grown on sapphire and (6H) SiC substrates. *Appl. Phys. Lett.*, 68(19):2705–2707, 1996.

[7] T. Paskova, D. Hommel, P. P. Paskov, V. Darakchieva, B. Monemar, M. Bockowski, T. Suski, I. Grzegory, F. Tuomisto, K. Saarinen, et al. Effect of high-temperature annealing on the residual strain and bending of freestanding GaN films grown by hydride vapor phase epitaxy. *Appl. Phys. Lett.*, 88:141909, 2006.

[8] M. Barchuk, C. Röder, Y. Shashev, G. Lukin, M. Motylenko, J. Kortus, O. Pätzold, and D. Rafaja. Correlation between the residual stress and the density of threading dislocations in GaN layers grown by hydride vapor phase epitaxy. *J. Cryst. Growth*, 386:1–8, 2014.

[9] T. Kozawa, T. Kachi, H. Kano, H. Nagase, N. Koide, and K. Manabe. Thermal stress in GaN epitaxial layers grown on sapphire substrates. *J. Appl. Phys.*, 77(9): 4389–4392, 1995.

[10] B. J. Skromme, H. Zhao, D. Wang, H. S. Kong, M. T. Leonard, G. E. Bulman, and R. J. Molnar. Strain determination in heteroepitaxial GaN. *Appl. Phys. Lett.*, 71:829, 1997.

[11] E. V. Etzkorn and D. R. Clarke. Cracking of GaN films. *J. Appl. Phys.*, 89:1025, 2001.

[12] C. Roder, S. Einfeldt, S. Figge, T. Paskova, D. Hommel, P. P. Paskov, B. Monemar, U. Behn, B. A. Haskell, P. T. Fini, et al. Stress and wafer bending of a-plane GaN layers on r-plane sapphire substrates. *J. Appl. Phys.*, 100:103511, 2006.

[13] F. Lipski, M. Klein, and F. Scholz. Studies about wafer bow of freestanding GaN substrates grown by hydride vapor phase epitaxy. *J. Cryst. Growth*, 352:235, 2012.

[14] P. Vennegues, B. Beaumont, M. Vaille, and P. Gibart. Microstructure of GaN epitaxial films at different stages of the growth process on sapphire (0 0 0 1). *J. Cryst. Growth*, 173(3):249–259, 1997.

[15] V. Potin, P. Ruterana, and G. Nouet. HREM study of stacking faults in GaN layers grown over sapphire substrate. *J. Phys: Condens. Matter*, 12:10301, 2000.

[16] I. H. Lee, I. H. Choi, C. R. Lee, and S. K. Noh. Evolution of stress relaxation and yellow luminescence in GaN/sapphire by Si incorporation. *Appl. Phys. Lett.*, 71: 1359, 1997.

[17] H. Siegle, P. Thurian, L. Eckey, A. Hoffmann, C. Thomsen, B. K. Meyer, H. Amano, I. Akasaki, T. Detchprohm, and K. Hiramatsu. Spatially resolved photoluminescence and Raman scattering experiments on the GaN/substrate interface. *Appl. Phys. Lett.*, 68:1265, 1996.

[18] F. C. Wang, C. L. Cheng, Y. F. Chen, C. F. Huang, and C. C. Yang. Residual thermal strain in thick GaN epifilms revealed by cross-sectional Raman scattering and cathodoluminescence spectra. *Semicond. Sci. Technol.*, 22:896, 2007.

[19] R. Korbutowicz, M. Tłaczała, J. Kovač, G. Irmer, and R. Srnanek. Cross-sectional and surface Raman mapping of thick GaN layers. *Cryst. Res. Technol.*, 43(12): 1339–1344, 2008.

[20] Y. Huang, X. D. Chen, S. Fung, C. D. Beling, C. C. Ling, Z. F. Wei, S. J. Xu, and C. Y. Zhi. The depth-profiled carrier concentration and scattering mechanism in undoped GaN film grown on sapphire. *J. Appl. Phys.*, 96:1120–1126, 2004.

[21] Y. Huang, X. D. Chen, S. Fung, C. D. Beling, and C. C. Ling. Spatial characterization of a 2 in GaN wafer by Raman spectroscopy and capacitance-voltage measurements. *J. Phys. D: Appl. Phys.*, 37:2814–2818, 2004.

[22] B. Ma, D. Jinno, H. Miyake, K. Hiramatsu, and H. Harima. Orientation dependence of polarized Raman spectroscopy for nonpolar, semi-polar, and polar bulk GaN substrates. *Applied Physics Letters*, 100:011909, 2012.

[23] K. Ishioka, K. Kato, N. Ohashi, H. Haneda, M. Kitajima, and H. Petek. The effect of n- and p-type doping on coherent phonons in GaN. *J. Phys.: Condens. Matter*, 25:205404, 2013.

[24] M. Kuball. Raman spectroscopy of GaN, AlGaN and AlN for process and growth monitoring/control. *Surf. Interface Anal.*, 31:987–999, 2001.

[25] H. Harima. Properties of GaN and related compounds studied by means of Raman scattering. *J. Phys: Condens. Matter*, 14:R967, 2002.

[26] M. V. Klein. *Light Scattering in Solids I*, chapter Electronic Raman Scattering, page 147. Springer-Verlag, 1983.

[27] G. Abstreiter, M. Cardona, and A. Pinczuk. *Light Scattering in Solids IV*, chapter Light Scattering by Free Carrier Excitations in Semiconductors, page 5. Springer-Verlag, 1984.

[28] G. Irmer, V. V. Toporov, B. H. Bairamov, and J. Monecke. Determination of the Charge Carrier Concentration and Mobility in n-GaP by Raman Spectroscopy. *Phys. Status Solidi (b)*, 119:595, 1983.

[29] W. L. Faust and C. H. Henry. Mixing of visible and near-resonance infrared light in GaP. *Phys. Rev. Lett.*, 17:1265, 1966.

[30] M. Cardona. *Light Scattering in Solids II*, chapter Resonance Phenomena, page 19. Springer-Verlag, 1982.

[31] T. Kozawa, T. Kachi, H. Kano, Y. Taga, M. Hashimoto, N. Koide, and K. Manabe. Raman scattering from LO phonon-plasmon coupled modes in gallium nitride. *J. Appl. Phys.*, 75:1098–1101, 1994.

[32] C. Wetzel, W. Walukiewicz, and J. W. Ager III. Electron-phonon scattering in Si doped GaN. *Mater. Res. Soc. Symp. Proc.*, 449:567–572, 1997.

[33] F. Demangeot, J. Frandon, M. A. Renucci, N. Grandjean, B. Beaumont, J. Massies, and P. Gibart. Coupled longitudinal optic phonon-plasmon modes in p-type GaN. *Solid State Communications*, 106:491–494, 1998.

[34] H. Harima, H. Sakashita, and S. Nakashima. Raman microprobe measurement of under-damped LO-phonon-plasmon coupled mode in n-type GaN. *Materials Science Forum*, 264-268:1363–1366, 1998.

[35] H. Harima, H. Sakashita, T. Inoue, and S. Nakashima. Electronic properties in doped GaN studied by Raman scattering. *Journal of Crystal Growth*, 189/190: 672–676, 1998.

[36] I. Loa, S. Gronemeyer, C. Thomson, O. Ambacher, D. Schikora, and D. J. As. Comparative Determination of Absolute Raman Scattering Efficiencies and Application to GaN. *J. Raman Spectrosc.*, 29:291, 1998.

[37] R. H. Poolman, E. A. Muljarov, and A. L. Ivanov. Terahertz response of acoustically driven optical phonons. *Phys. Rev. B*, 81:245208/1–245208/6, 2010.

[38] T. Feurer, J. C. Vaughan, and K. A. Nelson. . *Science*, 299:374, 2003.

[39] K. Saito, T. Tanabe, Y. Oyama, K. Suto, and J. Nishizawa. . *J. Appl. Phys.*, 105: 063102, 2009.

[40] K. Torii, M. Ono, T. Sota, T. Azuhata, S. F. Chichibu, and S. Nakamura. Raman scattering from phonon-polaritons in α-GaN. *Phys. Rev. B*, 62:10861–10866, 2000.

[41] V. Darakchieva, B. Monemar, A. Usui, M. Saenger, and M. Schubert. Lattice parameters of bulk GaN fabricated by halide vapor phase epitaxy. *J. Cryst. Growth*, 310:959–965, 2008.

[42] C. Roder, S. Einfeldt, S. Figge, and D. Hommel. Temperature dependence of the thermal expansion of GaN. *Phys. Rev. B*, 72(8):085218, 2005.

[43] A. F. Wright. Elastic properties of zinc-blende and wurtzite AlN, GaN, and InN. *J. Appl. Phys.*, 82:2833, 1997.

[44] E. Ejder. Refractive Index of GaN. *Phys. Stat. Solidi (a)*, 6:445–448, 1971.

[45] M. Leszczynski, T. Suski, H. Teisseyre, P. Perlin, I. Grzegory, J. Jun, S. Porowski, and T. D. Moustakas. Thermal expansion of gallium nitride. *J. Appl. Phys.*, 76(8): 4909–4911, 1994.

[46] J. H. Edgar and INSPEC (Information service). *Properties of group III nitrides*. EMIS datareviews series, vol. 11. INSPEC, Institution of Electrical Engineers, 1994.

[47] K. Barghout and J. Chaudhuri. Calculation of residual thermal stress in GaN epitaxial layers grown on technologically important substrates. *J. Mater. Sci.*, 39 (18):5817–5823, 2004.

[48] F. Lipski, T. Wunderer, S. Schwaiger, and F. Scholz. Fabrication of freestanding 2″-GaN wafers by hydride vapour phase epitaxy and self-separation during cooldown. *Phys. Status Solidi (a)*, 207(6):1287–1291, 2010.

[49] G. Lukin, C. Röder, E. Niederschlag, Y. Shashev, U. Mühle, O. Pätzold, J. Kortus, D. Rafaja, and M. Stelter. Nucleation of GaN on sapphire substrates at intermediate temperatures by Hydride Vapor Phase Epitaxy. *Cryst. Res. Technol.*, 47(2): 121–130, 2012.

[50] G. Lukin, C. Röder, M. Barchuk, G. Schreiber, O. Pätzold, J. Kortus, D. Rafaja, and M. Stelter. Investigation of GaN layers grown by high temperature vapor phase epitaxy. *Physica Status Solidi C*, 11(3-4):491–494, 2014.

[51] N. Itoh, J. C. Rhee, T. Kawabata, and S. Koike. Study of cracking mechanism in GaN/α-Al_2O_3 structure. *J. Appl. Phys.*, 58(5):1828–1837, 1985.

[52] K. Hiramatsu, T. Detchprohm, and I. Akasaki. Relaxation mechanism of thermal stresses in the heterostructure of GaN grown on sapphire by vapor phase epitaxy. *Jpn. J. Appl. Phys.*, 32(4):1528–1533, 1993.

[53] S. J. Pearton, J. C. Zolper, R. J. Shul, and F. Ren. GaN: Processing, defects, and devices. *J. Appl. Phys.*, 86:1, 1999.

[54] V. Darakchieva, B. Monemar, and A. Usui. On the lattice parameters of GaN. *Appl. Phys. Lett.*, 91:031911, 2007.

[55] K. Fujito, Sh. Kubo, H. Nagaoka, T. Mochizuki, H. Namita, and S. Nagao. Bulk GaN crystals grown by HVPE. *J. Cryst. Growth*, 311:3011–3014, 2009.

[56] H. Ashraf, R. Kudrawiec, J. L. Weyher, J. Serafinczuk, J. Misiewicz, and P. R. Hageman. Properties and preparation of high quality, free-standing GaN substrates and study of spontaneous separation mechanism. *J. Cryts. Growth*, 312: 2398–2403, 2010.

[57] J. F. Nye. *Physical Properties of Crystals*. Clarendon Press, 1957.

[58] M. Suzuki and T. Uenoyama. Strain effect on electronic and optical properties of GaN/AlGaN quantum-well lasers. *J. Appl. Phys.*, 80(12):6868–6874, 1996.

[59] E. Wimmer, H. Krakauer, M. Weinert, and A. J. Freeman. Full-potential self-consistent linearized-augmented-plane-wave method for calculating the electronic structure of molecules and surfaces: O_2 molecule. *Phys. Rev. B*, 24:864–875, 1981.

[60] O. Gunnarson and B. I. Lundquvist. Exchange and correlation in atoms, molecules, and solids by the spin-density-functional formalism. *Phys. Rev. B*, 13: 4274–4298, 1976.

[61] J. M. Wagner and F. Bechstedt. Electronic and phonon deformation potentials of GaN and AlN: ab initio calculations versus experiment. *Phys. Status Solidi (b)*, 234(3):965–969, 2002.

[62] C. Kisielowski, J. Krüger, S. Ruvimov, T. Suski, J. W. Ager III, E. Jones, Z. Liliental-Weber, M. Rubin, E. R. Weber, M. D. Bremser, et al. Strain-related phenomena in GaN thin films. *Phys. Rev. B*, 54(24):17745, 1996.

[63] W. Shan, R. J. Hauenstein, A. J. Fischer, J. J. Song, W. G. Perry, M. D. Bremser, R. F. Davis, and B. Goldenberg. Strain effects on excitonic transitions in GaN: Deformation potentials. *Phys. Rev. B*, 54(19):13460, 1996.

[64] C. A. Arguello, D. L. Rousseau, and S. P. S. Porto. First-Order Raman Effect in Wurtzite-Type Crystals. *Phys. Rev.*, 181:1351–1363, 1969.

[65] V. Yu. Davydov, Yu. E. Kitaev, I. N. Goncharuk, A. N. Smirnov, J. Graul, O. Semchinova, D. Uffmann, M. B. Smirnov, A. P. Mirgorodsky, and R. A. Evarestov. Phonon dispersion and Raman scattering in hexagonal GaN and AlN. *Phys. Rev. B*, 58:12899–12907, 1998.

[66] K. Huang. Lattice Vibrations and Optical Waves in Ionic Crystals. *Nature*, 167: 779, 1951.

[67] K. Huang. On the Interaction between the Radiation Field and Ionic Crystals. *Proc. Roy. Soc.*, A208:352, 1951.

[68] G. Irmer, C. Röder, C. Himcinschi, and J. Kortus. Phonon polaritons in uniaxial crystals: A Raman-scattering study of polaritons in α-GaN. *Phys. Rev. B*, 88(10): 104303, 2013.

[69] R. Claus, L. Merten, and J. Brandmüller. *Light Scattering by Phonon-Polaritons*. Springer Tracts in Modern Physics 75. Springer-Verlag, 1975.

[70] T. Azuhata, T. Sota, K. Suzuki, and S. Nakamura. Polarized Raman spectra in GaN. *J. Phys.: Condens. Matter*, 7:L129–L133, 1995.

[71] G. Yu, H. Ishikawa, T. Egawa, T. Soga, J. Watanabe, T. Jimbo, and M. Umeno. Polarized Reflectance Spectroscopy and Spectroscopic Ellipsometry Determination of the Optical Anisotropy of Gallium nitride on Sapphire. *Jpn. J. Appl. Phys.*, 36: L1029–L1031, 1997.

[72] I. N. Bronshtein, K. A. Semendyayev, G. Musiol, and H. Mühlig. *Handbook of Mathematics*. Springer-Verlag, 2007.

[73] H. Poulet. *Ann. Phys. Paris*, 10:908, 1955.

[74] R. Loudon. The Raman effect in crystals. *Adv. in Physics*, 13:423, 1964.

[75] A. Smekal. Zur Quantentheorie der Dispersion. *Naturwissenschaften*, 11(43): 873, 1923.

[76] C. V. Raman and K. S. Krishnan. A New Type of Secondary Radiation. *Nature*, 121(3048):501, 1928.

[77] G. Landsberg and L. Mandelstam. Eine neue Erscheinung bei der Lichtzerstreuung in Krystallen. *Naturwissenschaften*, 16(28):557, 1928.

[78] D. A. Long. *Raman spectroscopy*. McGraw-Hill, 1977.

[79] H. Kuzmany. *Solid-State Spectroscopy: An Introdiuction*. Springer-Verlag, 2009.

[80] Terence K. S. Wong. *Semiconductor Strain Metrology: Principles and Application*. Bentham eBooks, 2012.

[81] D. L. Mills and E. Burstein. Polaritons: the electromagnetic modes of media. *Rep. Prog. Phys.*, 37:817–926, 1974.

[82] Jr. W. D. Johnston. Nonlinear Optical Coefficients and the Raman Scattering Efficiency of LO and TO Phonons in Acentric Insulating Crystals. *Phys. Rev. B*, 1: 3494–3503, 1970.

[83] T. C. Damen, S. P. S. Porto, and B. Tell. Raman Effect in Zinc Oxide. *Phys. Rev.*, 142(2):570–574, 1966.

[84] R. J. Briggs and A. K. Ramdas. Piezospetroscopic study of the Raman spectrum of cadmium sulfide. *Phys. Rev. B*, 13:5518–5529, 1976.

[85] F. Demangeot, J. Frandon, M. A. Renucci, O. Briot, B. Gil, and R. L. Aulombard. Raman determination of phonon deformation potentials in α-GaN. *Solid State Commun.*, 100:207–210, 1996.

[86] V. Y. Davydov, N. S. Averkiev, I. N. Goncharuk, D. K. Nelson, I. P. Nikitina, A. S. Polkovnikov, A. N. Smirnov, M. A. Jacobson, and O. K. Semchinova. Raman and photoluminescence studies of biaxial strain in GaN epitaxial layers grown on 6H–SiC. *J. Appl. Phys.*, 82:5097, 1997.

[87] F. Demangeot, J. Frandon, P. Baules, F. Natali, F. Semond, and J. Massies. Phonon deformation potentials in hexagonal GaN. *Phys. Rev. B*, 69:155215, 2004.

[88] G. Callsen, J. S. Reparaz, M. R. Wagner, R. Kriste, C. Nenstiel, A. Hoffmann, and M. R. Phillips. Phonon deformation potentials in wurtzite GaN and ZnO determined by uniaxial pressure dependent Raman measurements. *Appl. Phys. Lett.*, 98:061906, 2011.

[89] J. M. Wagner and F. Bechstedt. Phonon deformation potentials of α-GaN and-AlN: An ab initio calculation. *Appl. Phys. Lett.*, 77:346, 2000.

[90] J. M. Wagner and F. Bechstedt. Properties of strained wurtzite GaN and AlN: Ab initio studies. *Phys. Rev. B*, 66(11):115202, 2002.

[91] J. Hertkorn, F. Lipski, P. Brückner, T. Wunderer, S. B. Thapa, F. Scholz, A. Chuvilin, U. Kaiser, M. Beer, and J. Zweck. Process optimization for the effective reduction of threading dislocations in MOVPE grown GaN using in situ deposited SiNx masks. *J. Cryst. Growth*, 310(23):4867–4870, 2008.

[92] P. Brückner, F. Habel, and F. Scholz. HVPE growth of high quality GaN layers. *Phys. Status Solidi (c)*, 3(6):1471–1474, 2006.

[93] *ABAQUS v6.11 Theory Manual*. Dassault Systèmes Simulia Corp., Providence RI USA, 2011.

[94] V. V. Strelchuk, V. P. Bryksa, K. A. Avramenko, M. Y. Valakh, A. E. Belyaev, Y. I. Mazur, M. E. Ware, E. A. DeCuir Jr, and G. J. Salamo. Confocal Raman depth-profile analysis of the electrical and structural properties in III-nitride structures. *Phys. Status Solidi (c)*, 8:2188, 2011.

[95] C. Röder, F. Lipski, F. Habel, G. Leibiger, M. Abendroth, C. Himcinschi, and J. Kortus. Raman spectroscopic characterization of epitaxially grown GaN on sapphire. *J. Phys. D: Appl. Phys.*, 46(28):285302, 2013.

[96] G. G. Stoney. The tension of metallic films deposited by electrolysis. *Proc. R. Soc. Lond. A*, 82(553):172–175, 1909.

[97] G. H. Olsen and M. Ettenberg. Calculated stresses in multilayered heteroepitaxial structures. *J. Appl. Phys.*, 48(6):2543–2547, 1977.

[98] T. Dieing and B. F. Usher. Wafer curvature in molecular beam epitaxy grown heterostructures. *Phys. Rev. B*, 67(5):054108, 2003.

[99] J. B. Wachtman Jr, W. E. Tefft, D. G. Lam Jr, and R. P. Stinchfield. Elastic Constants of Synthetic Single Crystal Corundum at Room Temperature. *J. Res. Natl. Bur. Stand.*, 64A:213, 1960.

[100] L. B. Freund. Substrate curvature due to thin film mismatch strain in the nonlinear deformation range. *J. Mech. Phys. Solids*, 48(6-7):1159–1174, 2000.

[101] G. Irmer, T. Brumme, M. Herms, T. Wernicke, M. Kneissl, and M. Weyers. Anisotropic strain on phonons in a-plane GaN layers studied by Raman scattering. *J. Mater. Sci.: Mater. Electron.*, 19(1):S51–S57, 2008.

[102] I. M. Tiginyanu, A. Sarua, G. Irmer, J. Monecke, S. M. Hubbard, D. Pavlidis, and V. Valiaev. Fröhlich modes in GaN columnar nanostructures. *Phys. Rev. B*, 64:233317, 2001.

[103] A. S. Jr. Barker and M. Ilegems. Infrared Lattice Vibrations and Free-Electron Dispersion in GaN. *Phys. Rev. B*, 7:743, 1973.

[104] B. B. Varga. Coupling of Plasmons to Polar Phonons in Degenerate Semiconductors. *Phys. Rev.*, 137:A1896–A1902, 1965.

[105] A. Mooradian and G. B. Wright. Observation of the interaction of plasmons with longitudinal optical phonons in GaAs. *Phys. Rev. Lett.*, 16:999–1001, 1966.

[106] D. T. Hon and W. L. Faust. Dielectric Parameterization of Raman Lineshapes for GaP with Plasma of Charge Carriers. *Appl. Phys.*, 1:241–256, 1973.

[107] G. Pezzotti, H. Sueoka, A. A. Porporati, M. Manghnani, and W. Zhu. Raman tensor elements for wurtzitic gan and their application to assess crystallographic orientation at film/substrate interfaces. *J. Appl. Phys.*, 110:013527/1–10, 2011.

[108] P. Perlin, J. Camassel, W. Knap, T. Taliercio, J. C. Chervin, T. Suski, I. Grzegory, and S. Porowski. Investigation of longitudinal-optical phonon-plasmon coupled modes in highly conducting bulk GaN. *Appl. Phys. Lett.*, 67:2524–2526, 1995.

[109] G. Popovici, G. Y. Xu, A. Botchkarev, W. Kim, H. Tang, A. Salvador, H. Morkoc, R. Strange, and J. O. White. Raman scattering and photoluminescence of Mg-doped GaN films grown by molecular beam epitaxy. *J. Appl. Phys.*, 82:4020–4023, 1997.

[110] D. I. Florescu, V. M. Asnin, F. H. Pollak, R. J. Molnar, and C. E. C. Wood. High spatial resolution thermal conductivity and Raman spectroscopy investigation of hydride vapor phase epitaxy grown n-GaN/sapphire (0001): doping dependence. *J. Appl. Phys.*, 88:3295–3300, 2000.

[111] V. N. Bessolov, E. V. Konenkova, Y. V. Zhilyaev, and B. A. Paez Sierra. Raman scattering from LO-phonon-plasmon coupled modes in Ag-coated GaN nanocrystals. *Appl. Surface Science*, 235:274–278, 2004.

[112] R. Kirste, S. Mohn, M. R. Wagner, J. S. Reparaz, and A. Hoffmann. Phonon plasmon interaction in ternary group-III-nitrides. *Appl. Phys. Lett.*, 101: 041909/1–4, 2012.

[113] C. Wetzel, W. Walukiewicz, E. E. Haller, J. Ager III, I. Grzegory, S. Porowski, and T. Suski. Carrier localization of as-grown n-type gallium nitride under large hydrostatic pressure. *Phys. Rev. B*, 53:1322–1326, 1996.

[114] K. Jeganathan, R. K. Debnath, R. Meijers, T. Stoica, R. Calarco, D. Gruetzmacher, and H. Lueth. Raman scattering of phonon-plasmon coupled modes in self-assembled GaN nanowires. *J. Appl. Phys.*, 105:123707/1–5, 2009.

[115] D. Kirillov, H. Lee, and J. S. Harris Jr. Raman scattering of GaN films. *J.Appl. Phys.*, 80:4058–4062, 1996.

[116] F. Demangeot, J. Frandon, M. A. Renucci, C. Meny, O. Briot, and R. L. Aulombard. Interplay of electrons and phonons in heavily doped GaN epilayers. *J. Appl. Phys.*, 82:1305–1309, 1997.

[117] M. Klose, R. Dassow, M. Gross, and H. Schroeder. Raman investigations of GaN films grown by pulsed laser deposition. *Journal of Crystal Growth*, 189/190: 666–671, 1998.

[118] M. Park, J. J. Cuomo, B. J. Rodriguez, W.-C. Yang, R. J. Nemanich, and O. Ambacher. Micro-Raman study of electronic properties of inversion domains in GaN-based lateral polarity heterostructures. *J. Appl. Phys.*, 93:9542–9547, 2003.

[119] H. Harima, T. Inoue, S. Nakashima, Furukawa; K., and M. Taneya. Electronic properties in p-type GaN studied by Raman scattering. *Appl. Phys. Lett.*, 73: 2000–2002, 1998.

[120] B. J. Skromme, K. C. Palle, C. D. Poweleit, H. Yamane, M. Aoki, and F. J. DiSalvo. Optical spectroscopy of bulk GaN crystals grown from a Na-Ga melt. *Appl. Phys. Lett.*, 81:3765–3767, 2002.

[121] V. V. Emtsev, V. Yu. Davydov, V. V. Kozlovskii, V. V. Lundin, D. S. Poloskin, A. N. Smirnov, N. M. Shmidt, A. S. Usikov, Aderhold J., H. Klausing, D. Mistele, T. Rotter, J. Stemmer, O. Semchinova, and J. Graul. Point defects in gamma-irradiated n-GaN. *Semicond. Sci. Technol.*, 15:73–78, 2000.

[122] C. H. Henry and J. J. Hopfield. Raman scattering by polaritons. *Phys. Rev. Lett.*, 15:964–966, 1965.

[123] S. P. S. Porto, B. Tell, and T. C. Damen. Near-forward Raman scattering in zinc oxide. *Phys. Rev. Lett.*, 16:450–452, 1966.

[124] C. K. N. Patel and R. E. Slusher. Raman scattering by polaritons in presence of electron plasma in GaAs. *Phys. Rev. Lett.*, 22:282, 1969.

[125] S. Ushioda and J. D. McMullen. Measurement of the frequency dependence of the phonon damping function by Raman scattering from polaritons in GaP. *Solid State Commun.*, 11:299, 1972.

[126] J. H. Nicola and R. C. C. Leite. Resonant Raman scattering from polaritons in ZnSe. *Phys. Rev. B*, 11:798, 1975.

[127] J. H. Nicola, J. A. Freitas, and R. C. C. Leite. Raman scattering by the upper branch polariton in ZnO. *Solid State Commun.*, 17:1379, 1975.

[128] H. E. Puthoff, R. H. Pantell, B. G. Huth, and M. A. Chacon. Near-Forward Raman Scattering in $LiNbO_3$. *J. Appl. Phys.*, 39:2144, 1968.

[129] A. Pinczuk, E. Burstein, and S. Ushioda. Raman scattering by polaritons in tetragonal $BaTiO_3$. *Solid State Commun.*, 7:139, 1969.

[130] J. F. Scott, P. A. Fleury, and J. M. Worlock. Light Scattering from Polaritons in Centrosymmetric Crystals. *Phys. Rev.*, 177:1288, 1969.

[131] R. Claus, G. Borstel, and L. Merten. Light scattering by polaritons associated with ordinary photons in $LiNbO_3$. *Opt. Commun.*, 3:17, 1971.

[132] E. Burstein, S. Ushioda, and A. Pinczuk. Polariton Results in Ferroelectrics with the Tungsten Bronze Crystal Structure. *Appl. Phys. Lett.*, 20:230, 1972.

[133] A. D'Andrea, B. Fornari, G. Mattei, M. Pagannone, and M. Scrocco. Light Scattering from Polaritons in $NaBrO_3$ and $NaClO_3$. *Phys. Status Solidi (b)*, 54: K131, 1972.

[134] W. S. Otaguro, E. Wiener-Avnear, S. P. S. Porto, and J. Smit. Oblique Polaritons in Uniaxial Crystals: Application to $LiIO_3$. *Phys. Rev. B*, 6:3100, 1972.

[135] F. X. Winter and R. Claus. On the observation of ordinary polaritons in $LiNbO_3$. *Opt. Commun.*, 6:22, 1972.

[136] F. X. Winter. Light scattering by polaritons associated with ordinary photons in $LiIO_3$. *Phys. Lett.*, 40A:425, 1972.

[137] M. Posledovich, F. X. Winter, G. Borstel, and R. Claus. Properties of Extraordinary Polaritons in $LiNbO_3$. *Phys. Status Solidi (b)*, 55:711, 1973.

[138] F. X. Winter, E. Wiesendanger, and R. Claus. Polaritons and Phonon Assignment in Orthorhombic $KNbO_3$ investigated by Light Scattering. *Phys. Status Solidi (b)*, 64:95, 1974.

[139] F. X. Winter, E. Wiesendanger, and R. Claus. Polariton- and Directional Dispersion of Polar Modes in Orthorhombic $KNbO_3$ investigated by Light Scattering. *Phys. Status Solidi (b)*, 72:189, 1975.

[140] L. A. Kulevsky, Yu. N. Polivanov, and S. N. Poluektov. Stokes and Anti-Stokes Scattering of Light by Low-Frequency polaritons in $LiIO_3$. *J. Raman Spectrosc.*, 5: 269, 1976.

[141] A. S. Barker and R. Loudon. Response Functions in the Theory of Raman Scattering by Vibrational and Polariton Modes in Dielectric Crystals. *Rev. Mod. Phys.*, 44:18–47, 1972.

[142] L. Merten. *Atomic Structure and Properties of Solids*. Academic Press, 1972.

[143] L. Merten. *Advances in Solid State Physics XII*. Pergamon Press, 1972.

[144] V. M. Agranovich and D. L. Mills, editors. *Surface Polaritons*. North-Holland Publishing Company, 1982.

[145] S. S. Ng, T. L. Yoon, Z. Hassan, and H. Abu Hassan. Surface and interface phonon polaritons of wurtzite GaN thin film grown on 6H-SiC substrate. *Appl. Phys. Lett.*, 94:24191/1–241912/3, 2009.

[146] S. F. Cheah, S. C. Lee, S. S. Ng, F. K. Yam, and H. A. Hassan. Surface phonon polariton characteristic of honeycomb nanoporous GaN thin films. *Appl. Phys. Lett.*, 102:101601/1–101601/5, 2013.

[147] M. Born and E. Wolf. *Principles of optics*. Cambridge University Press, 1999.

[148] S. A. Akhmanov and S. Yu. Nikitin. *Physical optics*. Clarendon Press, 1997.

[149] H. Siegle, G. Kaczmarczyk, L. Filippidis, A. P. Litvinchuk, A. Hoffmann, and C. Thomsen. Zone-boundary phonons in hexagonal and cubic GaN. *Phys. Rev. B*, 55:7000–7004, 1997.

List of Figures

List of Tables

List of Publications

[1] C. Himcinschi, I. Vrejoiu, T. Weißbach, K. Vijayanandhini, A. Talkenberger, C. Röder, S. Bahmann, D.R.T. Zahn, A.A. Belik, D. Rafaja, et al. Raman spectra and dielectric function of $BiCrO_3$: Experimental and first-principles studies. *Journal of Applied Physics*, 110(7):073501–073501, 2011.

[2] G. Lukin, C. Röder, E. Niederschlag, Y. Shashev, U. Mühle, O. Pätzold, J. Kortus, D. Rafaja, and M. Stelter. Nucleation of GaN on sapphire substrates at intermediate temperatures by Hydride Vapor Phase Epitaxy. *Crystal Research and Technology*, 47(2):121–130, 2012.

[3] A. Talkenberger, C. Himcinschi, T. Weißbach, K. Vijayanandhini, I. Vrejoiu, C. Röder, D. Rafaja, and J. Kortus. Raman spectroscopic and X-ray diffraction investigations of epitaxial $BiCrO_3$ thin films. *Thin Solid Films*, 520(14):4590–4594, 2012.

[4] S. Förster, T. Hahn, C. Loose, C. Röder, S. Liebing, W. Seichter, F. Eißmann, J. Kortus, and E. Weber. Synthesis and characterization of new derivatives of azulene, including experimental and theoretical studies of electronic and spectroscopic behavior. *Journal of Physical Organic Chemistry*, 25(10):856–863, 2012.

[5] F. B. Bairamov, V. V. Toporov, E. D. Poloskin, H. Bairamov, C. Röder, C. Sprung, K. Bohmhammel, J. Seidel, G. Irmer, A. Lashkul, E. Lähderanta, and Y. W. Song. Resonant inelastic light scattering and photoluminescence in isolated nc-Si/SiO_2 quantum dots. *Semiconductors*, 47(5):623–627, 2013.

[6] T. Gruber, D. Thomas, C. Röder, F. Mertens, and J. Kortus. Raman spectroscopic studies of Li_xSi_y compounds. *Journal of Raman Spectroscopy*, 44(6):934–938, 2013.

[7] C. Röder, F. Lipski, F. Habel, G. Leibiger, M. Abendroth, C. Himcinschi, and J. Kortus. Raman spectroscopic characterization of epitaxially grown GaN on sapphire. *Journal of Physics D: Applied Physics*, 46(28):285302, 2013.

[8] J. Hanzig, M. Zschornak, F. Hanzig, E. Mehner, H. Stöcker, B. Abendroth, C. Röder, A. Talkenberger, G. Schreiber, D. Rafaja, S. Gemming, and D.C.

Meyer. Migration-induced field-stabilized polar phase in strontium titanite single crystals at room temperature. *Physical Review B*, 88(2):024104, 2013.

[9] G. Irmer, C. Röder, C. Himcinschi, and J. Kortus. Phonon polaritons in uniaxial crystals: A Raman-scattering study of polaritons in α-GaN. *Physical Review B*, 88(10):104303, 2013.

[10] C. Röder, T. Weißbach, C. Himcinschi, J. Kortus, S. Dudczig, and C.G. Aneziris. Raman spectroscopic characterization of novel carbon-bonded filter compositions for steel melt filtration. *Journal of Raman Spectroscopy*, 45(1):128–132, 2014.

[11] M. Barchuk, C. Röder, Y. Shashev, G. Lukin, M. Motylenko, J. Kortus, O. Pätzold, and D. Rafaja. Correlation between the residual stress and the density of threading dislocations in GaN layers grown by hydride vapor phase epitaxy. *Journal of Crystal Growth*, 386:1–8, 2014.

[12] G. Lukin, C. Röder, M. Barchuk, G. Schreiber, O. Pätzold, J. Kortus, D. Rafaja, and M. Stelter. Investigation of GaN layers grown by high temperature vapor phase epitaxy. *Physica Status Solidi C*, 11(3-4):491–494, 2014.

[13] A. Dorner-Reisel, R. Lieberwirth, S. Svoboda, K. Günther, C. Röder, C. Himcinschi, G. Irmer, and S. Weißmantel. Wear behaviour of hydrogen free diamond-like carbon thin films in diesel fuel at different temperatures. *Diamond and Related Materials*, 44(0):78–87, 2014.

[14] M. Daschner de Tercero, C. Röder, U. Fehrenbacher, U. Teipel, and M. Türk. Continuous supercritical hydrothermal synthesis of iron oxide nanoparticle dispersions and their characterization. *Journal of Nanoparticle Research*, 16(4): 1–27, 2014.

Parts of this thesis are already published in [7] and [9].

Acknowledgements

At the end of my thesis, I want to thank a couple of people.

- First of all, I want to thank my supervisor Prof. Dr. Jens Kortus for providing the interesting topic and for all his patience he had with me.
- Furthermore, I want to thank Prof. Dr. Ion M. Tiginyanu for being the coreferee of this thesis.
- Special thanks go to Prof. i.R. Dr. Gert Irmer for fruitful, enlightening, and inspiring discussions as well as the introduction in fundamental phenomena of Raman scattering. I think a good part of this thesis was only possible due to your work.
- This work was performed within the Cluster of Excellence *Structure Design of Novel High-Performance Materials via Atomic Design and Defect Engineering (ADDE)* which is financially supported by the European Union (European regional development fund) and by the Ministry of Science and Art of Saxony (SMWK).
  I am very grateful for this funding.
- I want to highlight the *brilliant* atmosphere within the group of Prof. Dr. Jens Kortus. I really enjoyed to be part of this group. In particular, I thank Silvia, Claudia, and Andreas for the *sustainable* improvement in the quality of working life. The pleasant coffee break in the afternoon was source of many *novel* ideas.
- Moreover, manys thanks go to Dr. Cameliu Himcinschi as head of the Raman laboratory for giving me plenty of rope and Birgit Ostermay for her skillful technical assistance and her retentive memory.
- What is the use of a powerful characterization method without samples? I gratefully acknowledge the fruitful coorperation with Gleb Lukin and Dr. Olf Pätzold (Institute of Nonferrous Metallurgy and Purest Materials), Dr. Frank Habel and Dr. Gunnar Leibiger (Freiberger Compound Materials GmbH) as well as Dr. Franziska Beyer (Institute of Applied Physics), especially in providing high-quality GaN specimens and supporting the sample preparation.
- Last but not least I have to thank my family and friends for supporting me for all the years.

Versicherung

Hiermit versichere ich, dass ich die vorliegende Arbeit ohne unzulässige Hilfe Dritter und ohne Benutzung anderer als der angegebenen Hilfsmittel angefertigt habe; die aus fremden Quellen direkt oder indirekt übernommenen Gedanken sind als solche kenntlich gemacht.

Die Hilfe eines Promotionsberaters habe ich nicht in Anspruch genommen. Weitere Personen haben von mir keine geldwerten Leistungen für Arbeiten erhalten, die nicht als solche kenntlich gemacht worden sind. Die Arbeit wurde bisher weder im Inland noch im Ausland in gleicher oder ähnlicher Form einer anderen Prüfungsbehörde vorgelegt.

30. September 2014 Dipl. Nat. Christian Röder

Declaration

I hereby declare that I completed this work without any improper help from a third party and without using any aids other than those cited. All ideas derived directly or indirectly from other sources are identified as such.

I did not seek the help of a professional doctorate-consultant. Only those persons identified as having done so received any financial payment from me for any work done for me. This thesis has not previously been published in the same or a similar form in Germany or abroad.

30th September 2014 Dipl. Nat. Christian Röder